

UNIVERSITY OF MELBOURNE

MASTER'S THESIS

**Measurements of the ATLAS tau trigger
reconstruction and identification efficiencies using
2016 data from pp collisions at $\sqrt{s} = 13$ TeV**

Author:
Lara MASON

Supervisor:
Prof. Elisabetta BARBERIO

*A thesis submitted in fulfillment of the requirements
for the degree of Master of Philosophy*

in the

ARC Centre of Excellence for Particle Physics at the Terascale
Department of Physics

April 4, 2018

University of Melbourne

Abstract

Faculty of Science
Department of Physics

Master of Philosophy

Measurements of the ATLAS tau trigger reconstruction and identification efficiencies using 2016 data from pp collisions at $\sqrt{s} = 13$ TeV

by Lara MASON

This thesis presents the performance of the tau trigger algorithm used by the ATLAS experiment to select hadronically decaying tau leptons in the LHC Run 2. Using the 33.3 fb^{-1} of pp collision data recorded in 2016 at $\sqrt{s} = 13$ TeV, the performance of this algorithm is studied using a ‘tag-and-probe’ based analysis in order to select Z boson decays to tau leptons, where one tau decays hadronically and the other leptonically. The reconstruction and identification efficiencies of the tau trigger algorithm are measured, and good performance is observed. The efficiency of the tau trigger in data is compared with that in simulation, and is parametrised as a function of the tau decay topology, its kinematics, and the average number of interactions per bunch crossing. The selection efficiency at each step of the high level trigger is measured, using dedicated intermediary triggers, and good agreement between data and simulation is observed. Using the comparison between reconstruction and identification efficiencies in data and simulation, correction factors for simulated events are measured, which are utilised by the entire ATLAS collaboration.

Acknowledgements

Firstly, a huge thanks to Elisabetta, for her support and for being so accommodating and welcoming. As a successful and formidable woman in physics you are a true inspiration to me. A resounding thanks must go to Federico, for his immeasurable help with the work presented here, for always having time to explain when I came running into his office complaining that something wasn't working, for his eternal patience when I didn't understand, for weird comments he left in code he gave to me, for his supreme command of gifs (which he sent to me when I achieved something) and for his quiet confidence in me.

Huge thanks also to Matt Dolan and Quentin, to Ligang, Takashi² and the whole Tau Trigger group, and to my office mates and colleagues (in particular Marco Milesi and Laurence Spiller for their help and repertoire of YouTube videos, and of course Sean Crosby, for always helping me with computer things and not losing his cool even when I took down an entire node with a memory leak I caused). Massive thanks also to Daniele, for teaching me so much, and for giving me the opportunity to co-author an ATLAS Note. Thank you to the whole of CoEPP for help, guidance and inspiration. Thank you to Andy Buffler for being the reason I swapped my life from chemistry to physics (thank heavens for that) and to Andrew Hamilton, far north in the freezing lands of Canada, for introducing me to HEP and for being just the best.

Infinite thanks to my wonderful dad, for his unwavering support, for always sending me any physics jokes he finds in the paper, and for being the only non-physicist to be genuinely interested in what it is that I do. I love you. To the rest of my family, I also love you guys even though you still don't care what a quark is. And to Sean Magner, even if you never read more than the abstract you'll always be my number one.

Contents

Abstract	iii
1 Introduction	1
2 Theory Overview	3
2.1 The Standard Model	3
2.1.1 The Z boson	3
2.1.2 The Tau Lepton	3
2.2 Hadronic Collisions	4
3 LHC and the ATLAS experiment	7
3.1 The Large Hadron Collider	7
3.2 The ATLAS Detector	7
3.2.1 Inner Detector	9
3.2.2 Calorimeters	10
3.2.3 Muon Spectrometer	10
3.3 The ATLAS Trigger System	10
3.4 Reconstruction and identification of hadronic tau lepton decays	11
3.4.1 Online reconstruction	12
Level 1	12
High Level Trigger	12
3.4.2 Offline Reconstruction	13
3.4.3 Identification variables	14
4 $Z \rightarrow \tau\tau$ Tag and Probe Analysis	17
4.1 Data and Simulation	17
4.2 Object and Event Selection	18
4.2.1 Muon	18
4.2.2 Tau	19
4.2.3 Further Object Selection	19
4.2.4 Event Selection	19
4.3 Background Estimation	20
4.3.1 Methodology	20
4.3.2 Multi-jet Background	21
4.3.3 Lepton Backgrounds	23
4.3.4 $W(\rightarrow \mu\nu) + \text{jets}$ Background	25
$W(\rightarrow \mu\nu) + \text{jets}$ Shape	26
Correction Factor	27
4.4 Uncertainties	28
4.5 Validation of the background estimation method	28
4.6 Online Tau Reconstruction Performance	32
4.7 Efficiency Measurement	38
4.8 Scale Factors	41

4.9 HLT Selection Steps Efficiencies	43
5 Conclusion	47
A Appendix	49
A.1 Higher p_T Triggers	49

To anyone who has ever let me talk about physics to them

Chapter 1

Introduction

The Standard Model [1] is the leading theory in particle physics, describing all known elementary particles with impressive accuracy and tracing them back to a set of relatively simple mathematics rules described within the formalism of a relativistic quantum field theory [2]. In particle physics, our best probe of nature and of the Standard Model is a collider, such as the Large Hadron Collider (LHC) [3] at CERN, at which the data contained in this thesis are gathered by the ATLAS Collaboration. The Standard Model successfully incorporates all elementary particles discovered thus far, and following the Higgs discovery in 2012 [4] all predicted particles are accounted for. However, small inconsistencies are leading some physicists to consider extensions to the framework, using the consistently higher energies available at colliders to verify the Standard Model to greater precision, as well as to test theories beyond the Standard Model (BSM). A conceptual limitation of the Standard Model, known as the hierarchy problem [5], finds its name in the instability of mass scales between the electroweak symmetry breaking scale and the grand unification scale, or Planck mass. Another question is the nature of Dark Matter [6], for which there is no viable candidate predicted by the Standard Model as we know it currently. A third question is the unification [5] of the three fundamental interactions described, each with their own symmetry, by the Standard Model. It would be appealing to imbed these interactions into a single symmetry, and even more so to include gravity, which at present is left out of the Standard Model. These questions may be answered as we reach higher energies, probe the limits of the Standard Model, and perhaps discover new particles at the LHC. For this to occur, and for further studies on the Standard Model as we know it to take place, we require a highly efficient detector which can catch even the most elusive of particles in its net. This efficiency, as it relates to tau particles, is the subject of this thesis.

Tau leptons are a key signature in many Standard Model measurements, as well as many beyond the Standard Model searches for new physics [7]. Final states featuring hadronically decaying taus are an important part of the ATLAS physics program and are notoriously difficult to distinguish from major backgrounds, relying critically on the hadronic tau reconstruction and identification algorithm used by the tau trigger, referred to as *online*, as well as a further *offline* reconstruction algorithm. The tau trigger algorithm is divided into two levels; the *Level 1 trigger* (L1) and the *High level trigger* (HLT), where a first separation is achieved between hadronically decaying tau leptons and the large background of QCD jets by using a *Boosted Decision Tree* (BDT) [8], a machine learning technique for developing cut-based discriminants to extract hadronically decaying taus from dominant backgrounds. Using a *tag-and-probe* method in order to select $Z \rightarrow \tau\tau$ events, the efficiency of the tau trigger is studied, as well as the performance of its reconstruction and identification components.

Monte Carlo simulations are used to model the backgrounds in physics searches. It is therefore crucial that Monte Carlo simulation incorporates the correct modelling and normalisation of variables. This is ensured through the use of *scale factors*, correction factors for simulated events which correct the efficiencies measured in Monte Carlo to the results from data. The scale factors presented in this analysis are critical input for all ATLAS analyses concerning hadronically decaying tau leptons using

data gathered in 2016.

This thesis uses data collected by the ATLAS collaboration at the Conseil Européen pour la Recherche Nucléaire (CERN) in Geneva in 2016, corresponding to a total integrated luminosity of $\mathcal{L} = 33.3 \text{ fb}^{-1}$, and is structured as follows. In Chapter 2, a brief description of the Standard Model is given, paying special attention to the elementary particles of interest to this analysis. A description is given in Chapter 3 of the Large Hadron Collider and the ATLAS detector, including the online and offline reconstruction and identification algorithms used at ATLAS in Section 3.4.

The analysis is described in full in Chapter 4. The data and simulation used are further described in Chapter 4.1. The estimation of the background to the signal events is described in Section 4.3, including a new approach developed in this analysis to estimate the $W(\rightarrow \mu\nu) + \text{jets}$ background events, which is modelled using a data-driven estimation. The background due to *multi-jet* events, referring to jets of energetic quarks and gluons, is also modelled using a data-driven estimation, because the strong interaction by which the quarks and gluons interact is not well modelled by simulation. The remaining backgrounds are modelled via Monte Carlo simulation.

In Section 4.7, the efficiencies of several tau triggers, each with differing minimum transverse momentum requirements, are measured, along with their associated scale factors. Efficiencies are parametrised by tau p_T , tau η , and by the average number of interactions per bunch crossing, μ , respectively, and the efficiency at each step of the HLT is investigated using dedicated intermediary triggers. The plots shown in Section 4.6, 4.7 and 4.8 have been accepted by the Tau Trigger Group and the ATLAS Trigger group, and the scale factors given in Section 4.8 are now being utilised by the entire ATLAS Collaboration.

Chapter 2

Theory Overview

2.1 The Standard Model

All particles relevant for the work presented in this thesis are described, in both their properties and interactions, by the Standard Model of particle physics [1]. The unification of the electromagnetic and weak forces by Glashow, Weinberg and Salam [9], [10], [11] in the late 1960s yielded the Standard Model as we know it today, describing three of the four fundamental forces (strong, weak, and electromagnetic, but not gravitational), three generations of fermions, and bosons.

In the Standard Model, the fundamental building blocks of matter are fermions, particles with spin values of $\frac{1}{2}$ which obey Fermi-Dirac statistics. Among them, three generations of quarks and leptons (and their corresponding antiparticles) are present. Tau leptons are included in the third generation, and are heavier than their corresponding first and second generation counterparts, namely the electron and the muon. All matter particles carry the weak charge, and so can interact via the weak force. Each lepton has an associated neutrino (ν_ℓ), a fermion which carries only the weak charge. Because neutrinos are not electromagnetically charged they do not interact with the ATLAS detector, and are observable only through the missing transverse energy observed in ATLAS collision events.

Forces are mediated by the exchange of spin 1 vector bosons which obey Bose-Einstein statistics. They are the photon γ (the propagator of the electromagnetic force), the gluon g (the propagator of the strong force), and the Z and $W^{+/-}$ bosons (propagators of the weak force). There exists only one elementary scalar boson, the Higgs boson, which has been introduced into the Standard Model to provide a mechanism by which particles acquire mass.

The final state particles of importance to this thesis are the Z boson, the tau, τ , the muon, μ , and the neutrino, ν_ℓ .

2.1.1 The Z boson

The Z boson is an elementary vector boson, the propagator of the weak force, and a key particle in this analysis. It is electrically neutral, and has a mass of 91.1876 ± 0.0021 GeV [12]. In proton-proton collisions such as those relevant to this thesis, the Z boson can be produced only by the annihilation of a quark and an antiquark ($q\bar{q}$). Due to its large mass, the Z boson decays promptly after production and is only observable by its decay products, which traverse the detector. The branching fraction of the Z boson produced in the pp collision to decay to a pair of tau leptons, which describes the probability of this decay mode, is 3.370 ± 0.008 % [12].

2.1.2 The Tau Lepton

The tau lepton is an elementary fermion of the third generation. In comparison to its first and second generation counterparts, the tau is very heavy; with a mass of 1776.86 ± 0.12 MeV [12] it is almost 3500

TABLE 2.1: The predominant hadronic tau decay modes and their branching fractions, taken from [12].

Decay Mode	Branching Fraction (%)
1-prong	
$\tau^\pm \rightarrow \pi^\pm \nu_\tau$	10.82
$\tau^\pm \rightarrow \pi^\pm \pi^0 \nu_\tau$	25.49
$\tau^\pm \rightarrow \pi^\pm 2\pi^0 \nu_\tau$	9.26
$\tau^\pm \rightarrow \pi^\pm 3\pi^0 \nu_\tau$	1.04
$\tau^\pm \rightarrow K^\pm \nu_\tau + \text{neutral particles}$	1.54
3-prong	
$\tau^\pm \rightarrow 2\pi^\pm \pi^\mp \nu_\tau$	8.99
$\tau^\pm \rightarrow 2\pi^\pm \pi^\mp \pi^0 \nu_\tau$	2.74
$\tau^\pm \rightarrow K^\pm \pi^\pm \pi^\mp \nu_\tau + \text{neutral particles}$	0.33

times more massive than the electron and 17 times more massive than the muon, and has a proper decay length of $87 \mu\text{m}$ [12]. Tau leptons decay either leptonically ($\tau \rightarrow \ell + \nu_\ell + \nu_\tau$) or hadronically ($\tau \rightarrow \text{hadrons} + \nu_\tau$) [13], and do so before they can traverse the detector. Because of this very short mean life of only $2.903 \times 10^{-13} \text{ s}$ [12], tau leptons can only be detected via their decay products.

The branching fraction for the leptonic decay specific to the production of a muon ($\tau^- \rightarrow \mu^- \bar{\nu}_\mu \nu_\tau$) is given by [12] as 17.4 %, while hadronic decays occur 64.8 % of the time. The leptonic decays involving the production of an electron will not be considered in this analysis. The main hadronic decay channels consist of one or three charged pions π^\pm or occasionally kaons K^\pm , with additional neutral pions π^0 or kaons K^0 and a tau neutrino ν_τ . Of primary interest in hadronic decay modes are 1-prong and 3-prong candidates, referring to the one or three associated charged pions produced during the decay. The predominant hadronic tau decay modes are listed in Table 2.1. The neutral and charged hadrons produced in the hadronic tau decay make up the visible part of the tau lepton, and are referred to as $\tau_{\text{had,vis}}$.

In this analysis, di-tau decays of the Z boson are considered, where one tau decays leptonically and the other tau decays hadronically. An example Feynman diagram for this process is given in Figure 2.1. In the diagram, a Z boson is produced by a $q\bar{q}$ annihilation, and decays into a $\tau^+\tau^-$ pair. The pair of taus produced must have opposite charge by charge conservation. In this instance, the τ^- then decays hadronically via a W^- boson into a pair of quarks, which form hadronic jets. The τ^+ decays leptonically via a W^+ boson to a μ^+ and a $\bar{\nu}_\mu$ pair. The choice of decay modes for the τ^+ and τ^- in this instance are purely diagrammatic; for this process it is equally possible that the τ^- could decay leptonically and the τ^+ could decay hadronically.

2.2 Hadronic Collisions

At the Large Hadron Collider, proton beams are accelerated to produce collisions with a center of mass energy of $\sqrt{s} = 13 \text{ TeV}$. A proton is comprised of three valence quarks (uud) which can self-interact via gluons, and additional *sea quarks*, which spontaneously annihilate and materialise inside the proton. The momentum distributions of these quarks and gluons, collectively termed partons, are described by the universal parton distribution functions (PDFs) on which the structure of the proton depends. At high collision energies, these partons are effectively free to interact independently.

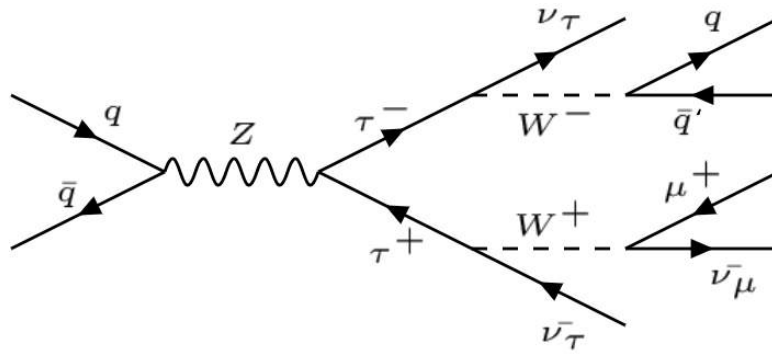


FIGURE 2.1: An example Feynman diagram to leading order showing a Z boson decaying to a pair of tau leptons, one of which decays leptonically and the other hadronically.

Since physics at the subatomic level is governed by quantum mechanics, the occurrence of processes of interest is governed by probability. The probability of each event is proportional to its *cross-section*, denoted σ . The number of expected events N is then given by

$$N = \sigma \cdot \int \mathcal{L} dt, \quad (2.1)$$

where \mathcal{L} is the *instantaneous luminosity* [14], a machine parameter which measures the ability of a particle accelerator to produce the required number of interactions. In order to increase the number of events collected for physics, beams are collided at higher and higher instantaneous luminosities in order to increase the number of hard scatters between partons. This leads to a phenomenon termed *pileup*, where multiple events generated in the same or different bunch-crossing(s) overlap in the detector.

Chapter 3

LHC and the ATLAS experiment

The Large Hadron Collider (LHC) [3] is a proton synchrotron located at CERN in Geneva, Switzerland. Located about 100 m below ground with a circumference of 26.7 km, the LHC produces and collides beams of protons which are detected by the five experiments located around its circumference: ATLAS, CMS, ALICE, TOTEM and LHCb. For this thesis, data collected by the ATLAS experiment were analysed. The aim of the LHC is to reveal physics beyond the Standard Model, by colliding protons with center of mass collision energies of up to 14 TeV. The LHC began its second operational run, termed Run 2, in 2015, when it began accelerating protons to an energy of 6.5 TeV, producing collisions at a center of mass energy of $\sqrt{s} = 13$ TeV.

In the following, the LHC is discussed in Section 3.1. A description is then given of the ATLAS detector and its subdetectors in Section 3.2, and of the ATLAS trigger system in Section 3.3. Finally, a description of the online and offline identification and reconstruction algorithms performed on hadronically decaying tau candidates is given in Section 3.4.

3.1 The Large Hadron Collider

The LHC is a superconducting hadron accelerator and collider. Because it is a particle-particle collider, it is made up of two rings with counter rotating beams, in which the protons are accelerated. Protons are accelerated at the LHC in bunches, while the superconducting magnet system within the tunnel accelerates, steers and focuses the two proton beams travelling in opposite directions around the ring.

During 2016 data-taking the LHC delivered a peak luminosity to ATLAS of $13.8 \times 10^{33} \text{ cm}^{-2}\text{s}^{-1}$ during stable beams [15], which are beams that are good for data-taking, and delivered a total integrated luminosity of 38.5 fb^{-1} . Of the luminosity delivered, ATLAS recorded 35.6 fb^{-1} . Figure 3.1 shows plots related to the luminosity delivered in Run 2, pertaining specifically to 2016 collisions, where the total integrated luminosity accounts for the luminosity delivered from the declaration of stable beams to the standby of sensitive detectors to allow a beam dump or beam studies [15]. A beam dump is the process by which the beam is completely extracted from the ring of the collider and absorbed by dedicated systems. The recorded luminosity refers to the amount of data stored to disk by the ATLAS experiment. As indicated in Section 2.2, higher luminosities lead to more interactions per bunch crossing. The mean number of interactions per bunch crossing, μ , or pile-up, is shown in Figure 3.1, averaged over all colliding bunch pairs. Only the maximum value during stable beam periods is shown.

3.2 The ATLAS Detector

The ATLAS (A Toroidal Lhc ApparatuS) detector [16] is a multi-purpose particle detector with forward-backward symmetric cylindrical geometry and nearly 4π coverage in solid angle, and consists, in order from the collision point moving radially outwards, of an inner detector (ID), electromagnetic

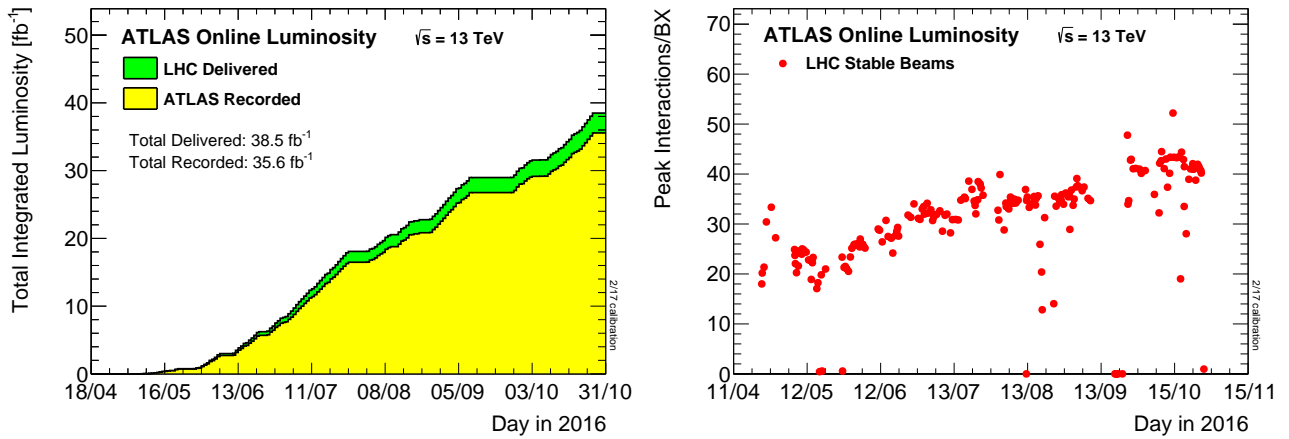


FIGURE 3.1: Luminosity summary plots for 2016 data taking during stable beams for pp collisions at $\sqrt{s} = 13$ TeV showing (left) total integrated luminosity delivered by the LHC in green, and recorded by the ATLAS detector in yellow, and (right) the maximum mean number of inelastic collisions per bunch crossing [15].

(EM) and hadronic (HAD) calorimeters, and a muon spectrometer (MS). It is depicted in Figure 3.2. The specifications and performance of the ATLAS detector can be found at [16], and a summary is provided here.

The nominal proton-proton collision point serves as the origin of the coordinate system used at ATLAS. The beam line defines the \hat{z} -direction, while the x - y plane, known as the transverse plane, lies perpendicular to the beam, with the positive \hat{x} -axis pointing towards the center of the ring, and the positive \hat{y} -axis pointing vertically upwards. The kinematics of the partons in the initial state along the \hat{z} -axis is not known. The azimuthal angle, ϕ , lies in the x - y plane and is measured around the beam axis, while the polar angle θ is measured from the beam axis. The rapidity, y , is defined as

$$y = \frac{1}{2} \ln \left(\frac{E + p_z}{E - p_z} \right), \quad (3.1)$$

and is related to the angle between the x - y plane and the direction of the outgoing particles from the collision. It is defined such that for high energy products of a collision which are directed into the x - y plane with a high transverse momentum and a negligible \hat{z} momentum component, the rapidity will tend to 0. For highly energetic particles which are produced with a large component of momentum in the beam direction, $E \approx p_z$ and the rapidity tends to ∞ .

For highly relativistic particles, we define the pseudorapidity η as

$$\eta = -\ln \left(\tan \frac{\theta}{2} \right), \quad (3.2)$$

which is used in place of the rapidity as it only requires knowledge of θ . For highly relativistic particles, such as those produced at the LHC, $y \approx \eta$, where $\eta = 0$ points perpendicularly to the beam line, and runs to $\eta = \infty$ at the beam line. The detector is symmetric about $\eta = 0$. Although η is not Lorentz-invariant under transformations (or *boosts*) along the \hat{z} axis, $\Delta\eta$ is invariant under these transformations. For this reason, the angle of emission of a particle is often given in $\Delta\eta \times \Delta\phi$ space, which is undistorted by boosts parallel to the beam axis with respect to the rest frame of the detector, and is therefore independent of the highly relativistic kinematics of the particle in the \hat{z} direction.

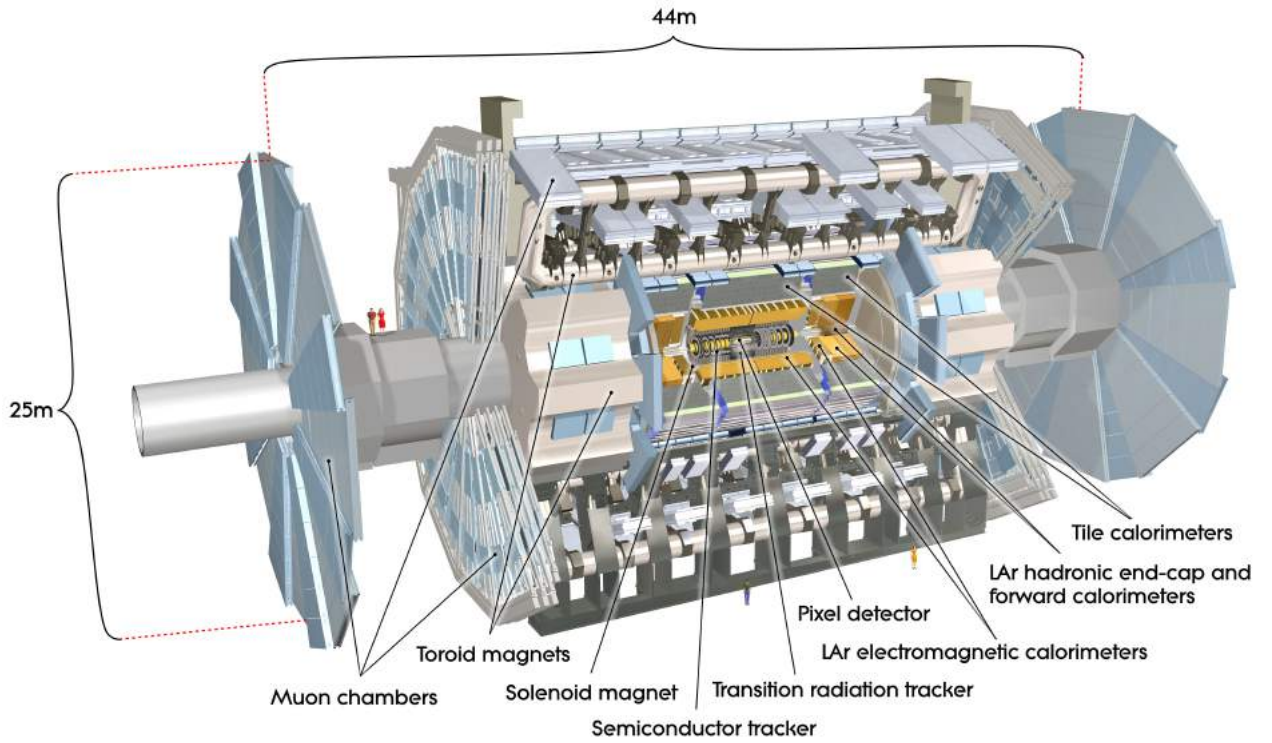


FIGURE 3.2: The full ATLAS detector showing the inner detector, calorimeter and muon spectrometer, and their components [17].

The transverse momentum, p_T , is the momentum in the x - y plane transverse to the beam axis, where momentum conservation is expected. It is defined as

$$p_T = \sqrt{p_x^2 + p_y^2}, \quad (3.3)$$

and is a key kinematic variable in this analysis, along with η .

In events where neutrinos (or other weakly interacting, yet-to-be-discovered particles) are present, the sum of momenta in the transverse plane for all detected particles will be non-zero. The missing transverse energy variable, E_T^{miss} , is used to account for this imbalance, and is defined similarly to p_T as

$$E_T^{miss} = \sqrt{E_{x,miss}^2 + E_{y,miss}^2}. \quad (3.4)$$

The missing transverse energy E_T^{miss} is measured from the vector sum of the transverse momenta of all reconstructed objects in the event [18].

The following descriptions of the subsystems of the ATLAS detector are based on [16].

3.2.1 Inner Detector

The inner detector is designed to achieve high-precision momentum and vertex resolution measurements amidst the very large track density created by the sheer volume of collisions occurring inside the ATLAS detector. It encompasses three independent but complementary sub-detectors which make up a tracking system, immersed in a 2 T axial magnetic field by its surrounding superconducting

solenoid, which bends charged particles and allows for measurements of their momentum.

The inner detector subsystem consists of precision tracking detectors (pixel detectors and a semiconductor tracker) which cover the region $|\eta| < 2.5$, and have high-resolution pattern recognition. These are used in conjunction with the straw tubes of the transition radiation tracker, providing continuous tracking to improve momentum resolution measurements. The insertible B-layer (IBL), a fourth layer of the pixel detector, provides an additional position measurement.

3.2.2 Calorimeters

The ATLAS calorimeters cover a range of $|\eta| < 4.9$, performing precision measurements of electrons and photons in the electromagnetic (EM) calorimeter, and jet reconstruction and E_T^{miss} measurements in the hadronic (HAD) calorimeter.

The electromagnetic (EM) calorimeter measures the energy of electrons, positrons and photons, using lead and liquid argon (LAr) as absorber and active materials respectively. It is divided into a barrel part ($|\eta| < 1.475$) and two end-caps ($1.375 < |\eta| < 3.2$). As charged particles traverse the EM calorimeter they cause EM showers, where ionization of the bulk material occurs. The current from the drifting ions is proportional to the energy deposited, which is then collected by electrodes.

The hadronic (HAD) calorimeter envelopes the EM calorimeter, and is optimised to measure the energy of particles which do not interact electromagnetically. It is divided into a tile calorimeter, with a barrel ($|\eta| < 1.0$) and extended barrel ($0.8 < |\eta| < 1.7$), a LAr hadronic end-cap calorimeter, covering ($1.5 < |\eta| < 3.2$), and a LAr forward calorimeter (FCal), increasing the calorimeter coverage to $|\eta| < 4.9$.

The FCal consists of copper, optimised for electromagnetic measurements, and tungsten, measuring mostly hadronic interactions. The hadronic end-cap calorimeter overlaps slightly with the forward calorimeter and the tile calorimeter, in order to reduce the drop in material density.

3.2.3 Muon Spectrometer

The muon spectrometer is the outermost sub-detector at ATLAS, and consists of a system of tracking chambers, immersed in a magnetic field generated by a system of three superconducting air-core toroidal magnets. The MS is designed to measure the momentum of muons which lose a negligible amount of energy while traversing the calorimeter. Combined with the inner detector tracking information, the muon spectrometer identifies muon track candidates.

The toroid magnets consist of a large barrel toroid, covering $|\eta| < 1.4$, and two smaller end-caps covering ($1.6 < |\eta| < 2.7$). The muons, which are electrically charged, bend in this magnetic field, allowing the subdetectors to make measurements of the muon's transverse momentum. Over most of the η range covered by the toroidal magnets, precision measurements of the track coordinates are made with the Monitored Drift Tubes. At higher η , Cathode Strip Chambers are used to perform measurements. The muon trigger system covers $|\eta| < 2.4$, providing bunch crossing identification, and measuring muon coordinates and momentum.

3.3 The ATLAS Trigger System

Due to the high collision rate and large cross-sections featured at the LHC, a trigger system has been implemented by the ATLAS collaboration to reject the high fraction of uninteresting events which are not useful for physics analyses produced in proton-proton collisions, and hence reduce the demand for data storage. For Run 2, the system is composed of separate hardware-based Level-1 (L1) and

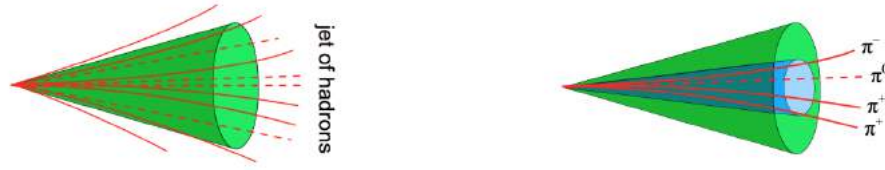


FIGURE 3.3: Typical signatures of a jet originating from a quark or gluon (left) and a jet originating from a hadronic tau decay (right) [19].

software-based High Level Trigger (HLT) systems. The L1 trigger reduces the event rate from 30 MHz to 100 kHz, with a decision time of approximately $2.5 \mu\text{s}$. The HLT further reduces the rate to 1 kHz. Results from the L1 and HLT trigger are processed to implement trigger *menus*, made up of combinations of trigger selections which are designed and implemented at each stage of the trigger to select specific signatures. These menus differ in their combinations of minimum p_T and isolation requirements across the L1 and High Level Triggers. They have different rate demands and are required to fit within global rate restrictions.

Of particular importance to this analysis are the tau trigger and the reconstruction algorithms in place at ATLAS. At the LHC there is a very large cross-section for jets originating from quarks or gluons, referred to as quantum-chromodynamic (QCD) jets, with features very similar to those of hadronically decaying tau leptons. Due to the high production of this *multi-jet* background, it is critical to use highly specialised tau triggers which are able to distinguish hadronically decaying taus from QCD jet events while maintaining the rate within bandwidth limits, and to implement further identification processes after the trigger. The reconstruction and identification of hadronic tau candidates at ATLAS therefore takes place both online (at trigger level) and offline (once the event has been saved).

The characteristic patterns of hadronic tau lepton decays include one or three charged tracks in the electromagnetic and hadronic calorimeters, which are utilised both online and offline in identifying hadronic tau decays against the large background of QCD multi-jet events. In order to distinguish between the two, the inner structure of the jets must be studied, since in contrast to the one or three tracks associated to hadronic tau jets, QCD jets contain a large number of tracks from charged hadrons, as depicted in Figure 3.3. These tracks are identified in the inner detector, and energy is deposited in the calorimeter. The one or three charged hadrons associated with a hadronic tau initiated jet form a narrow cone within the calorimeter, as shown in Figure 3.3. Compared to the quark or gluon initiated jets, jets from hadronic tau decays deposit very little energy in the calorimeter cells surrounding this inner cone, allowing for a level of isolation to be required surrounding the calorimeter energy deposits in the hadronic tau identification algorithms [19]. This process is further described in Section 3.4, and is used both online and offline. The online and offline reconstruction algorithms are very similar; notably, they both employ a Boosted Decision Tree (BDT) algorithm, a tau identification technique into which various discriminating variables are fed in order to reject jets. The BDT input variables are described in Section 3.4.3.

3.4 Reconstruction and identification of hadronic tau lepton decays

In the following sections, the online reconstruction will be described as it occurs at the trigger level in Section 3.4.1, followed by a description of the offline reconstruction and identification algorithms in Section 3.4.2. A further description is available at [8], [20], [21] and [22].

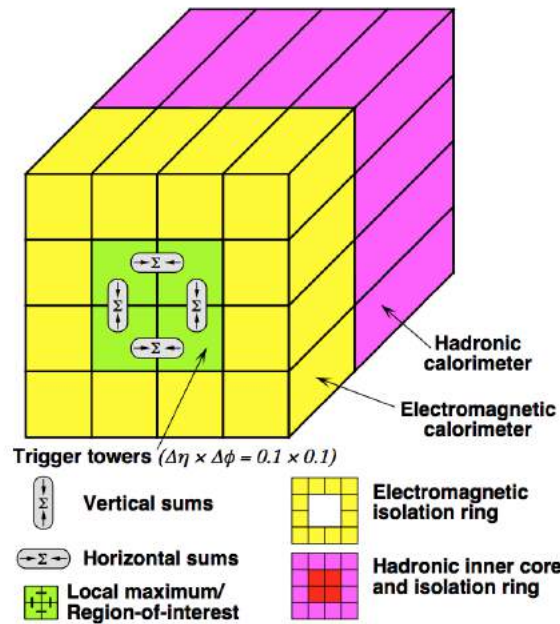


FIGURE 3.4: The 2×2 trigger tower in the electromagnetic calorimeter which identifies a RoI in the tau trigger algorithm [22].

3.4.1 Online reconstruction

Level 1

At Level 1, the tau trigger records a *Region of Interest (RoI)* corresponding to a $\tau_{\text{had,vis}}$ candidate as a 2×2 trigger tower cluster in the EM calorimeter for which the sum of transverse energy from at least one of its four neighbouring towers exceeds a predefined threshold, which depends on the trigger menu. Jet RoIs are defined as 4×4 trigger tower clusters for which the summed EM and HAD p_T exceeds predefined thresholds, surrounding a core 2×2 trigger tower which is a local maximum [22]. This RoI in the calorimeters is illustrated in Figure 3.4.

The tau triggers in the EM and HAD calorimeters have a granularity of $\Delta\eta \times \Delta\phi = 0.1 \times 0.1$, with a coverage of $|\eta| < 2.5$, and are used to define a core region (0.2×0.2) and an isolation region (0.4×0.4) around the core in $\Delta\eta \times \Delta\phi$ space. When a RoI is identified, the geographical coordinates in η and ϕ are recorded if certain isolation and minimum energy requirements depending on the trigger menu in question are met. These coordinates define the distance parameter R , written

$$R = \sqrt{(\Delta\eta)^2 + (\Delta\phi)^2}. \quad (3.5)$$

The core region is then described by $\Delta R < 0.1$, and the isolation region is described by $\Delta R < 0.3$.

High Level Trigger

The RoI recorded by the L1 cluster is then used as input for the HLT, which is divided into three steps: calo-only preselection, track preselection, and offline-like selection. At each step, selections on the $\tau_{\text{had,vis}}$ candidate are made in order to reduce the rate of candidates proceeding to the following steps; namely, requirements are placed on the p_T , number of tracks, and BDT score assigned to the $\tau_{\text{had,vis}}$ candidate at the first, second, and third step respectively.

First, in calo-only preselection, the $\tau_{\text{had,vis}}$ candidate is reconstructed from calorimeter information. The center of the energy deposit and the transverse momentum belonging to the $\tau_{\text{had,vis}}$ candidate are measured from the isolation and core regions of the RoI respectively. The vectorial sum of the energies of the calorimeter clusters identified at L1 is used as a *jet seed* for the reconstruction of the $\tau_{\text{had,vis}}$ candidate. A dedicated tau energy calibration scheme (TES) is used to improve the energy measurement. This calibration scheme is derived from simulation as a function of the transverse momentum and pseudorapidity of the tracks, and includes pileup corrections. A minimum transverse momentum requirement, again dependent on the trigger menu, is placed on the candidate, which must be achieved in order to move to the track preselection stage.

A fast tracking algorithm then uses tracks with $p_T > 1.5$ GeV and $\Delta R < 0.3$ to calculate tracking observables and implement track isolation requirements to increase background rejection. For multi-track candidates, we require that

$$\frac{\sum_i p_{T,i,(0.1 < \Delta R < 0.3)}}{\sum_j p_{T,j,(\Delta R < 0.1)}} < 0.1. \quad (3.6)$$

Any single track candidates with a reconstructed track in the isolation region is rejected, since a single track associated to a hadronically decaying tau is expected to be confined to the narrow cone in the center of the jet, which corresponds to the core region. The tau vertex algorithm (TV) uses as input all $\tau_{\text{had,vis}}$ candidates in the core region around the jet seed direction. The p_T of all tracks associated with the candidate are summed, and the primary vertex candidate to which the largest fraction of the total p_T is attributed is chosen as the tau vertex. The vertex is used to ascribe a direction to the candidate, to associate tracks, and to build a coordinate system relative to the candidate. $\tau_{\text{had,vis}}$ candidates must satisfy $1 \leq N_{\text{core}}^{\text{track}} \leq 3$ and $N_{\text{iso}}^{\text{track}} \leq 1$ in order to pass to the final stage of the trigger.

The final stage of the HLT tau trigger is labelled offline-like selection since it closely mimics its offline counterpart, described in Section 3.4.2. This stage is executed only on candidates passing the preceding preselections, and consists of a precision tracking algorithm, which performs a more precise measurement of the tracks associated to the $\tau_{\text{had,vis}}$, as well as the application of a BDT algorithm. The input to the BDT algorithm are identification variables which combine the calorimeter and track information gathered across the L1 and previous steps of the HLT, and are built in order to suppress the background resulting from jets misidentified as hadronic taus. They are listed in Section 3.4.3. The implementation of these BDT input variables closely follows that of their offline counterparts [8], as described in Section 3.4.2.

3.4.2 Offline Reconstruction

Much like the online reconstruction algorithm, the offline reconstruction is seeded by the calorimeter energy deposits identified by the L1 trigger. In offline reconstruction, these seeds are reconstructed as individual jets using the anti- k_t algorithm with a distance parameter of $R = 0.4$. Transverse momentum is measured in a similar manner to the online method, and TES is again implemented. While this TES scheme closely follows that used during reconstruction online, there are small differences in the parametrisation by pile-up μ and track multiplicity; namely, in offline reconstruction the value for μ is updated for each luminosity block, whereas the online reconstruction uses a preliminary calibration, meaning that on average the online corrections are based on a μ which is slightly higher than the true value. Secondly, the online TES is not parametrised as a function of the candidate track multiplicity, since this information is not yet available. Instead, an inclusive TES is used, and the track multiplicity information gathered by the online reconstruction is used by the offline TES. In order to be considered a hadronic tau candidate, a jet must possess $p_T > 10$ GeV and $|\eta| < 2.5$.

Following the p_T requirement, a selection is made on the track multiplicity of the candidate using a two stage fast-tracking algorithm, which selects candidates with $1 \leq N_{\Delta R < 0.1}^{\text{trk}} \leq 3$, and $N_{0.1 < \Delta R < 0.3}^{\text{trk}} \leq 1$: between 1 and 3 tracks in the core region, and at most one track in the isolation region. HLT precision tracking is then run, and track multiplicities are assigned to the candidate. Events are required to have a primary vertex with at least three associated tracks, which must be in the core region.

At the final stage, a collection of variables built from the calorimeter information and tracking algorithms are input to a Boosted Decision Tree (BDT) which produces a score for the tau identification. The full list of variables is given in Section 3.4.3.

3.4.3 Identification variables

The variables input to the BDT algorithm are designed to distinguish hadronic taus from QCD jets, and are based on the information described in Sections 3.4.1 and 3.4.2. A correction depending linearly on the average number of interactions per bunch crossing computed from the instantaneous luminosity is applied to each variable except $f_{\text{iso}}^{\text{track}}$, to ensure that the BDT score does not vary under differing pile-up conditions [8]. Removing the correction for $f_{\text{iso}}^{\text{track}}$ yields an increased performance with no degradation of pile-up dependence. Separate BDT algorithms are trained for 1-track and 3-track candidates, as some variables apply only to one or the other. BDT algorithms are nearly uniform between online trigger and offline reconstruction, with only one exception; $|S_{\text{leadtrack}}|$ is computed online with respect to the beamspot position, and offline with respect to the primary vertex associated with the $\tau_{\text{had,vis}}$ candidate. The variables are summarised in Table 3.1, and are defined as follows:

f_{cent} : **Central energy fraction**

The fraction of the energy in the core region around the $\tau_{\text{had,vis}}$ candidate deposited in $\Delta R < 0.1$.

$f_{\text{leadtrack}}^{-1}$: **Leading track momentum fraction**

The ratio of the transverse energy sum in the core region to the transverse momentum of the highest- p_T charged particle in the core region.

R_{track} : **Track radius**

p_T weighted ΔR distance of the associated tracks to the $\tau_{\text{had,vis}}$ candidate direction, using only tracks in the core region.

$|S_{\text{leadtrack}}|$: **Leading track impact parameter significance**

Absolute value of the transverse impact parameter of the highest- p_T track in the core region, divided by its estimated uncertainty.

$f_{\text{iso}}^{\text{track}}$: **Fraction of tracks' p_T in the isolation region**

The ratio of the sum of the p_T of tracks in the isolation region to the sum of the p_T of all tracks associated to the $\tau_{\text{had,vis}}$ candidate.

ΔR_{Max} : **Maximum ΔR**

Maximum ΔR between a $\tau_{\text{had,vis}}$ candidate and its direction, considering only tracks in the core region.

$S_{\text{T}}^{\text{flight}}$: **Transverse flight path significance**

The decay length of the multi-track $\tau_{\text{had,vis}}$ candidate's secondary vertex in the transverse plane, divided by its estimated uncertainty.

m_{track} : **Track mass**

Invariant mass calculated from the sum of the four-momentum of all tracks in both the core and

isolation regions, assuming a pion mass for each track.

$f_{EM}^{\text{track-HAD}}$: **Fraction of EM energy from charged pions**

Fraction of the electromagnetic energy of the tracks associated with the $\tau_{\text{had,vis}}$ candidate in the core region.

$f_{\text{track}}^{\text{EM}}$: **Ratio of EM energy to track momentum**

The ratio of the sum of the cluster energy associated to a $\tau_{\text{had,vis}}$ candidate to the sum of the transverse momentum in the core region.

$m_{\text{EM+track}}$: **Track-plus-EM-system mass**

Invariant mass of the system composed of the tracks and up to two most energetic electromagnetic calorimeter clusters in the core region.

p_T **ratio: Ratio of track-plus-EM-system to p_T**

The ratio of the $\tau_{\text{had,vis}}$ candidate p_T as estimated using the vector sum of the track momenta and EM clusters in the core region to that estimated by calorimeter only measurement.

Variable	1-track	3-track
f_{cent}	•	•
$f_{\text{leadtrack}}^{-1}$	•	•
R_{track}	•	•
$ S_{\text{leadtrack}} $	•	
$f_{\text{iso}}^{\text{track}}$	•	
ΔR_{Max}		•
$S_{\text{T}}^{\text{flight}}$		•
m_{track}		•
$f_{EM}^{\text{track-HAD}}$	•	•
$f_{\text{track}}^{\text{EM}}$	•	•
$m_{\text{EM+track}}$	•	•
p_T ratio	•	•

TABLE 3.1: Discriminating variables used as input to the tau identification algorithm for 1-prong and 3-prong $\tau_{\text{had,vis}}$ candidates.

The BDT algorithm outputs a continuous score between 0, for background-like events, and 1, for signal-like events, for each $\tau_{\text{had,vis}}$ candidate. The candidate is labelled with one of three working points, *loose*, *medium*, and *tight*, listed here in order of decreasing signal efficiency and increasing background rejection, and defined according to the level of identification (BDT score) assigned to the candidate. The reconstruction efficiency is defined as the fraction of 1-prong (3-prong) tau decays that are reconstructed as 1-track (3-track) hadronic tau candidates. The identification efficiency is defined as the fraction of 1-prong (3-prong) tau decays that are reconstructed as 1-track (3-track) hadronic tau candidates, which also pass the BDT selection criteria. The baseline medium working point yields an efficiency of 96 % (82 %) for true 1-prong (3-prong) $\tau_{\text{had,vis}}$ that are reconstructed offline as 1-prong (3-prong) $\tau_{\text{had,vis}}$ and pass the HLT p_T and track multiplicity requirements..

Chapter 4

$Z \rightarrow \tau\tau$ Tag and Probe Analysis

In this section, the performance of the ATLAS tau trigger is evaluated by employing a tag-and-probe analysis using a sample enriched in $Z \rightarrow \tau\tau$ events, where one tau decays leptonically into a muon and the second tau decays hadronically. The tag-and-probe analysis is done by selecting events triggered by the presence of a muon (the tag), and a hadronically decaying tau lepton candidate (the probe) in the final state, which is reconstructed offline. Preselection requirements are placed on both the tag and the probe, as summarised Table 4.3. The tag-and-probe method allows for the selection of a sample of taus which is as unbiased by selection criteria as possible by exploiting the di-tau resonances of the Z boson.

This section is organised as follows; the data and Monte Carlo simulation which were used in the analysis is described in Section 4.1. The object and event selection is described in Section 4.2, including requirements made on the tag muon, probe tau, and general event selections. In Section 4.3, the background estimation is explained. Uncertainties on the measurement are described in Section 4.4. The kinematics of the tag and probe are plotted in Section 4.5, including the full background estimation. The online tau reconstruction algorithms are studied in Section 4.6, and the trigger efficiencies are presented in Section 4.7, with the derived scale factors following in Section 4.8. These scale factors are the comparison between the efficiency of the trigger in data and in simulation, and are used in other ATLAS analysis to make simulation more closely resemble data. Finally, a study of the HLT is given in Section 4.9, presenting the efficiencies at each of the selection steps discussed in Section 3.4.1, namely the p_T , track counting and BDT selection steps.

4.1 Data and Simulation

The data used in this analysis were compared with estimated background and signal events, produced using a combination of simulated samples and data-driven estimations, as will be described in Section 4.3. Simulated signal and background samples were produced using the Monte Carlo generators detailed in Table 4.1, and include simulations of the background processes, $W(\rightarrow \mu\nu) + \text{jets}$, $Z(\rightarrow \mu\mu) + \text{jets}$, and top events, including events with a single top t and $t\bar{t}$ events, as well as simulations of the signal process, $Z \rightarrow \tau\tau$. The simulations are used in the background estimation process, and the signal simulation is used in the comparison of efficiency in data to that in simulation.

The simulated samples were reconstructed with the same algorithms as the data, where a simulation of the ATLAS detector is interfaced with the process generator. The $\tau_{\text{had,vis}}$ reconstruction, identification and calibration are achieved using $Z \rightarrow \tau\tau$ events simulated using Powheg-Box [23, 24] and Pythia [25]. The muon and $\tau_{\text{had,vis}}$ candidates reconstructed in the simulation are calibrated using scale factors measured in data which restore the identification and reconstruction efficiency in data.

TABLE 4.1: Generators used in simulated samples. The following additional software is used in some cases: EvtGen to set the properties of the bottom and charm hadron decays, Photos++ for quantum electrodynamic emissions from electroweak vertices and charged leptons, Tauola for the decay of tau leptons and MadSpin for the decay of top quarks.

Process	ME	Non pert.	Misc.
W/Z +jets	Powheg-Box v2+CT10 [23, 24] [30, 31, 32, 33]	Pythia8+AZNLO +CTEQ6L1 [25, 29] [34]	EvtGen [26], Photos++ [27, 28]
$t\bar{t}$, single top Wt - and s -channel	Powheg-Box v2+CT10 [36]	Pythia6+P2012 +CTEQ6L1 [37, 38]	EvtGen MadSpin [35] Tauola [39], Photos++
single top t -channel	Powheg-Box v1+CT10f4	Pythia6+P2012 +CTEQ6L1	EvtGen, MadSpin

4.2 Object and Event Selection

During the analysis, selection requirements are placed on the individual objects in the events, as detailed in Sections 4.2.1 to 4.2.3, and on the tag-probe pair in Section 4.2.4. The requirements are summarised in Table 4.3.

4.2.1 Muon

The offline reconstructed tag muon is selected by requiring the lowest unprecaled muon trigger dependent on the data period in 2016. Precaled triggers are used to reduce trigger output by randomly resetting a given number of *passed* events to *fail*. Events are deemed to *pass* a trigger when they fulfil the requirements of the trigger and are saved for later analyses, and *fail* when they do not fulfil the requirements and are discarded. This is done particularly in the lower energy range of the collisions at the LHC where there is a greater volume of events. ATLAS analyses use unprecaled triggers as they are predominantly interested in the high- p_T regimes. Here, it is required that one of two HLT triggers is satisfied, one of which imposes isolation requirements, as described in Table 4.2.

TABLE 4.2: Triggers required for tag muon selection in various 2016 data periods

Data period	Integrated Luminosity	Triggers	Requirements
A	0.6 fb^{-1}	<i>HLT mu24 iloose</i> or <i>HLT mu40</i>	24 GeV HLT p_T , loose isolation 40 GeV HLT p_T
B-D ₃	5.6 fb^{-1}	<i>HLT mu24 imedium</i> or <i>HLT mu50</i>	24 GeV HLT p_T , medium isolation 50 GeV HLT p_T
D ₄	27.1 fb^{-1}	<i>HLT mu26 imedium</i> or <i>HLT mu50</i>	26 GeV HLT p_T , medium isolation 50 GeV HLT p_T

Muon candidates are reconstructed by combining an inner-detector track with a track from the muon spectrometer [40], and must pass calorimeter and track isolation requirements. A working point is defined in order to describe the isolation required of the tag muon, defined by the scalar sum of the transverse momenta of tracks within a cone of p_T -dependent size $< \min(10 \text{ GeV}/p_T, 0.3)$, centered on the lepton candidate track, and the sum of the calorimeter energy deposits in a cone of size $\Delta R < 0.2$ around the muon. These cones define two variables, the track-based isolation variable $p_T^{\text{varcone30}(\mu)}$,

defined as

$$p_T^{\text{varcone30}(\mu)} = \sum_{x, \Delta R(\mu, x) \leq \min\left(\frac{30}{100}, \frac{10 \text{ GeV}}{p_T^\mu}\right)} p_T^x, \quad (4.1)$$

where x is every track included in the cone excluding the μ , and the calorimeter based isolation variable $E_T^{\text{topo,cone20}(\mu)}$, defined as

$$E_T^{\text{topo,cone20}(\mu)} = \sum_{c, \Delta R(\mu, c) \leq \frac{20}{100}} E_T^c - \sum_{c, \Delta R(\mu, c) \leq \Delta R_{\text{core}}} E_T^c - \rho\pi \left(\left(\frac{20}{100} \right)^2 - \Delta R_{\text{core}}^2 \right), \quad (4.2)$$

where c are the calorimeter energy deposits surrounding the μ . These variables are used to define the isolation working point used in this analysis, *gradient* isolation, which requires $p_T^{\text{varcone30}(\mu)} \leq 0.12$, and $E_T^{\text{topo,cone20}(\mu)} \leq 0.1$. This working point is required in the signal region and inverted in a control region used to calculate the multi-jet background contribution, as described in Section 4.3.2. Corrections to the reconstruction efficiencies are applied to simulated samples, including corrections to the muon energy scale, muon energy resolution, identification and isolation.

4.2.2 Tau

Events are required to have no additional muons μ or electrons e , and at least one $\tau_{\text{had,vis}}$ candidate. The reconstruction and identification of hadronically decaying tau leptons has been described in Sections 3.4.1 and 3.4.2, including both the online and offline algorithms. In this analysis, the $\tau_{\text{had,vis}}$ probe is required to have $p_T > 25 \text{ GeV}$, $|\eta| < 2.5$ (excluding the region $1.37 < |\eta| < 1.52$), one or three core tracks and electric charge opposite to the charge of the muon. This charge requirement stems from the opposite charges required of the leptonic and hadronic taus. In the study of the online reconstruction algorithms, the candidate is required to fulfil the medium identification requirement. For the efficiency studies, candidates with each of the three identification working points are considered.

4.2.3 Further Object Selection

Events with electrons reconstructed with $p_T > 15 \text{ GeV}$, with $|\eta| < 2.5$ (excluding $1.37 < |\eta| < 1.52$) and passing the *loose* likelihood identification are vetoed [41]. Geometric overlap of objects with $\Delta R < 0.2$ is resolved by selecting only one of the overlapping objects in the following order of priority: muons, electrons, $\tau_{\text{had,vis}}$ and jets.

4.2.4 Event Selection

As indicated in Table 4.3, the purity of $Z \rightarrow \tau\tau$ events is enhanced with further requirements on the selected tag-probe pair. In order to reduce contamination by $W(\rightarrow \mu\nu) + \text{jets}$ events, a series of requirements are made on the transverse mass and $\Sigma \cos \Delta\phi$ variables attributed to the tag and probe pair in the signal region. The transverse mass

$$m_T(\mu, E_T^{\text{miss}}) = \sqrt{2p_T\mu E_T^{\text{miss}} (1 - \cos \Delta\phi(\mu, E_T^{\text{miss}}))} \quad (4.3)$$

is required to be less than 50 GeV, and the sum of the azimuthal angles of the muon and the $\tau_{\text{had,vis}}$ with the missing energy, defined as

$$\Sigma \cos \Delta\phi = \cos \Delta\phi(\tau_{\text{had,vis}}, E_T^{\text{miss}}) + \cos \Delta\phi(\mu, E_T^{\text{miss}}), \quad (4.4)$$

TABLE 4.3: Summary of the $Z \rightarrow \tau\tau$ event selection

Event selection	
Muon tag:	$\tau_{\text{had,vis}}$ probe:
Medium quality	jet BDT medium
Trigger-matched	Muon veto, no overlapping electron
$p_T > 26/28$ GeV	$p_T > 25$ GeV, $ q = 1$
$ \eta < 2.5$	$ \eta < 1.37, 1.52 < \eta < 2.47$
gradient isolation	1 or 3 core tracks
Tag-probe pair selection:	
μ and $\tau_{\text{had,vis}}$ with opposite electric charge	
No other μ or e	
Event:	
$m_T(\mu, E_T^{\text{miss}}) < 50$ GeV	
$\Sigma \cos \Delta\phi > -0.5$	
$45 \text{ GeV} < m_{\text{vis}}(\tau_{\text{had,vis}}, \mu) < 80$ GeV	

must be greater than -0.5. The $\Sigma \cos \Delta\phi$ variable plays a key role in the determination of the $W(\rightarrow \mu\nu + \text{jets})$ background, which is done using a data-driven method as described in Section 4.3.4.

4.3 Background Estimation

The following section introduces the backgrounds to the $Z \rightarrow \tau\tau$ signal, which have final states which may be misidentified as a hadronically decaying tau lepton in association with a muon. The method relies heavily on the definitions of *opposite-sign* (OS) and *same-sign* (SS) regions, which are defined by the charge product of the tag muon and hadronic tau probe. The signal region (Table 4.3) and the control regions (Table 4.4) used for calculations of the background are defined as opposite-sign. The same-sign version of a given region is then defined by flipping the charge-product in the definition of the region.

The main backgrounds to this measurement are multi-jet and $W(\rightarrow \mu\nu) + \text{jets}$ events, where a jet is misidentified as a $\tau_{\text{had,vis}}$. The multi-jet background, which is due to jets initiated by quarks or gluons, is described in Section 4.3.2. In the case of the $W(\rightarrow \mu\nu) + \text{jets}$ estimation, a predominantly data-driven method is used to estimate the background contribution, which is described in Section 4.3.4. The remaining backgrounds, namely $Z(\rightarrow \mu\mu) + \text{jets}$ and those containing top quarks, are modelled using simulation, as described in Section 4.3.3. Several control regions, detailed in Table 4.4, are defined in order to estimate these backgrounds or the factors which transfer them to the signal region. In the following, objects which are misidentified as taus are called *fakes*.

4.3.1 Methodology

The full estimate of the background in the opposite-sign signal region (SR) is written as

$$N_{\text{OS}}^{\text{fake}} = r_{QCD} \text{Data}_{\text{SS}} + W_{\mu\nu}^{\text{OS-SS}} + Z_{\mu\mu}^{\text{OS-SS}} + \text{top}^{\text{OS-SS}} \quad . \quad (4.5)$$

The method exploits charge asymmetry by determining the charge symmetric ($Q_\tau \times Q_\mu > 0$) and charge asymmetric ($Q_\tau \times Q_\mu < 0$) components of the background independently. The charge-asymmetric component of a given background is estimated in the relevant opposite-sign

TABLE 4.4: Summary of the control region selections used in background estimation

Background estimation control regions
r_{QCD} control region
Inverted muon <i>gradient</i> isolation $m_T(\mu, E_T^{miss}) < 50 \text{ GeV}$ $\Sigma \cos \Delta\phi > -0.5$
$kW^{OS(SS)}$ control region
Muon <i>gradient</i> Isolation $m_T(\mu, E_T^{miss}) > 60 \text{ GeV}$ $E_T^{miss} > 30 \text{ GeV}$
LSCDP control region
$m_T(\mu, E_T^{miss}) < 50 \text{ GeV}$ $\Sigma \cos \Delta\phi < -0.5$ $45 \text{ GeV} < m_{vis}(\tau_{had,vis}, \mu) < 80 \text{ GeV}$ Muons <i>gradient</i> isolation

control region, and the charge-symmetric component is estimated in the same-sign version of the same control region. The estimations are done separately because the expected number of background events depends on the charge-product between the tag and the probe.

The $r_{QCD}Data_{SS}$ term in Equation 4.5 describes the multijet background, and is estimated by measuring the data in the same-sign region, and then extrapolating to the opposite-sign signal region using a transfer factor r_{QCD} which is defined in Section 4.3.2. There is a negligible contamination of signal events, which are by definition opposite sign, in the same sign region; in principle, signal events can contaminate the same-sign region if the charge of the particles is misidentified, but this is rare. In fact, since no Monte Carlo estimations of the background were subtracted from data in the SS region before extrapolation to the signal region, this term contains the same-sign (charge-symmetric) contributions from all of the remaining backgrounds, as well as the estimation of the multi-jet background. It is for this reason that we simply add the charge asymmetric contributions for each background, subtracting the charge-symmetric backgrounds, so as not to over-count. The “OS – SS” superscript indicates this subtraction.

The control regions used to estimate the backgrounds described are described in Table 4.4 as follows: the r_{QCD} control region refers to the measurement of the r_{QCD} transfer factor, used for the multi-jets background estimation as detailed in Section 4.3.2. The $kW^{OS(SS)}$ control region is used in the measurement of the kW factors as detailed in Section 4.3.3, which are used to scale the Monte Carlo predictions of the lepton backgrounds to correct for possible mis-modellings by Monte Carlo simulation. kW^{OS} , which is used to scale simulation in the opposite-sign region, is measured in the defined control region with an opposite sign requirement, and vice versa for kW^{SS} . Finally, the LSCDP control region indicates the low $\Sigma \cos \Delta\phi$ region that is used to estimate the $W(\rightarrow \mu\nu) + \text{jets}$ background, described in Section 4.3.4. The remaining backgrounds, namely $Z(\rightarrow \mu\mu) + \text{jets}$ and top events, are estimated using pure Monte Carlo simulation in the signal region, and scaled with the kW factors.

4.3.2 Multi-jet Background

Multi-jet events contribute to the background as jets misidentified as $\tau_{had,vis}$. They form a significant component of the background, due to their high production cross-section and the similarities between hadronic tau decays and jets initiated by quarks or gluons. Feynman diagrams of leading order (LO)

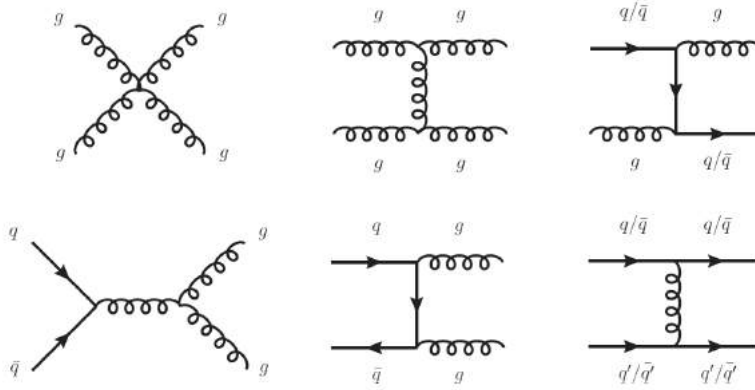


FIGURE 4.1: Examples of di-jet production at the LHC [42].

di-jet production modes are shown in Figure 4.1.

The r_{QCD} DataSS term in Equation 4.5 is used to model these events that arise from the mis-identification of multi-jet events. At present it is not possible to model this background using Monte Carlo, as the simulation of quark or gluon initiated jets is dominated by large uncertainties associated with the strong coupling constant. Instead, it is modelled using data in the SS control region, which is enriched in jets faking taus and where a negligible $Z \rightarrow \tau\tau$ contamination is found.

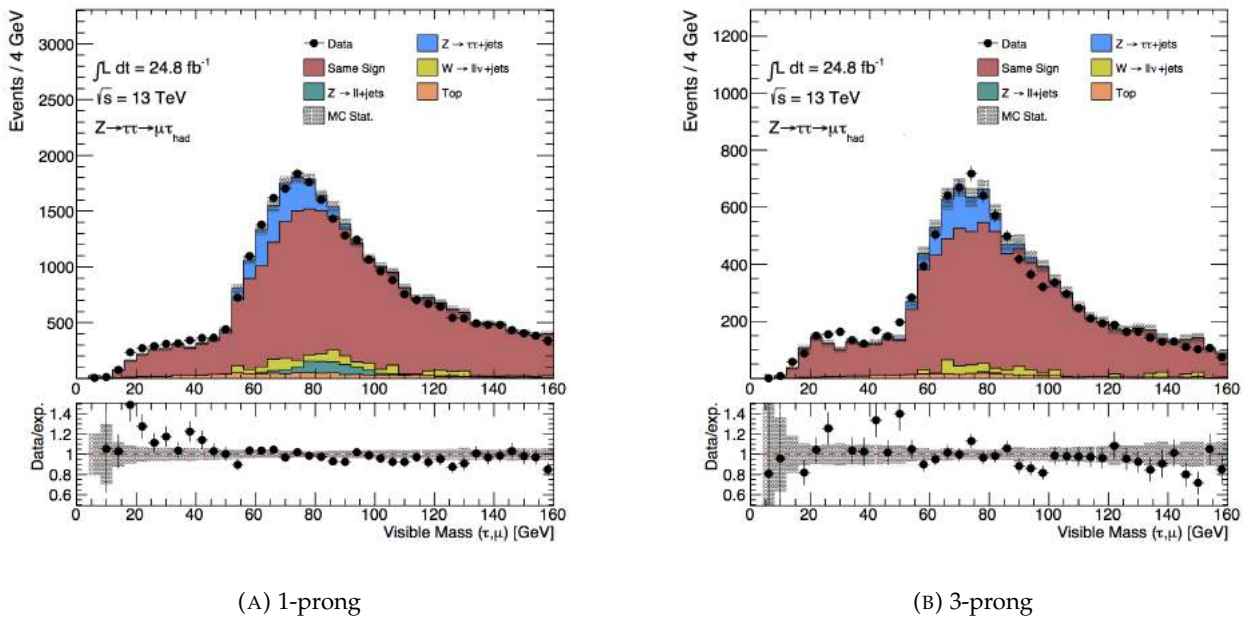


FIGURE 4.2: The distribution of m_{vis} , the invariant mass of the τ_{vis} and muon system in the multi-jet control region for a) 1-prong and b) 3-prong taus. Here, the tau candidate is required to pass medium identification. Monte Carlo samples are used for $Z \rightarrow \tau\tau$, $W(\rightarrow \mu\nu) + \text{jets}$, $Z(\rightarrow \mu\mu) + \text{jets}$ and top events. The error band contains only statistical uncertainty.

Since the occurrence of multi-jet events is not symmetric between same-sign and opposite-sign regions, the normalisation of the SS data to the OS region is corrected using the r_{QCD} factor. This is measured in a multi-jet enriched control region, labelled ' r_{QCD} control region' in Table 4.4 and obtained by inverting the isolation requirement around the tag muon, which defines a control region which is orthogonal to

the signal region. The r_{QCD} factor is the ratio of the number of multi-jet events in the opposite sign r_{QCD} control region to those in the same-sign r_{QCD} control region. The r_{QCD} factor is measured both before and after the event has been selected by the tau trigger, and is parametrised as a function of the probe $\tau_{had,vis}$ track multiplicity and the muon p_T . r_{QCD} is parametrised as a function of the muon p_T in order not to introduce a p_T dependent bias in the r_{QCD} control region. This is because the r_{QCD} factor is measured in a region where muon isolation is inverted, but data are collected online using an isolated low p_T muon trigger and a high p_T muon trigger with no isolation requirement. It is possible that the online isolation requirement might bias the p_T of the muon, hence the topology of the event, and hence the r_{QCD} factor. This can be mitigated by paramtrising in muon p_T .

The control region used to measure the r_{QCD} factor is shown in Figure 4.2. It is clear that this region is dominated by multi-jet events, labelled ‘‘Same Sign’’, with very little contamination by signal or other background events. The values for the r_{QCD} factor range between 1.16 and 1.55 and their uncertainties are approximately 5 %.

4.3.3 Lepton Backgrounds

A further source of background is due to the production of events containing leptons, namely events containing single top quarks or $t\bar{t}$ pairs, collectively termed top events, or events where a Z decays into a di-muon pair with associated jets. During top events, the top decays into a W boson and a b quark ($t \rightarrow Wb$). The signature of top events is dictated by the W boson decay mode; the production of a muon or electron from the W decay with associated QCD jets resembles the signal in this analysis. Feynman diagrams for the production of these top processes are shown in Figure 4.3. Events containing an electron or two muons are vetoed in this analysis, so only a very small fraction of $Z \rightarrow \mu\mu$ events are able to contaminate the signal region.

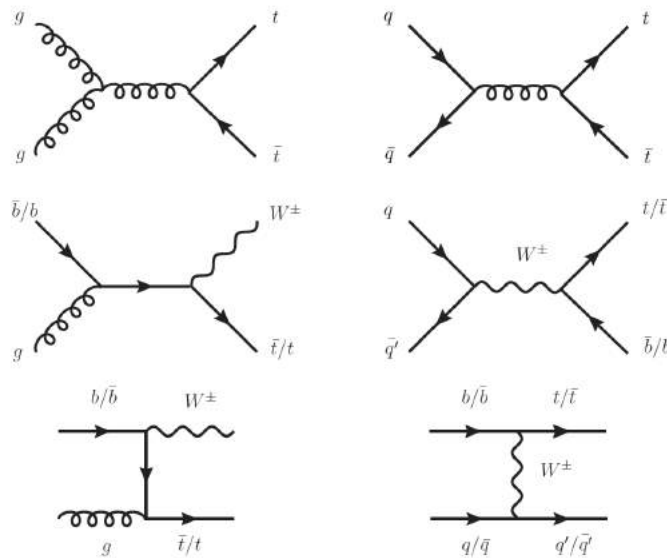


FIGURE 4.3: Examples of top production at the LHC [42].

It is expected that there will be a contribution of events containing true hadronically decaying taus in the $t\bar{t}$ simulation, due to the $t\bar{t}$ decay processes represented in Figure 4.4, where a top may decay into a τ and its associated neutrino via a W boson. This means that a portion of the simulated top events should be considered signal rather than background. The simulated top events containing a true τ are identified and extracted from the top background Monte Carlo simulation, and are added to the $Z \rightarrow \tau\tau$ simulation. The signal simulation and top simulation samples containing hadronic taus are referred to collectively as *true taus*. These backgrounds are represented by the terms $Z\mu\mu^{OS-SS}$ and top^{OS-SS} in

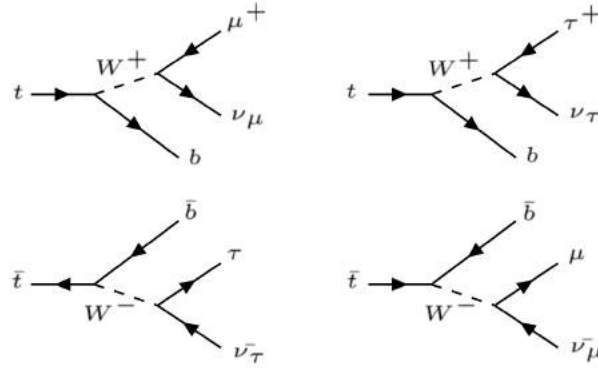
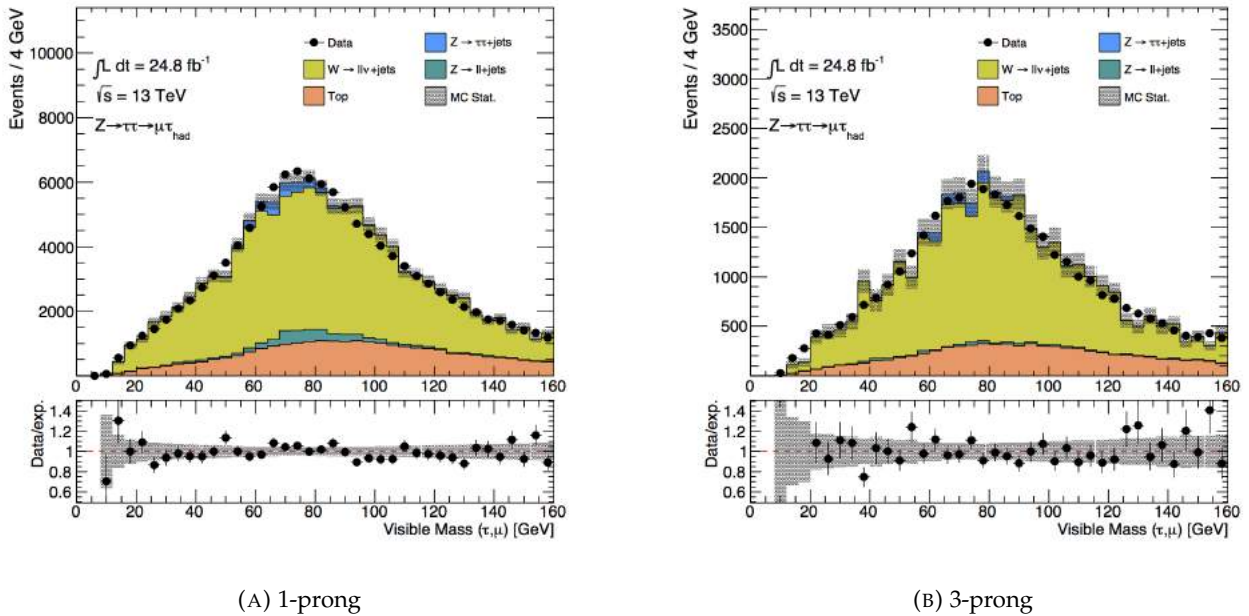


FIGURE 4.4: Feynman diagrams of $t\bar{t}$ decays where a true τ is produced from one top.

Equation 4.5, denoting the charge-asymmetric contributions from $Z(\rightarrow \mu\mu) + \text{jets}$ and top quark events to be added to the charge-symmetric components already modelled by the $r_{QCD}Data_{SS}$ term. They are estimated, using Monte Carlo simulation, as:

$$N^{OS-SS} = kW^{OS}N^{OS} - kW^{SS}r_{QCD}N^{SS} \quad (4.6)$$

where $N^{OS(SS)}$ is the $Z(\rightarrow \mu\mu) + \text{jets}$ or the top contribution in the opposite-sign (same-sign) region estimated using simulation, and $kW^{OS(SS)}$ is a data-driven correction used to scale Monte Carlo based predictions to account for possible mis-modelling of the misidentification probability in simulation. The kW corrections are measured in the ‘ $kW^{OS(SS)}$ control region’ enriched in $W(\rightarrow \mu\nu) + \text{jets}$ events, defined in Table 4.4, and plotted in Figure 4.5. It is clear that this region is dominated by $W(\rightarrow \mu\nu) + \text{jets}$ events, with some contamination from the top background.



(A) 1-prong

(B) 3-prong

FIGURE 4.5: The distribution of m_{vis} , the invariant mass of the τ_{vis} and muon system, in the control region used to calculate the kW factors for a) 1 prong and b) 3 prong taus. Here, the tau candidate is required to pass medium identification. The background is estimated using Monte Carlo samples only. The error band contains only statistical uncertainty.

In order to calculate the kW^{OS} correction, the $Z \rightarrow \tau\tau$ simulation and the simulation of all backgrounds

except $W(\rightarrow \mu\nu) + \text{jets}$ are subtracted from data in the kW^{OS} control region in order to obtain the $W(\rightarrow \mu\nu) + \text{jets}$ estimation as expected from data. The kW^{OS} correction factor is the ratio between this measured $W(\rightarrow \mu\nu) + \text{jets}$ contribution, and that predicted directly by simulation. The same process is followed for the measurement of the kW^{SS} correction, using the same-sign version of the control region. The $kW^{\text{OS(SS)}}$ factors, although measured in a region dominated by $W(\rightarrow \mu\nu) + \text{jets}$ events, are assumed to hold for corrections of the $Z(\rightarrow \mu\mu) + \text{jets}$ and top events, as the scaling of Monte Carlo simulations of jets faking taus is fairly uniform. The values for the $kW^{\text{OS(SS)}}$ factors range between 1.35 and 1.94, and their uncertainties are approximately 2%.

4.3.4 $W(\rightarrow \mu\nu) + \text{jets}$ Background

Another significant component of the background is the production of a W boson in association with a jet, where the W decays into a muon and a neutrino. This production mode, which has a high cross-section at the LHC, is depicted in Figure 4.6. Due to the high integrated luminosity achieved during 2016 of 33.3 fb^{-1} , there is a far greater volume of data available than there is Monte Carlo, making the statistical error associated to any calculations lesser in data. It is of interest to minimise the statistical error associated with any background estimations, and so in this analysis a new data-driven approach to the modelling of the $W(\rightarrow \mu\nu) + \text{jets}$ background has been devised, in order to limit the dependence on Monte Carlo for this important background estimation. It should be noted that there must still be a dependence on Monte Carlo in the subtraction of the remaining backgrounds and signal sample in the estimation of the distribution, as well as in measurement of the transfer factor.

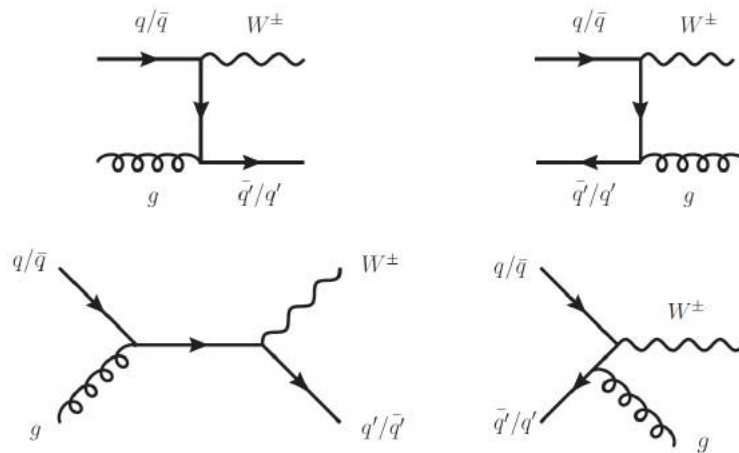


FIGURE 4.6: Examples of W boson production in association with a jet at the LHC [42].

The $W(\rightarrow \mu\nu) + \text{jets}$ background is estimated using a subtraction of simulated background events from data in the LSCDP control region as described in Table 4.4, defined by removing the $m_{\text{T}}(\mu, E_{\text{T}}^{\text{miss}})$ selection and inverting the $\Sigma \cos \Delta\phi$ requirement imposed on the signal region. This LSCDP region is orthogonal to the signal region, and is designed such that the $W(\rightarrow \mu\nu) + \text{jets}$ distribution will mimic that in the signal region with minimal contamination by other backgrounds or signal events. The LSCDP control region is dominated by $W(\rightarrow \mu\nu) + \text{jets}$ events with almost no real taus or contamination by other background processes, as is seen in Figure 4.9, where the transverse mass of the event is plotted using Monte Carlo simulation. It is expected that the $W(\rightarrow \mu\nu) + \text{jets}$ distribution in the LSCDP region will have a different normalisation to that in the signal region, so the estimated background is then normalised to the signal region using a transfer factor, f_W , as described in Section 4.3.4.

Before the method is accepted, the validity of the LSCDP region is tested by comparing the shape of the p_T distribution for the $W(\rightarrow \mu\nu) + \text{jets}$ Monte Carlo samples in the LSCDP region with the shape in the signal region, both normalised to 1. Should the distribution of $W(\rightarrow \mu\nu) + \text{jets}$ events in the LSCDP region mimic that in the signal region, the normalised distributions would agree within uncertainty. Sufficiently good agreement between the control regions is shown in Figures 4.7 and 4.8, indicating that the LSCDP region is a valid choice to estimate the shape of the $W(\rightarrow \mu\nu) + \text{jets}$ distribution.

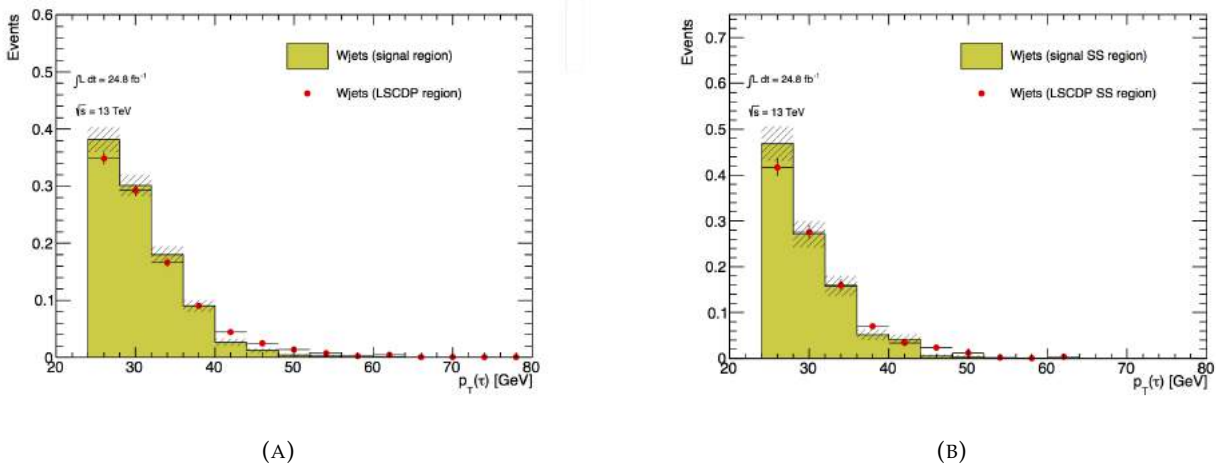


FIGURE 4.7: The shape of the $W(\rightarrow \mu\nu) + \text{jets}$ Monte Carlo prediction in the signal region compared to the shape in the LSCDP region for a) opposite sign and b) same sign regions, where SR denotes the $Z \rightarrow \tau\tau$ signal region. The error bars indicate the statistical uncertainty on the Monte Carlo samples.

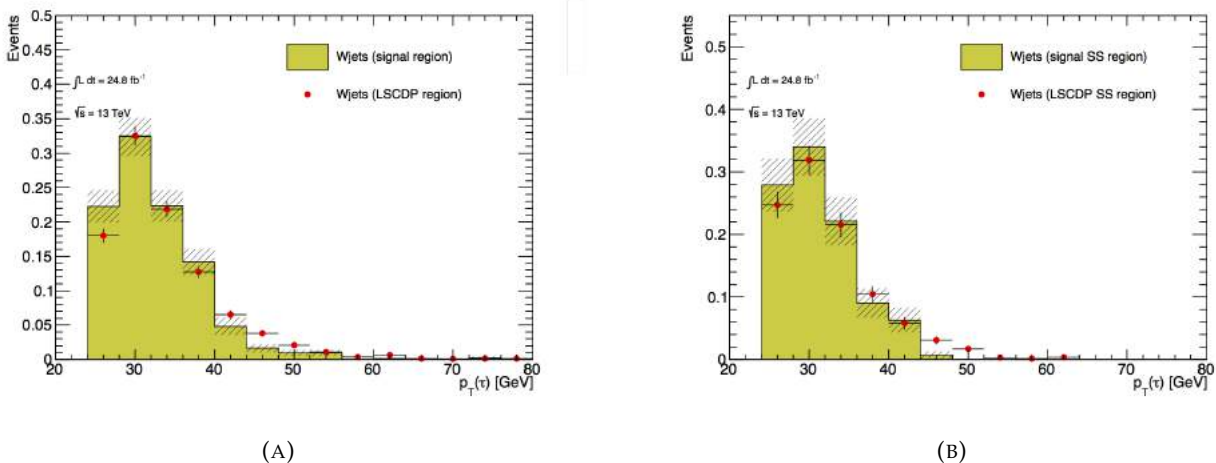


FIGURE 4.8: The shape of the $W(\rightarrow \mu\nu) + \text{jets}$ Monte Carlo prediction in the signal region after the τ 25 medium trigger compared to the shape in the LSCDP region for a) opposite sign and b) same sign regions, where SR denotes the $Z \rightarrow \tau\tau$ signal region. The error bars indicate the statistical uncertainty on the Monte Carlo samples.

$W(\rightarrow \mu\nu) + \text{jets}$ Shape

In order to obtain the shape of the $W(\rightarrow \mu\nu) + \text{jets}$ background, the opposite-sign data are measured in the LSCDP region and the remaining backgrounds (namely the SS data scaled by r_{QCD} and the

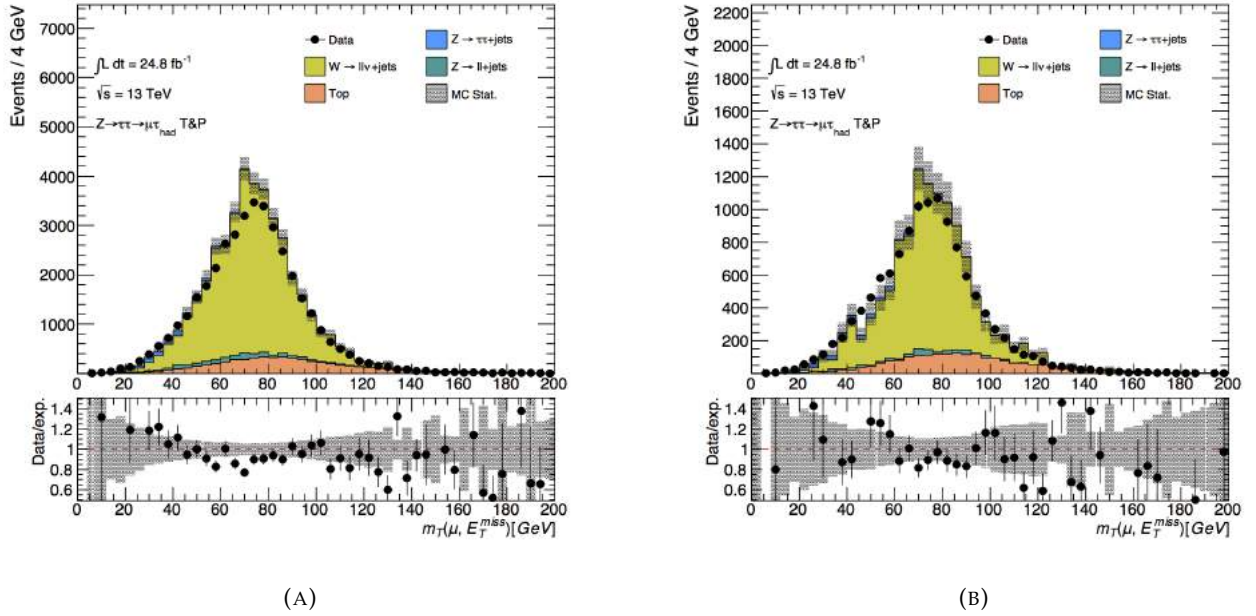


FIGURE 4.9: The distribution of the transverse mass for the E_T^{miss} and muon system m_T in the $W(\rightarrow \mu\nu) + \text{jets}$ region for a) 1-prong and b) 3-prong taus. The error band contains only statistical uncertainty.

expected small contributions from $Z(\rightarrow \mu\mu) + \text{jets}$ and top events based on simulation) and the $Z \rightarrow \tau\tau$ signal contribution as predicted by simulation, are subtracted, yielding the $W(\rightarrow \mu\nu) + \text{jets}$ distribution as predicted by data. This distribution has the incorrect normalisation, which is then rectified by the correction factor described below.

Correction Factor

The expected distribution of $W(\rightarrow \mu\nu) + \text{jets}$ events in the signal region is then normalised correctly by correcting the shape as obtained from the LSCDP data with a factor, fW , measured in simulated events. This is the event ratio of the Monte Carlo prediction of the $W(\rightarrow \mu\nu) + \text{jets}$ distribution in the signal region to the LSCDP control region, where simulation-based signal and background predictions and the same-sign component corrected by r_{QCD} are subtracted in each region. This normalisation correction for $W(\rightarrow \mu\nu) + \text{jets}$ is parametrised as a function of the tau track multiplicity and p_T , and is given by

$$fW = \frac{(W(\rightarrow \mu\nu) + \text{jets})_{\text{SR}}^{\text{OS}} - r_{QCD}(W(\rightarrow \mu\nu) + \text{jets})_{\text{SR}}^{\text{SS}}}{(W(\rightarrow \mu\nu) + \text{jets})_{\text{LSCDP}}^{\text{OS}} - r_{QCD}(W(\rightarrow \mu\nu) + \text{jets})_{\text{LSCDP}}^{\text{SS}}}. \quad (4.7)$$

The full form of the $W(\rightarrow \mu\nu) + \text{jets}$ background estimation is then written

$$W(\rightarrow \mu\nu) + \text{jets} = fW(\text{Data}_{\text{LSCDP}}^{\text{OS}} - r_{QCD}\text{Data}_{\text{LSCDP}}^{\text{SS}} - \text{MC}), \quad (4.8)$$

where the r_{QCD} factor is as defined in Section 4.3.2, and MC denotes all other Monte Carlo contributions in the LSCDP region.

The contribution by the $W(\rightarrow \mu\nu) + \text{jets}$ background in the signal region is represented in Equation 4.5 by the term $W_{\mu\nu}^{\text{OS-SS}}$. This accounts for the charge-asymmetric component of the $W(\rightarrow \mu\nu) + \text{jets}$ background, which is added to the charge-symmetric component included in the $r_{QCD}\text{Data}_{\text{SS}}$ term.

4.4 Uncertainties

This analysis takes into account both statistical and systematic uncertainties on the measurements. The statistical and systematic uncertainties considered are related to the muon trigger, reconstruction and selection efficiency of the tag muon, and the r_{QCD} and kW factors. Further systematic uncertainties are included for $\tau_{\text{had,vis}}$ reconstruction and identification efficiencies, τ -electron overlap removal, μ energy scale, the soft term of the E_T^{miss} , and pile-up reweighting. The overall systematic uncertainty is measured by comparing the yields of background events with and without each systematic variation.

Systematic uncertainties on the r_{QCD} factor are estimated by varying the width of the cones that define the *gradient* isolation requirement. This is done by considering the variations on r_{QCD} that occur within $0.1 \leq p_T^{\text{varcone30}(\mu)} \leq 0.4$ and $0.1 \leq E_T^{\text{topo,cone20}(\mu)} \leq 0.4$, which are considered independently for each r_{QCD} measurement. For each measurement of r_{QCD} , the largest of the two variations is chosen as the systematic uncertainty.

Systematic uncertainties on the kW factors are measured by varying the selection on $m_T(\mu, E_T^{\text{miss}})$ between 60 GeV and 100 GeV, which defines the $W(\rightarrow \mu\nu) + \text{jets}$ control region where the factors are measured.

Table 4.5 reports the observed data and expected signal and background contributions in the OS signal region, including statistical and systematic uncertainties. The selected sample of events has an estimated purity of 72% for true $\tau_{\text{had,vis}}$ probes.

TABLE 4.5: Observed and expected event yields after the $Z \rightarrow \tau\tau$ tag-and-probe event selection in the 33.3 fb^{-1} of 2016 pp collision data. Only statistical uncertainties are reported.

Contribution	Yield (\pm stat. \pm syst. uncert.)
r_{QCD} Datass	$19000 \pm 170 \pm 600$
$W\mu\nu^{\text{OS-SS}}$	$5300 \pm 80 \pm 500$
$Z\mu\mu^{\text{OS-SS}}$	$280 \pm 70 \pm 70$
$\text{top}^{\text{OS-SS}}$	$880 \pm 80 \pm 120$
True $\tau_{\text{had,vis}}$ ($Z \rightarrow \tau\tau$ and top)	$64400 \pm 500 \pm 1400$
Total expected	$89900 \pm 500 \pm 1600$
Data	89364
Data/Exp.	0.99 ± 0.02
Purity of true $\tau_{\text{had,vis}}$ probe	72%

4.5 Validation of the background estimation method

The kinematic variables of the tag muon and probe tau are plotted as a validation of the background estimation methods described above. Figures 4.10 and 4.11 show the azimuthal angle ϕ , pseudorapidity η and transverse momentum p_T of the tag muon. Figures 4.12 and 4.13 show the transverse momentum p_T , the pseudorapidity η , the core track multiplicity and the jet BDT score of the selected offline $\tau_{\text{had,vis}}$ probes, for inclusive 1-prong and 3-prong taus, before and after the 25 GeV tau trigger requirement respectively.

On these plots and all two-panel plots following, the ratio of data to simulation is shown in the bottom panel to provide a visual understanding of their agreement. Should the background estimation be

correct in the kinematic plots, the predicted background + signal estimations should match the data, yielding a ratio of 1. The systematic and statistical uncertainties are combined and plotted in grey on both the top and bottom panels. A good agreement between observed data and estimated signal and background contributions is achieved, indicating the success of the background estimation methods.

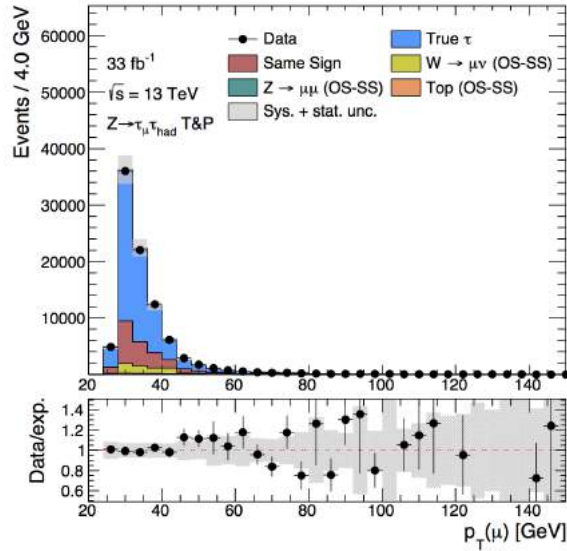


FIGURE 4.10: Kinematics and properties of the offline tag muon after the $Z \rightarrow \tau\tau$ tag-and-probe event selection. Plotted here is the transverse momentum p_T . Systematic and statistical uncertainties are added in quadrature.

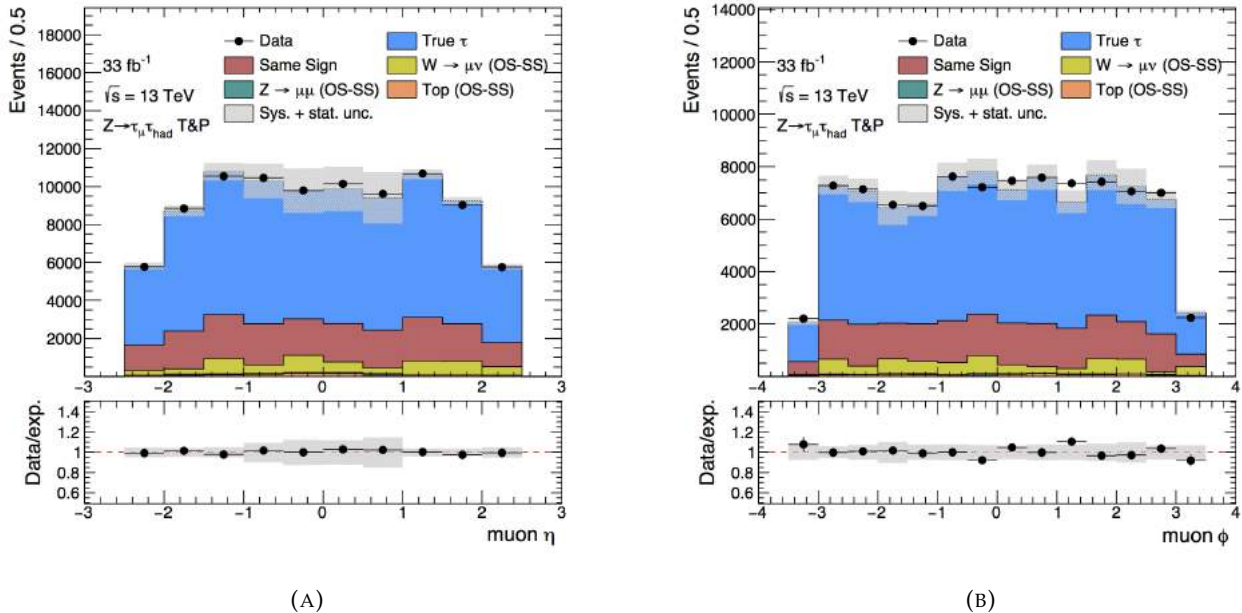
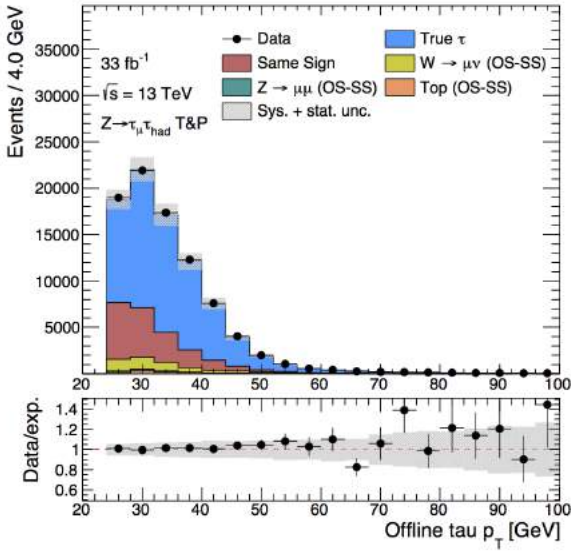
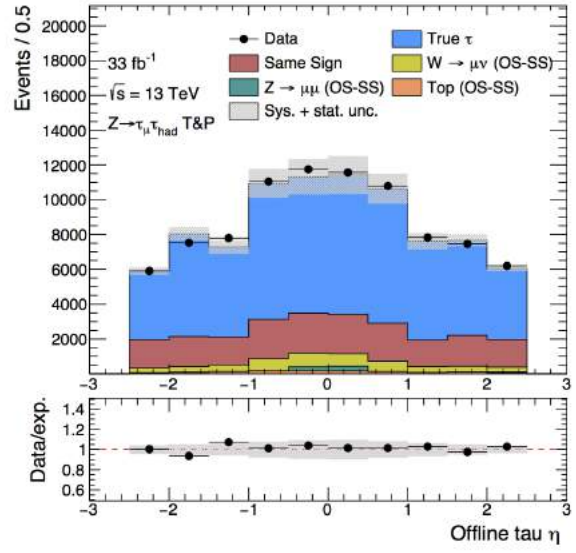


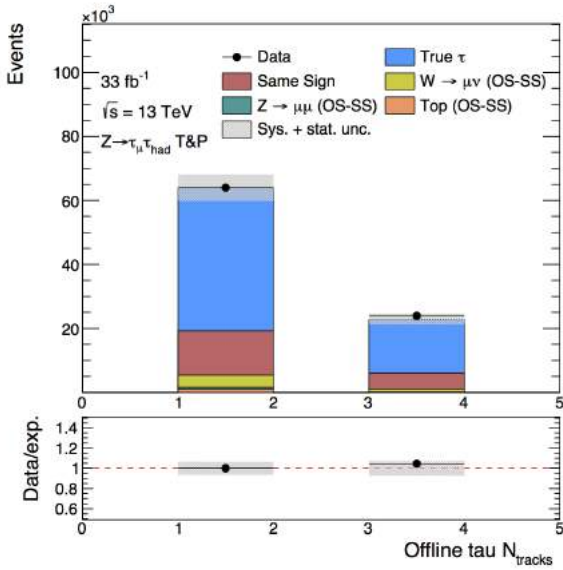
FIGURE 4.11: Kinematics and properties of the offline tag muon after the $Z \rightarrow \tau\tau$ tag-and-probe event selection, showing (a) the pseudorapidity and (b) the azimuthal angle. Systematic and statistical uncertainties are added in quadrature.



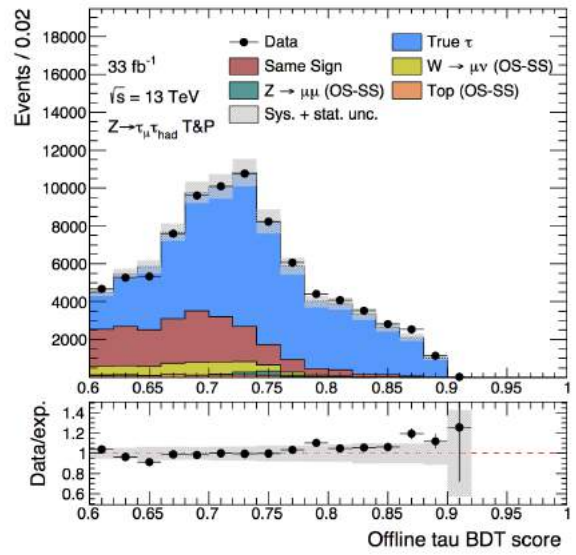
(A)



(B)

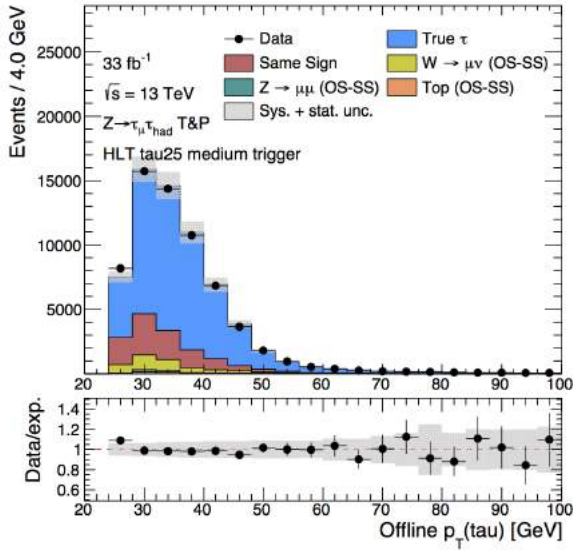


(C)

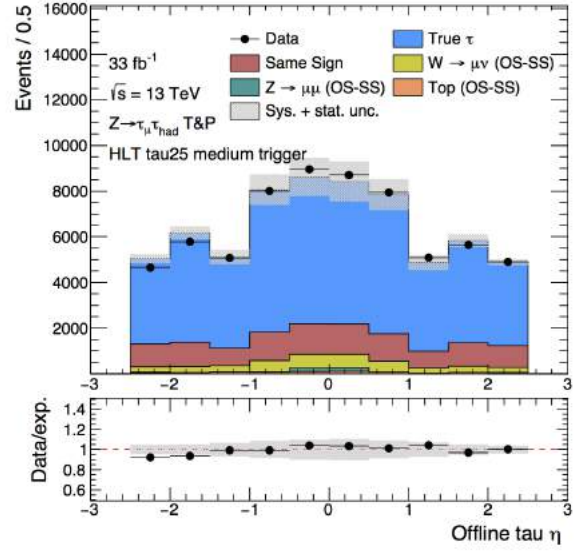


(D)

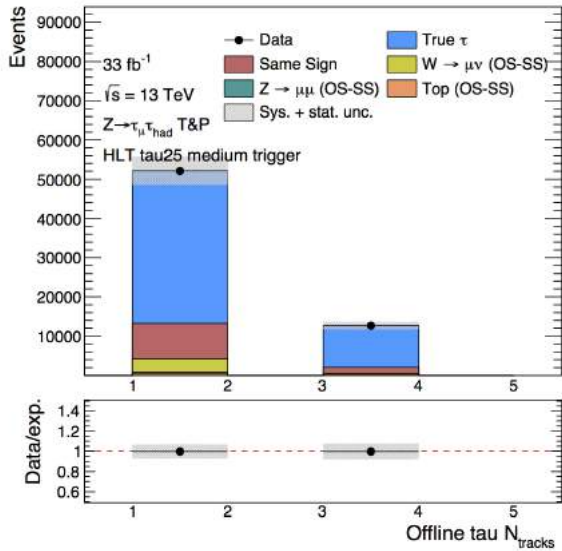
FIGURE 4.12: Kinematics and properties of the offline $\tau_{\text{had,vis}}$ probes after the $Z \rightarrow \tau\tau$ tag-and-probe event selection showing a) transverse momentum, b) pseudorapidity, c) core track multiplicity and d) jet BDT score. Systematic and statistical uncertainties are added in quadrature.



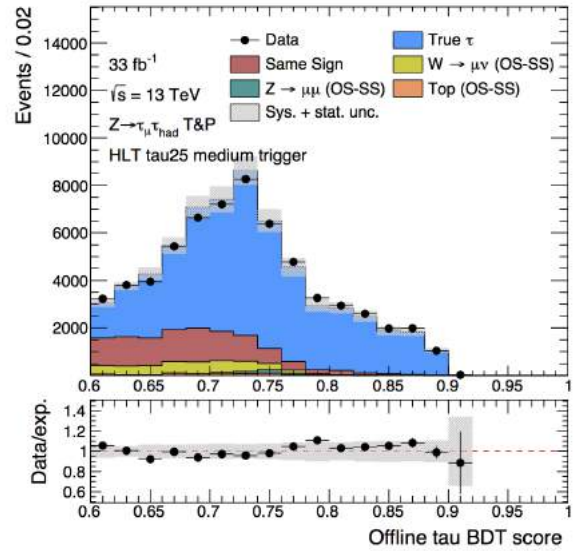
(A)



(B)



(C)



(D)

FIGURE 4.13: Kinematics and properties of the offline $\tau_{\text{had,vis}}$ probes passing the 25 GeV tau trigger after the $Z \rightarrow \tau\tau$ tag-and-probe event selection showing a) transverse momentum, b) pseudorapidity, c) core track multiplicity and d) jet BDT score. Systematic and statistical uncertainties are added in quadrature.

4.6 Online Tau Reconstruction Performance

As described above, the $\tau_{\text{had,vis}}$ reconstruction and identification relies on the BDT input variables, used to distinguish true tau candidates from QCD jets both online and offline. The online modelling and the performance of the $\tau_{\text{had,vis}}$ reconstruction in the tau trigger is validated by comparing the properties of the online $\tau_{\text{had,vis}}$ candidate between simulation and data, by plotting the BDT input variables for the candidate and its kinematics at the online level.

The online selection requires an isolated candidate with $E_T > 12$ GeV at L1, and $p_T > 25$ GeV at the HLT. No HLT identification or track multiplicity requirements have yet been applied to these candidates. However, the online candidates here have all been matched to an offline $\tau_{\text{had,vis}}$ candidate, where ‘matching’ refers to the topological compatibility of two objects. It should therefore be noted that this sample of online $\tau_{\text{had,vis}}$ candidates is biased by the identification and track multiplicity selections applied on the matching offline probe. Here and in all following plots, the background contributions as determined in Section 4 are plotted together as fakes.

Figures 4.14, 4.15 and 4.16 show transverse momentum p_T , pseudorapidity η , azimuthal angle ϕ and core track multiplicity of the online $\tau_{\text{had,vis}}$ candidates as reconstructed at the final stage of the HLT tau trigger. It can be seen in Figure 4.16 that no HLT track multiplicity requirements have yet been performed, as candidates with up to 5 tracks are accepted. Figures 4.17 to 4.21 show the input variables used for the HLT BDT identification listed in Table 3.1. A good modelling is observed in all distributions.

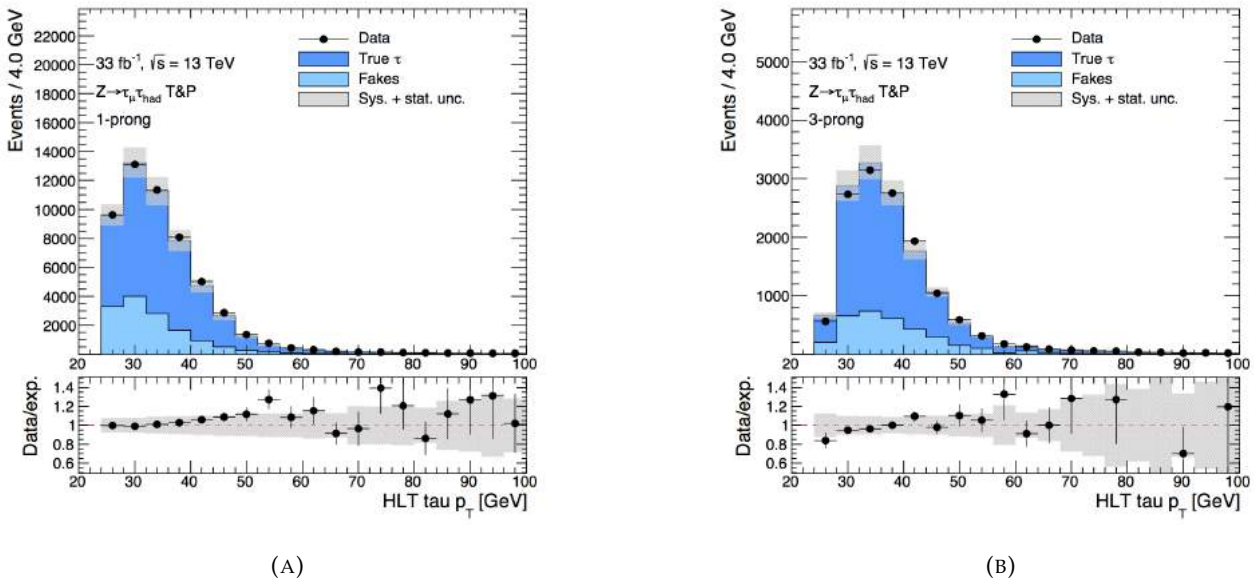


FIGURE 4.14: Distributions of HLT $\tau_{\text{had,vis}}$ p_T for online $\tau_{\text{had,vis}}$ candidates matched to an offline 1-prong (left) and 3-prong (right) $\tau_{\text{had,vis}}$ probe in the selected $Z \rightarrow \tau\tau$ events. Systematic and statistical uncertainties are added in quadrature.

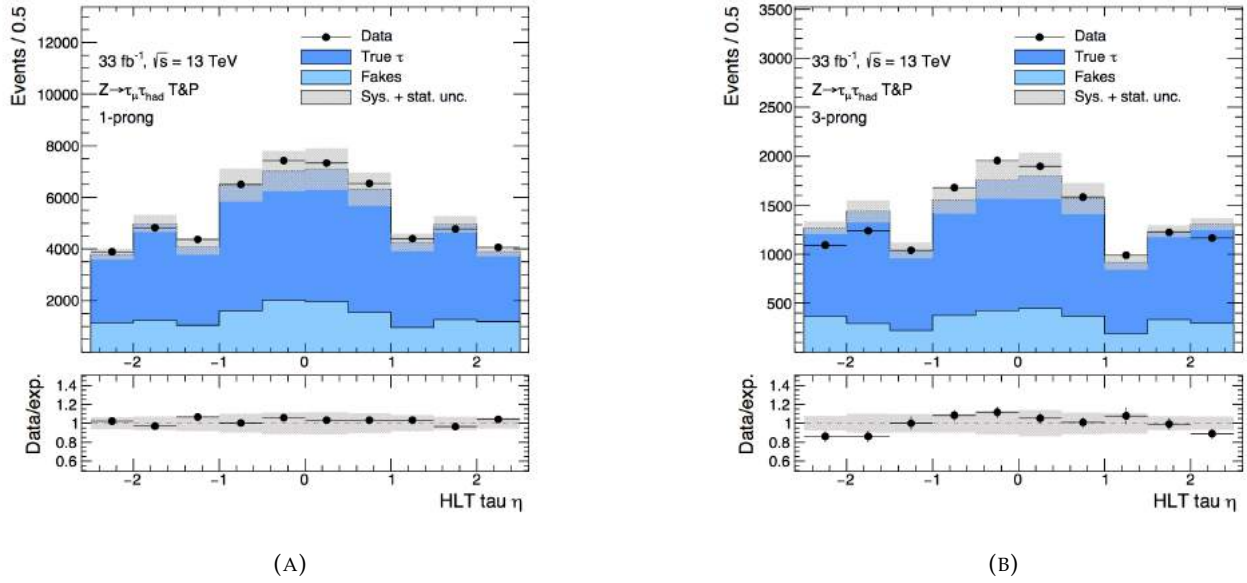


FIGURE 4.15: Distributions of HLT $\tau_{\text{had,vis}} \eta$ for online $\tau_{\text{had,vis}}$ candidates matched to an offline 1-prong (left) and 3-prong (right) $\tau_{\text{had,vis}}$ probe in the selected $Z \rightarrow \tau\tau$ events. Systematic and statistical uncertainties are added in quadrature.

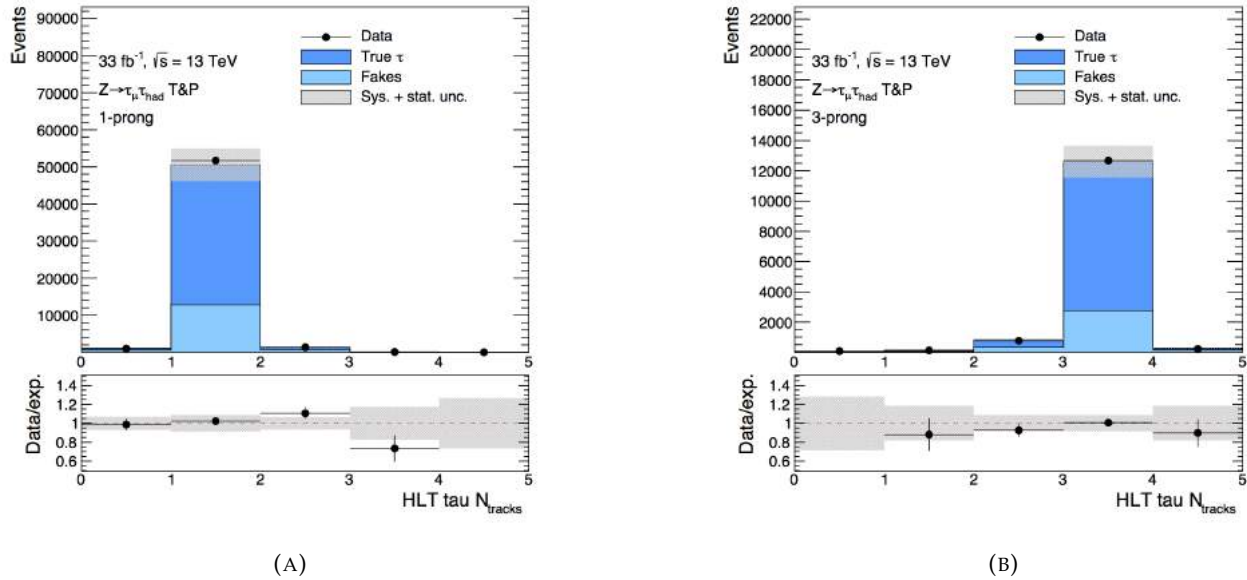


FIGURE 4.16: Distributions of HLT $\tau_{\text{had,vis}} N_{\text{core}}^{\text{trk}}$ for online $\tau_{\text{had,vis}}$ candidates matched to an offline 1-prong (left) and 3-prong (right) $\tau_{\text{had,vis}}$ probe in the selected $Z \rightarrow \tau\tau$ events. Systematic and statistical uncertainties are added in quadrature.

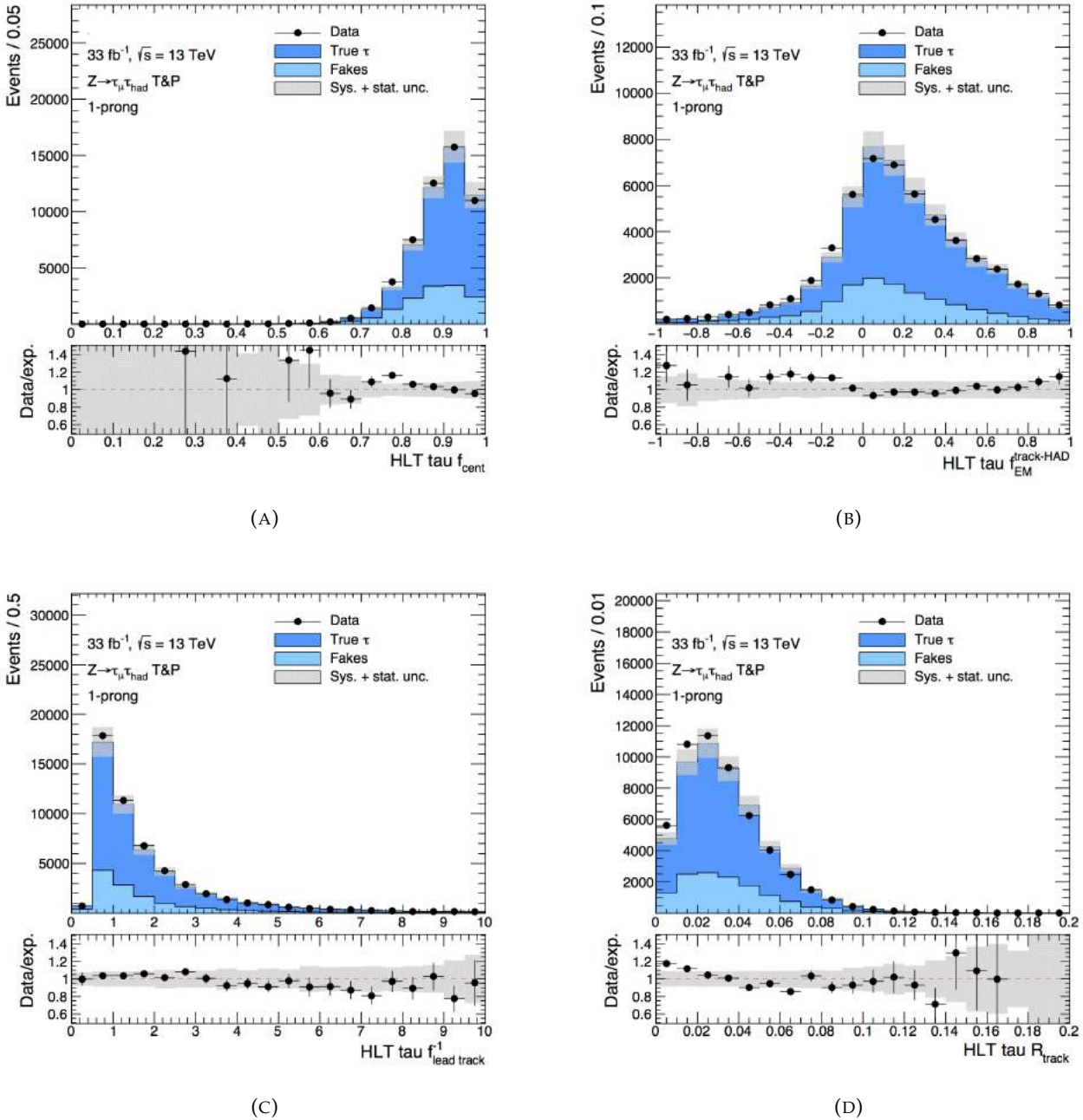


FIGURE 4.17: HLT BDT inputs for online $\tau_{\text{had,vis}}$ candidates matched to an offline 1-prong $\tau_{\text{had,vis}}$ probe in the selected $Z \rightarrow \tau\tau$ event candidates. Shown here are a) central energy fraction (f_{cent}), b) fraction of EM energy from charged pions ($f_{\text{EM}}^{\text{track-HAD}}$), c) leading track momentum fraction ($f_{\text{lead track}}^{-1}$), and d) track radius (R_{track}). Systematic and statistical uncertainties are added in quadrature.

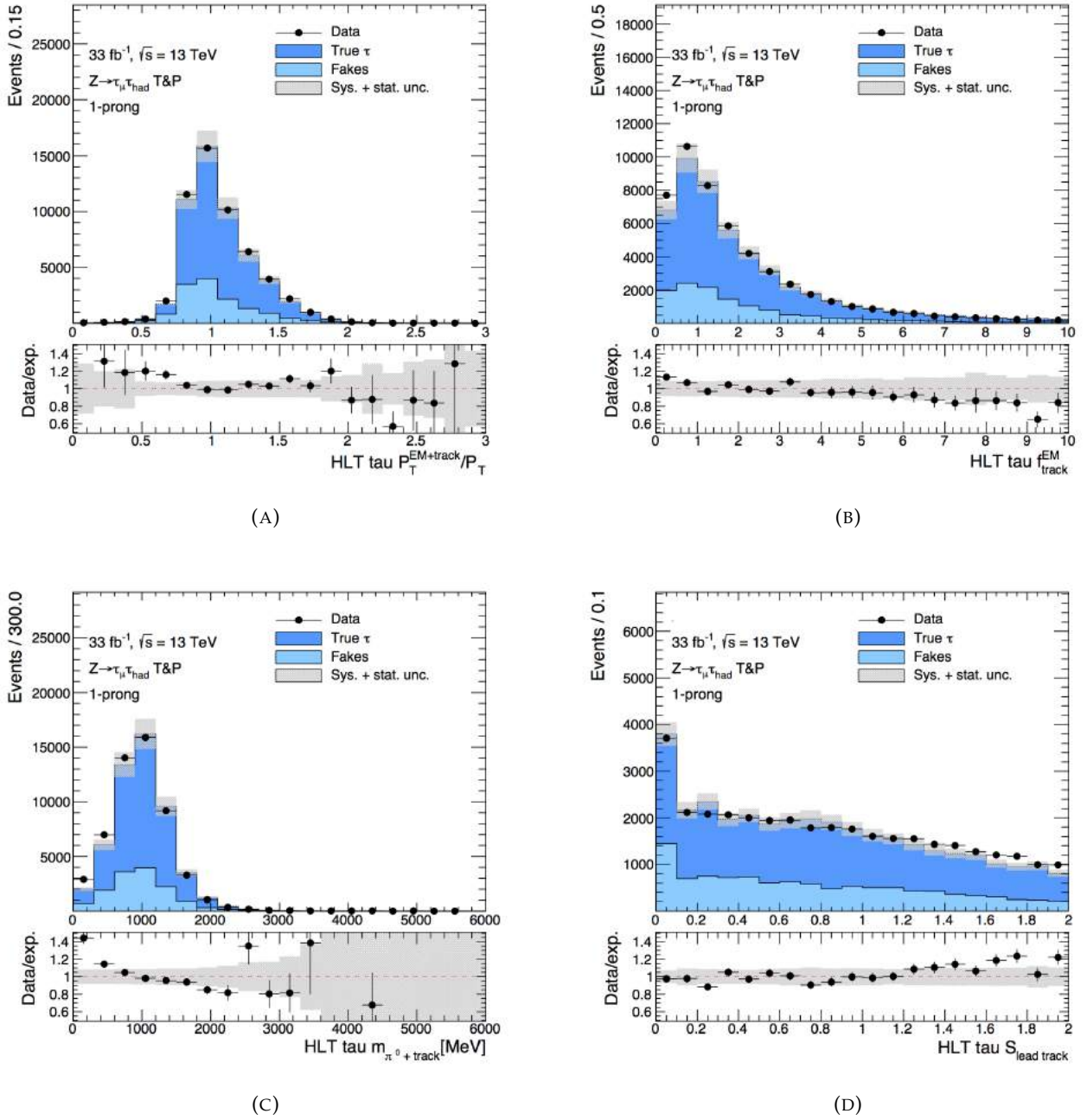


FIGURE 4.18: HLT BDT inputs for online $\tau_{\text{had,vis}}$ candidates matched to an offline 1-prong $\tau_{\text{had,vis}}$ probe in the selected $Z \rightarrow \tau\tau$ event candidates. Shown here are a) ratio of track-plus-EM-system to p_T ($p_T^{\text{EM+track}}/P_T$), b) ratio of EM energy to track momentum ($f_{\text{track}}^{\text{EM}}$), c) track-plus-EM-system mass ($m_{\pi^0+\text{track}}$), d) leading track IP significance ($|S_{\text{lead track}}|$). Systematic and statistical uncertainties are added in quadrature.

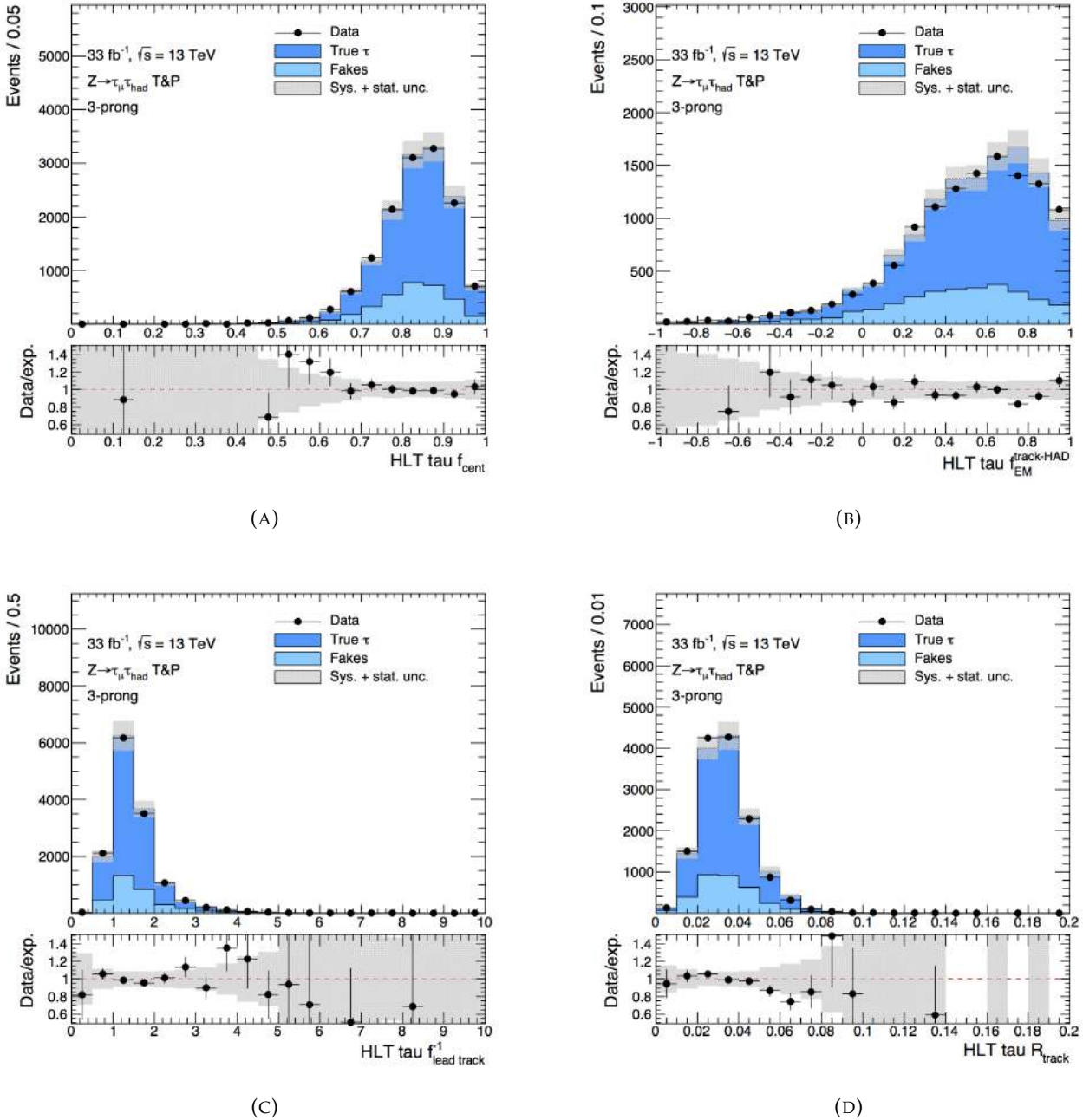


FIGURE 4.19: HLT BDT inputs for online $\tau_{\text{had,vis}}$ candidates matched to an offline 3-prong $\tau_{\text{had,vis}}$ probe in the selected $Z \rightarrow \tau\tau$ event candidates. Shown here are a) central energy fraction (f_{cent}), b) fraction of EM energy from charged pions ($f_{\text{EM}}^{\text{track-HAD}}$), c) leading track momentum fraction ($f_{\text{lead track}}^{-1}$), d) track radius (R_{track}). Systematic and statistical uncertainties are added in quadrature.

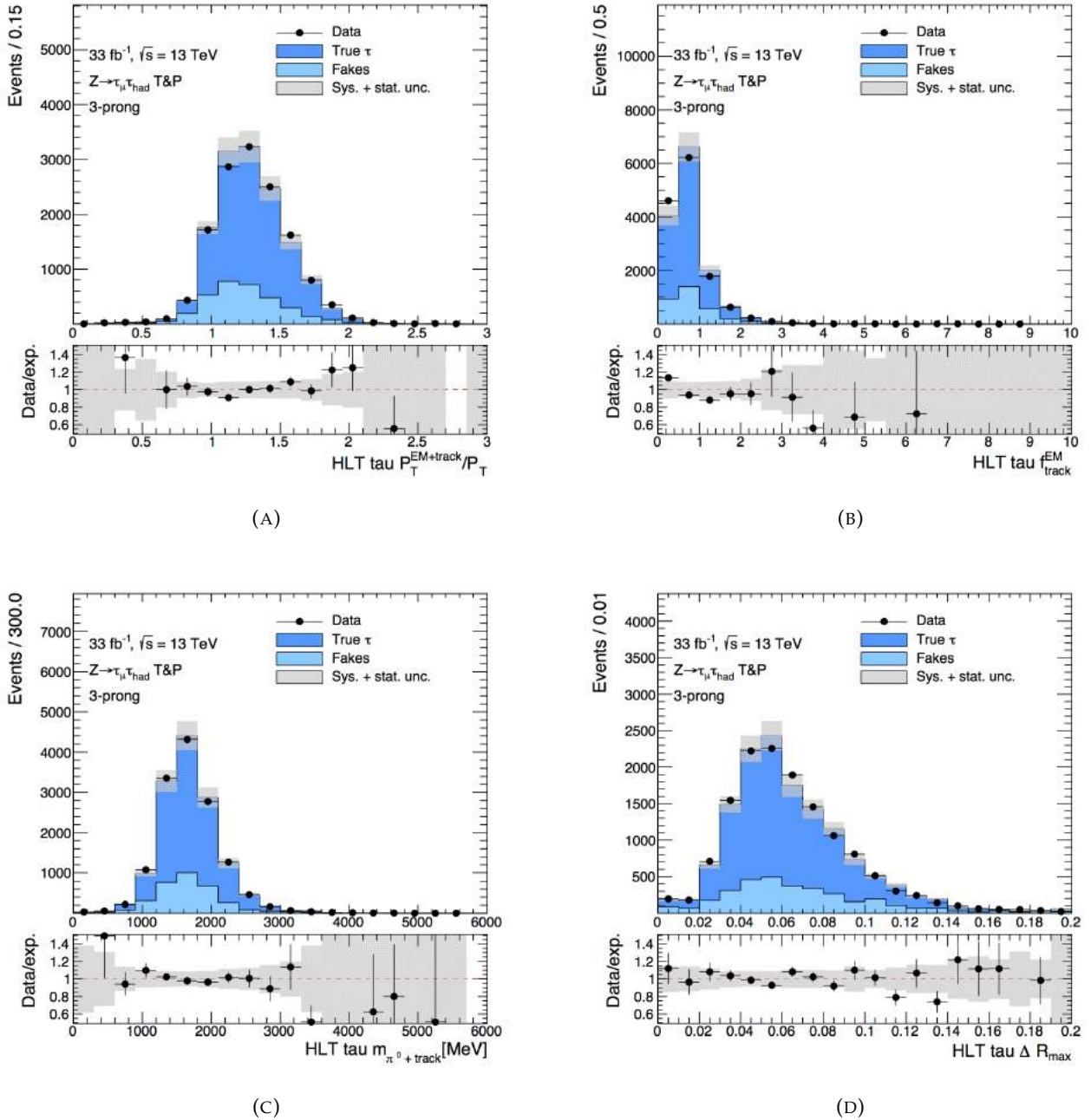


FIGURE 4.20: HLT BDT inputs for online $\tau_{\text{had,vis}}$ candidates matched to an offline 3-prong $\tau_{\text{had,vis}}$ probe in the selected $Z \rightarrow \tau\tau$ event candidates. Shown here are a) ratio of track-plus-EM-system to p_T ($p_T^{\text{EM+track}}/P_T$), b) ratio of EM energy to track momentum ($f_{\text{track}}^{\text{EM}}$), c) track-plus-EM-system mass ($m_{\pi^0+\text{track}}$), and d) maximum ΔR (ΔR_{Max}). Systematic and statistical uncertainties are added in quadrature.

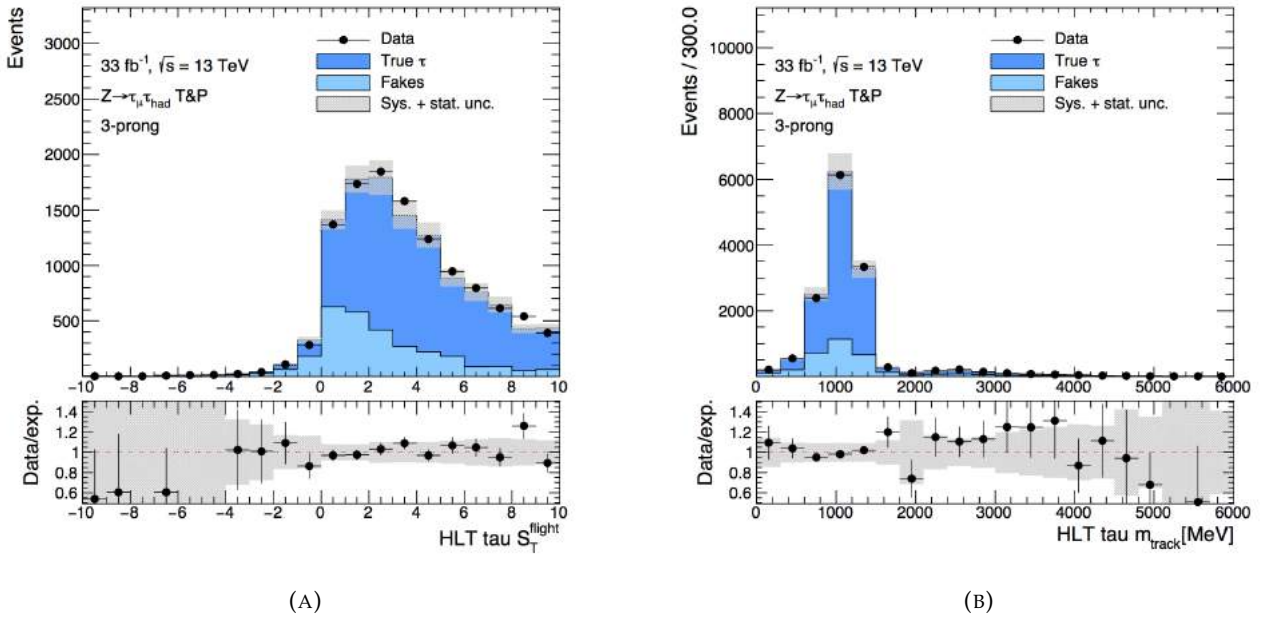


FIGURE 4.21: HLT BDT inputs for online $\tau_{\text{had,vis}}$ candidates matched to an offline 3-prong $\tau_{\text{had,vis}}$ probe in the selected $Z \rightarrow \tau\tau$ event candidates. Shown here are a) transverse flight path significance (S_T^{flight}), and b) track mass (m_{track}). Systematic and statistical uncertainties are added in quadrature.

4.7 Efficiency Measurement

The performance and efficiency of the tau trigger plays an important part in providing correction factors for Monte Carlo, referred to as *scale factors*. In the following section, the efficiency of the tau trigger for hadronically decaying tau leptons has been measured in the selected $Z \rightarrow \tau\tau$ events. The hadronic tau identification efficiency is expected to depend on both the p_T and η of the candidate, since the geometry of the detector changes with η and the online tau identification depends strongly on measurements of the p_T of the candidate. Due to this expected dependence, the efficiencies presented are parametrised in the offline $\tau_{\text{had,vis}}$ p_T and η , independently for 1-prong and 3-prong taus. A parametrisation in μ is also performed, in order to estimate the dependence of the trigger efficiency on the average number of interactions per bunch crossing.

The trigger efficiency is measured with respect to identified offline $\tau_{\text{had,vis}}$ candidates, defined as the fraction of the offline $\tau_{\text{had,vis}}$ probes that pass the tau trigger in question,

$$\varepsilon = \frac{n_{\text{pass}}}{n_{\text{total}}}. \quad (4.9)$$

This efficiency is measured in simulation for true hadronically decaying tau leptons, as well as in the selected data after the subtraction of the estimated backgrounds. These efficiencies in data and simulation are then compared in order to obtain the scale factors, defined in Equation 4.10 as the ratio between the two. The uncertainty on the subtracted background is considered as a systematic uncertainty on the efficiency measurement. Efficiencies and scale factors are measured independently for several tau triggers with differing p_T selection requirements, and are measured independently for candidates passing loose, medium, and tight identification requirements.

The efficiencies shown in this section are measured for five triggers of the form *HLT tauXX medium*, where XX is one of 25, 35, 80, 125, or 160, which require at the HLT a $\tau_{\text{had,vis}}$ candidate with $p_T > XX$ GeV passing the baseline track multiplicity and identification selection described in Section 3.4. The triggers with a lower minimum p_T at HLT (35 GeV to 80 GeV) require an isolated candidate at L1 with $E_T > 20$ GeV, with the exception of *HLT tau25 medium* which requires as isolated candidate at L1 with $E_T > 12$ GeV. The higher p_T triggers require an L1 candidate with $E_T > 60$ GeV (without isolation requirement). Two triggers with different L1 requirements, *HLT tau50 L1 tau12 medium* and *HLT tau80 L1 tau60 medium* are studied in addition.

Efficiencies for the *HLT tau25 medium* trigger are shown as a function of p_T in Figures 4.22, 4.23 and 4.24 for the three identification working points. The efficiencies are also shown as a function of η and μ in Figures 4.25 and 4.26 for candidates with $p_T > 30$ GeV fulfilling the medium identification working point. Small differences in the efficiencies in data and in simulation are expected due to slight differences in the calibration of the Tau Energy Scale (TES) and the HLT BDT training used in simulation versus that used in data. In particular, differences at low energies (in the *turn on curve* of the efficiency plot) are due to differences in the TES. Despite these differences, the efficiency of the tau trigger shows very good performance. For 1-prong $\tau_{\text{had,vis}}$ probes passing medium identification, *HLT tau25 medium* has a plateau efficiency of about 95% above $p_T > 40$ GeV, and for 3-prong $\tau_{\text{had,vis}}$ probes, the plateau efficiency is slightly lower at approximately 85% (Figure 4.23). At higher p_T , we see small differences for 3-prong taus, which could be due to the different TES track multiplicity parametrisations used online and offline.

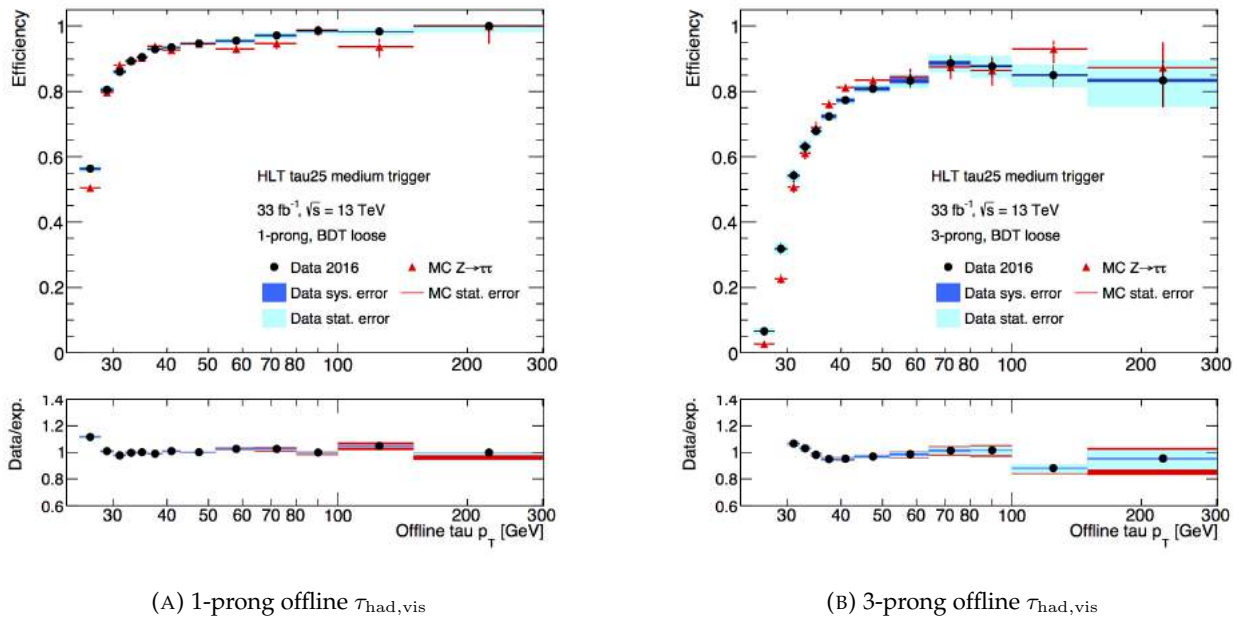


FIGURE 4.22: Efficiencies of the *HLT tau25 medium* trigger as a function of the p_T of the offline $\tau_{\text{had,vis}}$ probe selected in $Z \rightarrow \tau\tau$ events for (left) 1-prong and (right) 3-prong taus fulfilling the loose identification working point. The systematic uncertainty on the background subtraction is shown in dark blue, the total uncertainty on data is shown in light blue, and the combined uncertainty for data and MC is shown in red.

Figure 4.25 and 4.26 show the efficiencies as a function of the $\tau_{\text{had,vis}}$ pseudorapidity and of the average interactions per bunch-crossing to possess good modelling and stability. A gap in the efficiency parametrised in η is visible in the region $1.37 \leq \eta \leq 1.52$, due to the crack between the barrel and end-cap calorimeters. The efficiency is stable as the number of average interactions per bunch crossing increases, with only a small downward slope in higher μ for 3-prong taus. This is an important

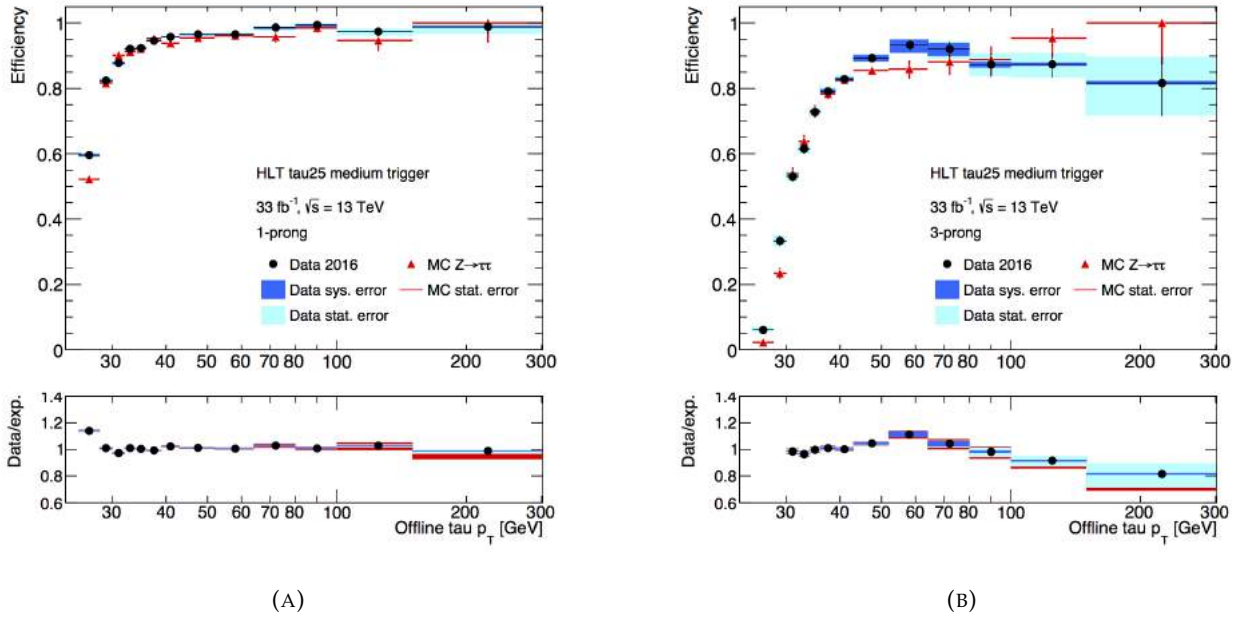


FIGURE 4.23: Efficiencies of the *HLT tau25 medium* trigger as a function of the p_T of the offline $\tau_{\text{had,vis}}$ probe selected in $Z \rightarrow \tau\tau$ events for (left) 1-prong and (right) 3-prong taus fulfilling the medium identification working point. The systematic uncertainty on the background subtraction is shown in dark blue, the total uncertainty on data is shown in light blue, and the combined uncertainty for data and MC is shown in red.

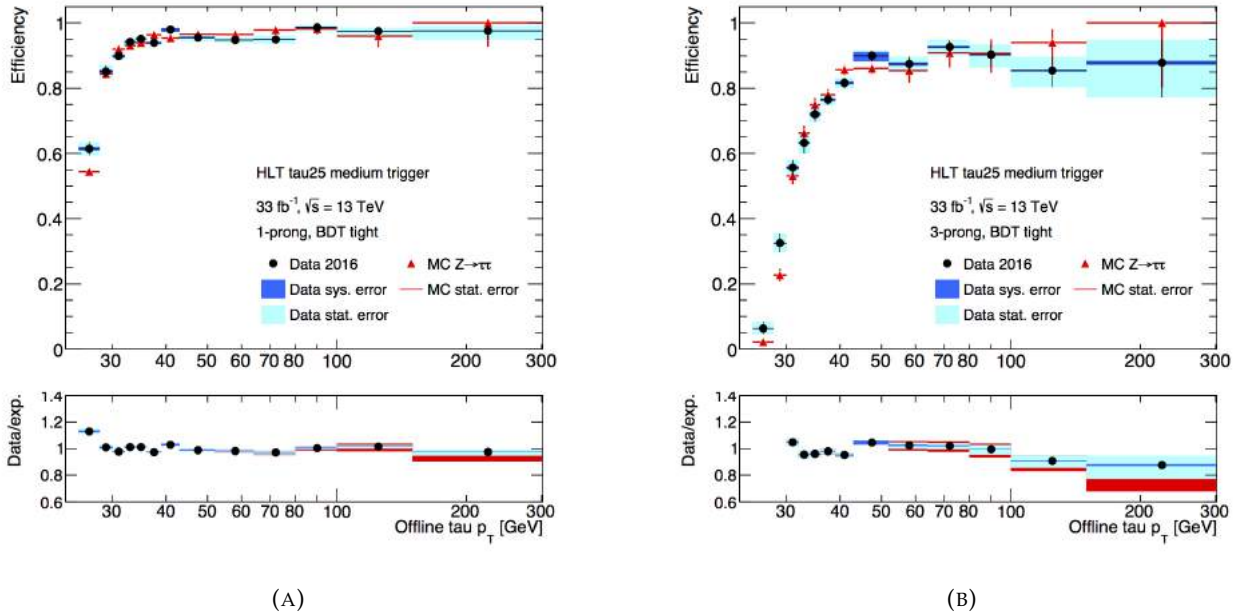


FIGURE 4.24: Efficiencies of the *HLT tau25 medium* trigger as a function of the p_T of the offline $\tau_{\text{had,vis}}$ probe selected in $Z \rightarrow \tau\tau$ events for (left) 1-prong and (right) 3-prong taus fulfilling the tight identification working point. The systematic uncertainty on the background subtraction is shown in dark blue, the total uncertainty on data is shown in light blue, and the combined uncertainty for data and MC is shown in red.

verification to make, as with higher luminosities and smaller bunch crossings the average interactions per bunch crossings will continue to increase, and it is imperative that the trigger efficiency remains stable as μ increases. In general, these results show good performance of the tau trigger. Efficiencies for the remaining individual triggers as a function of p_T are shown in Figures A.1 to A.18 in the Appendix.

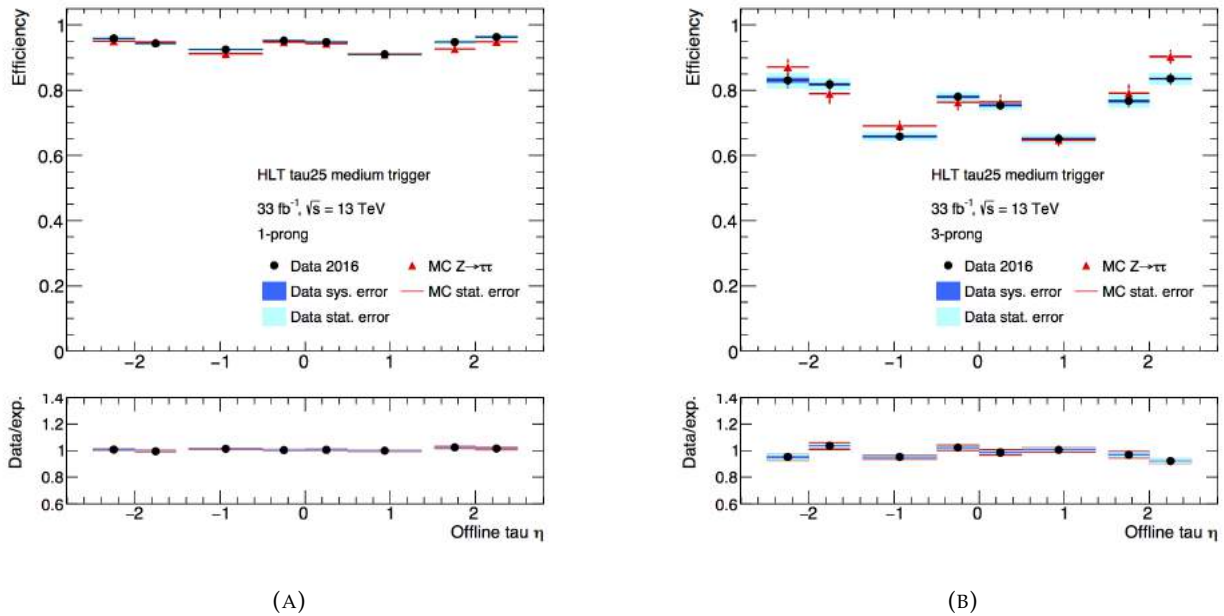


FIGURE 4.25: Efficiencies of the *HLT tau25 medium* trigger as a function of η for $\tau_{\text{had,vis}}$ 1-prong (left) and 3-prong (right) probes with $p_T > 30$ GeV selected in $Z \rightarrow \tau\tau$ events passing the medium identification requirement. The systematic uncertainty on the background subtraction is shown in dark blue, the total uncertainty on data is shown in light blue, and the combined uncertainty for data and MC is shown in red.

4.8 Scale Factors

Scale factors are measured as the ratio between the efficiencies in data and simulation, and are defined as

$$\text{SF}(p_T) = \frac{\varepsilon_{\text{data}}(p_T)}{\varepsilon_{\text{MC}}(p_T)}, \quad (4.10)$$

where ε is a given efficiency. Scale factors are important inputs to ATLAS physics analysis in correcting simulation to look more like data, and are shown as ‘data/exp’ in the ratio plots of Figures 4.22 to 4.26. In Figures 4.27 to 4.29, 2-dimensional maps are shown of the scale factors for the *HLT tau25 medium* trigger for the loose, medium, and tight working points, as a representative sample of the full set of scale factor maps which have been provided to the ATLAS trigger group, which includes scale factors for all triggers considered in this paper. These scale factor maps allow ATLAS analyses to correct any disagreements between data and simulation in the kinematic distributions of taus. They all vary close to unity, which indicates good simulation of the detector. Scale factors for the lowest p_T tau trigger are measured with an uncertainty of approximately 1%(sys) + 4%(stat) for 1-prong taus, and 2%(sys) and 10%(stat) for 3-prong taus.

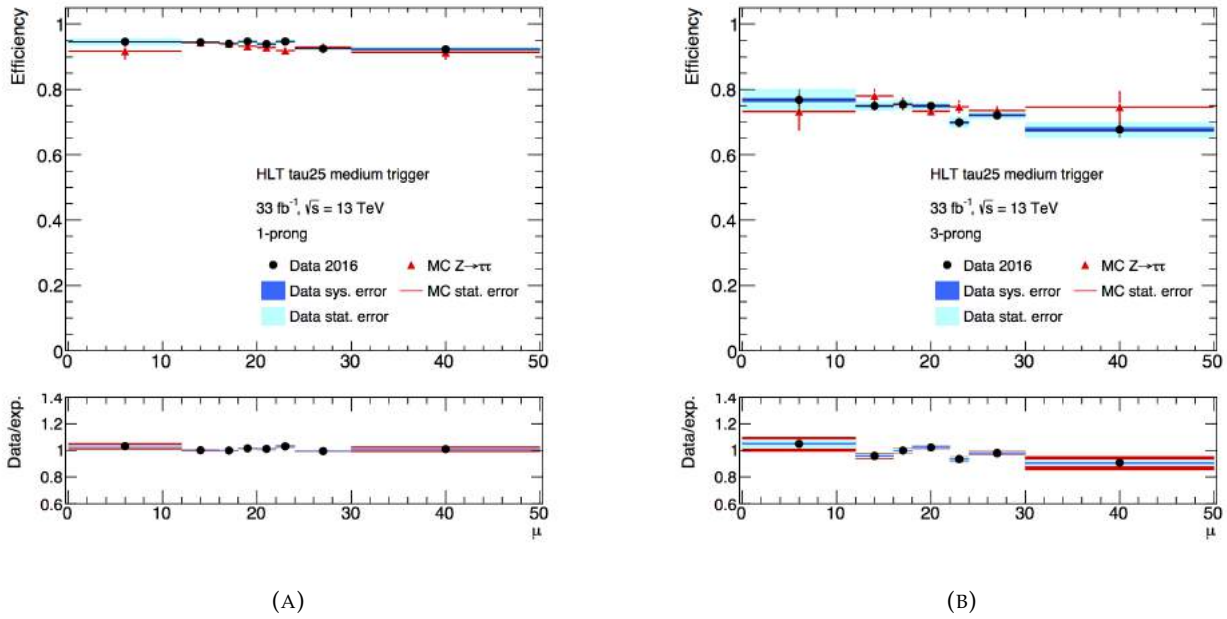


FIGURE 4.26: Efficiencies of the *HLT tau25 medium* trigger as a function of the average interactions per bunch-crossing for $\tau_{had,vis}$ 1-prong (left) and 3-prong (right) probes with $p_T > 30$ GeV selected in $Z \rightarrow \tau\tau$ events passing the medium identification requirement. The systematic uncertainty on the background subtraction is shown in dark blue, the total uncertainty on data is shown in light blue, and the combined uncertainty for data and MC is shown in red.

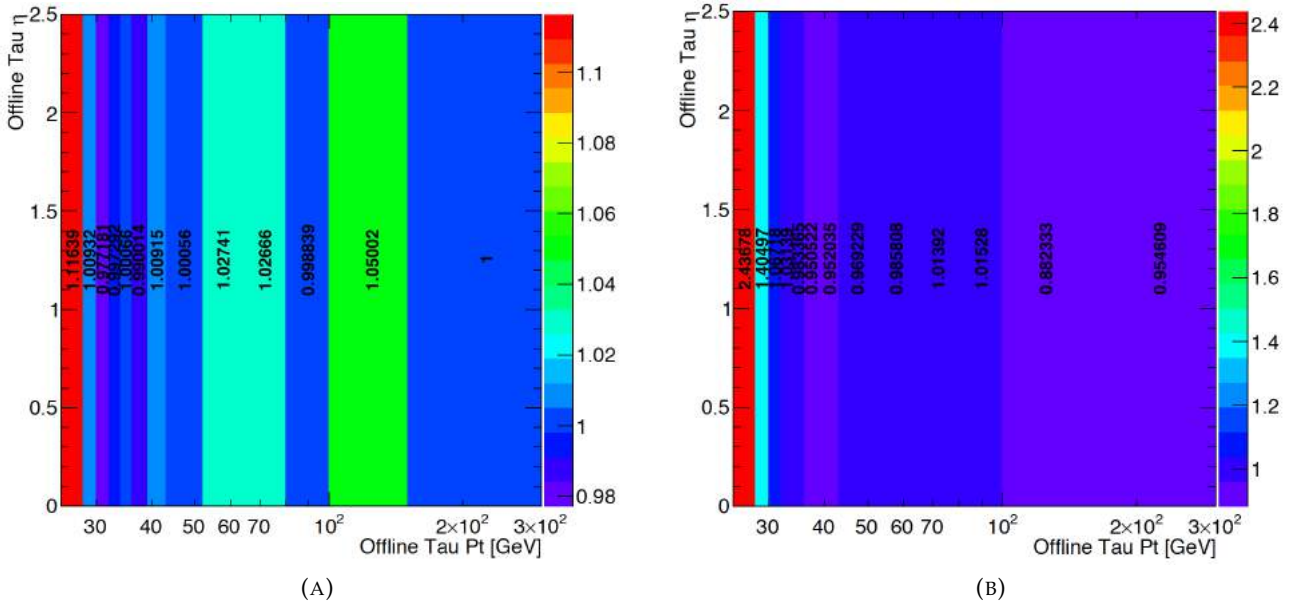


FIGURE 4.27: 2-dimensional maps of the scale factors for the *HLT tau25 medium* trigger measured for 1-prong (left) and 3-prong (right) taus passing the loose identification requirement.

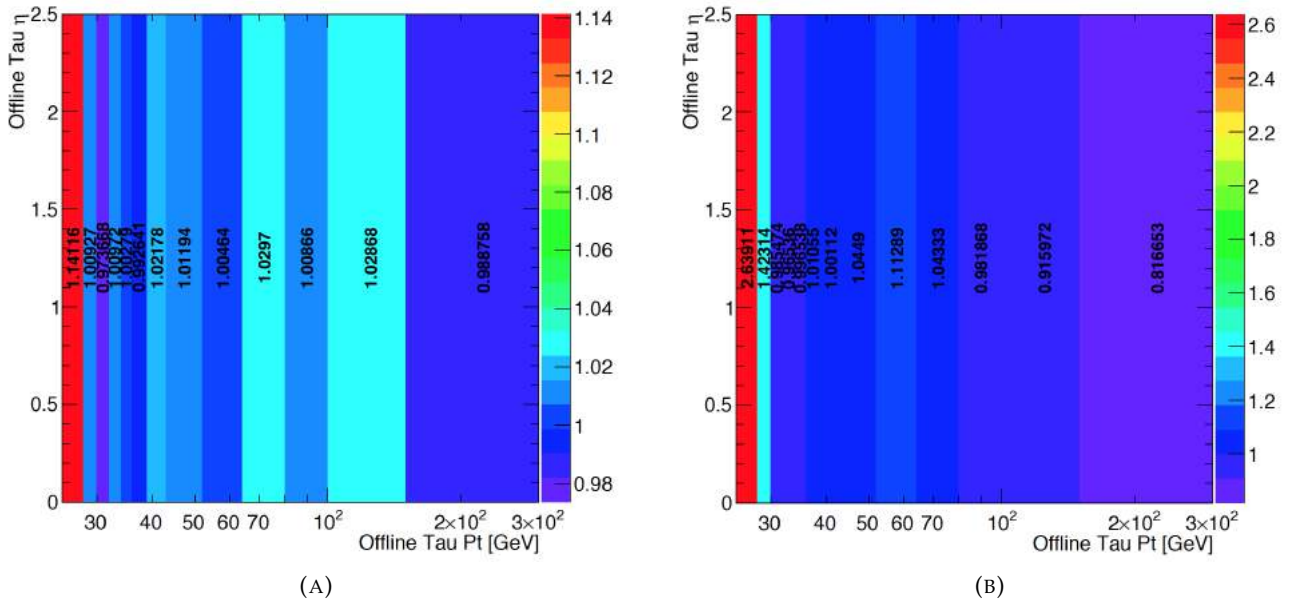


FIGURE 4.28: 2-dimensional maps of the scale factors for the *HLT tau25 medium* trigger measured for 1-prong (left) and 3-prong (right) taus passing the medium identification requirement.

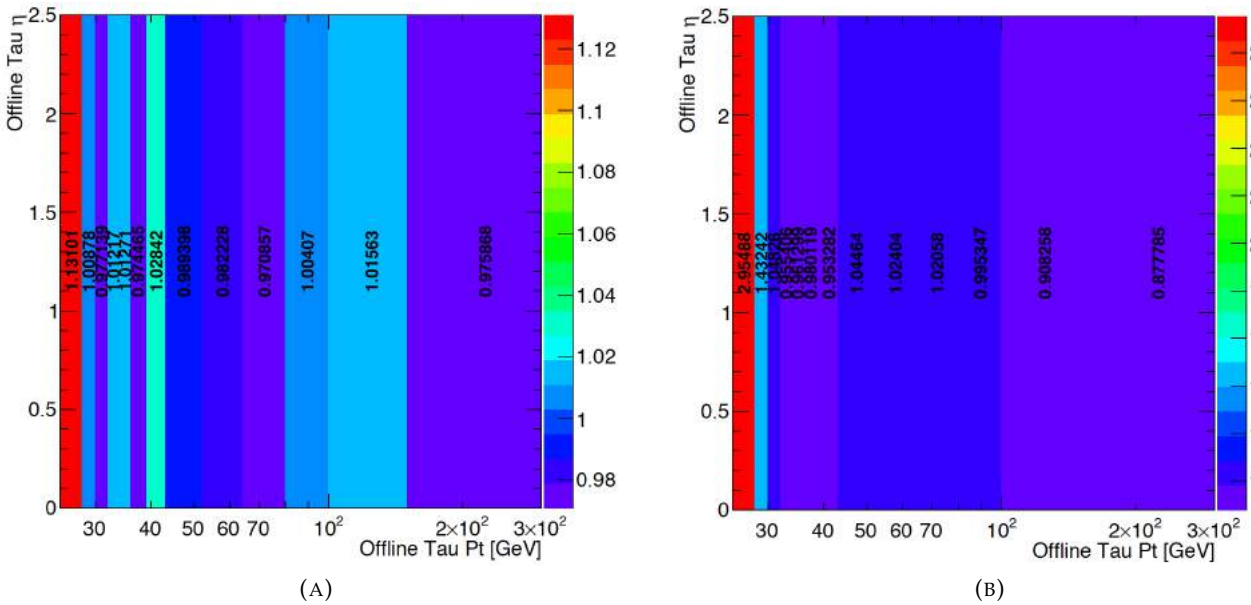


FIGURE 4.29: 2-dimensional maps of the scale factors for the *HLT tau25 medium* trigger measured for 1-prong (left) and 3-prong (right) taus passing the tight identification requirement.

4.9 HLT Selection Steps Efficiencies

To investigate the performance of each tau trigger selection described in Section 3.4, namely the Level 1 trigger selection, the HLT p_T selection, the HLT track multiplicity selection and the HLT BDT selection, efficiencies at each step are measured using dedicated performance tau triggers. Figure 4.30 shows the

efficiencies for these four steps as a function of the offline $\tau_{\text{had,vis}}$ probe p_T in $Z \rightarrow \tau\tau$ events.

The inefficiencies due to the L1 and HLT p_T resolutions are visible at the low p_T in the first two steps. The differences between data and simulation at the HLT p_T step are due to the different online TES calibrations used in data and simulation. In the HLT track selection step, the loss in efficiency for 3-prong candidates at high p_T comes primarily from the requirement on the number of reconstructed tracks at the fast tracking stage, as described in Section 3.4.1. At the HLT BDT step, a good stability as a function of $\tau_{\text{had,vis}}$ p_T is achieved. Differences between efficiencies in data and simulation are in part due to the different BDT training used. The efficiencies are then measured as a function of the offline $\tau_{\text{had,vis}}$ probe pseudorapidity and as a function of μ in Figures 4.31 and 4.32, respectively. Good agreement between data and simulation is observed overall.

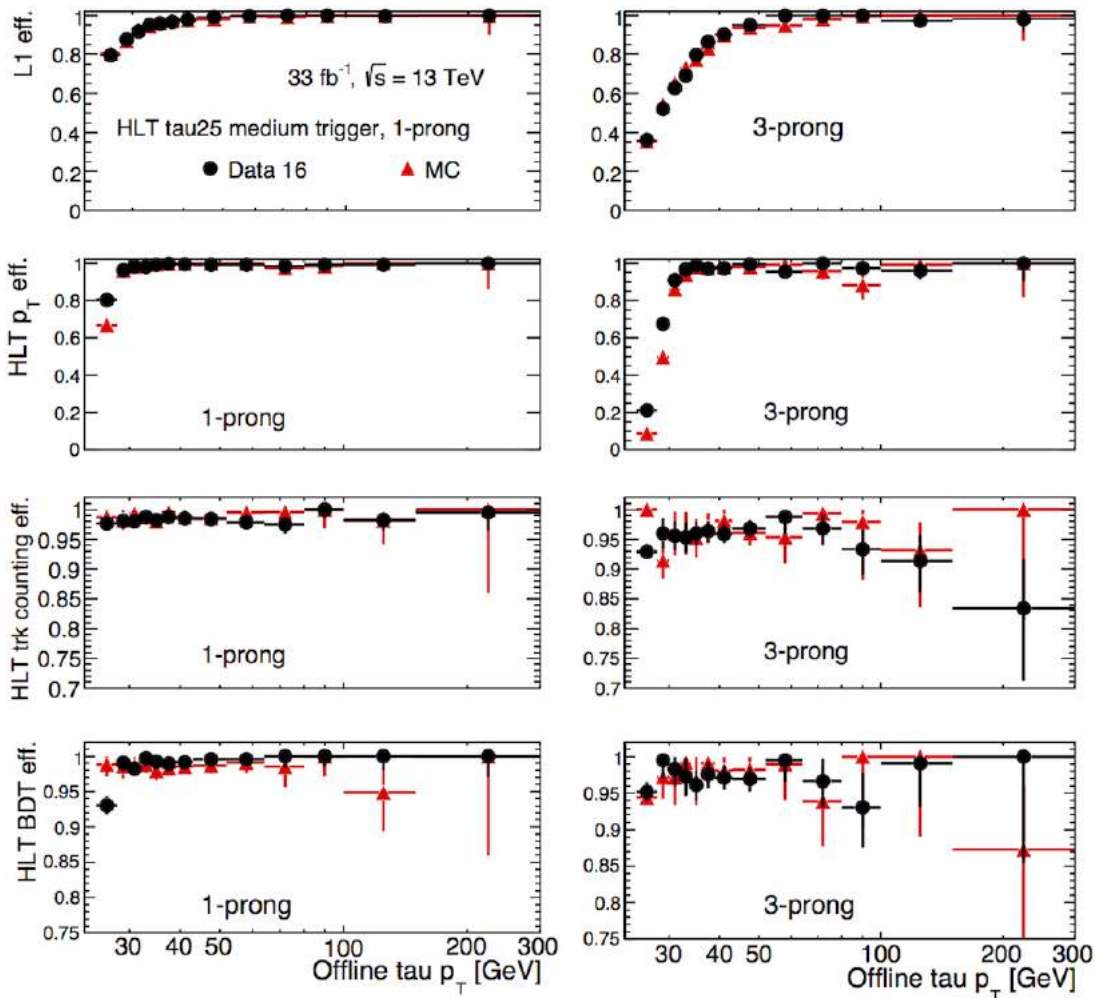


FIGURE 4.30: Selection efficiencies for each selection step of the *HLT tau25 medium* trigger for 1-prong (left) and 3-prong (right) τ_{vis} candidates in $Z \rightarrow \tau\tau$ events, parametrised in offline $\tau_{\text{had,vis}}$ p_T . The efficiencies of the L1, HLT p_T , HLT track multiplicity and HLT BDT selections are shown in descending order. Statistical and systematic uncertainties on data are combined quadratically.

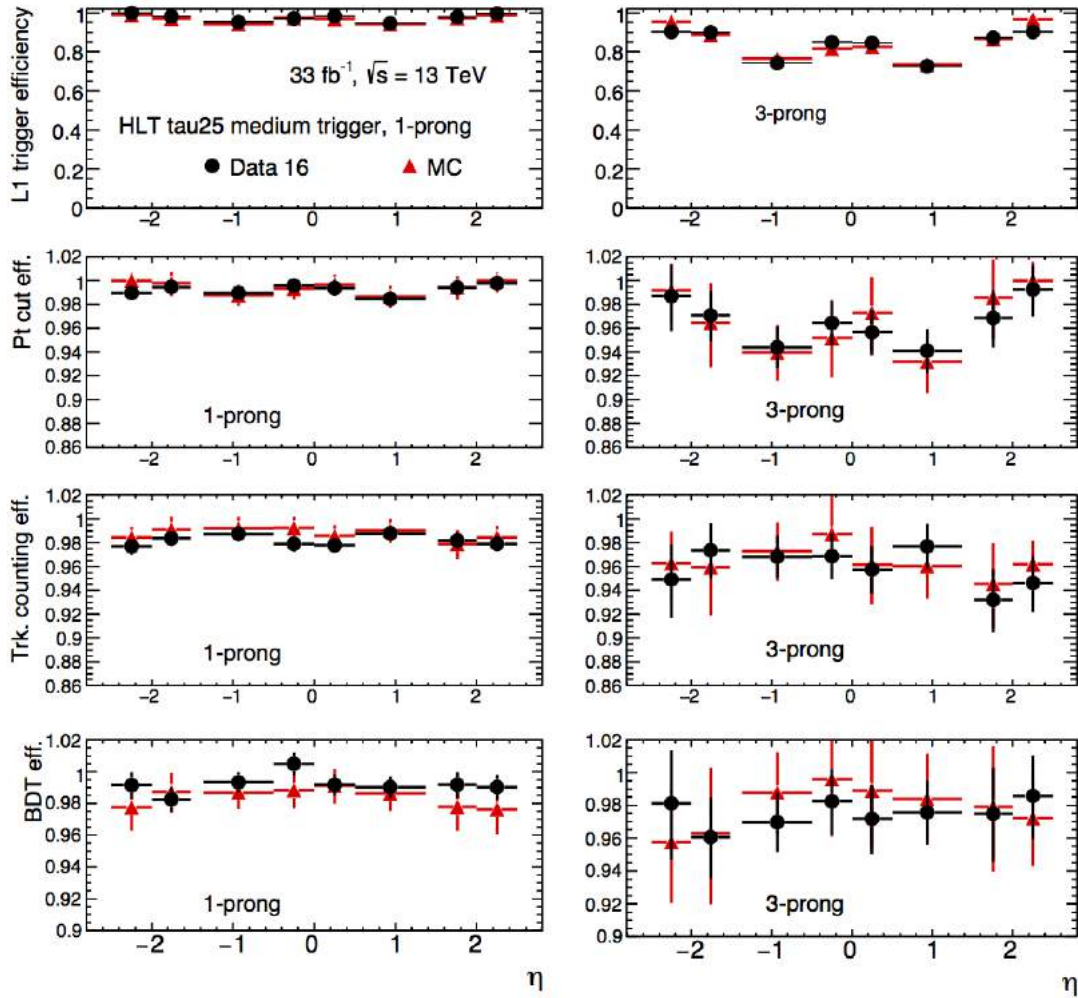


FIGURE 4.31: Selection efficiencies for each selection step of the *HLT tau25 medium* trigger for 1-prong (left) and 3-prong (right) τ_{vis} candidates in $Z \rightarrow \tau\tau$ events, parametrised in offline $\tau_{\text{had,vis}}$ η . The efficiencies of the L1, HLT p_T , HLT track multiplicity and HLT BDT selections are shown in descending order. Statistical and systematic uncertainties on data are combined quadratically.

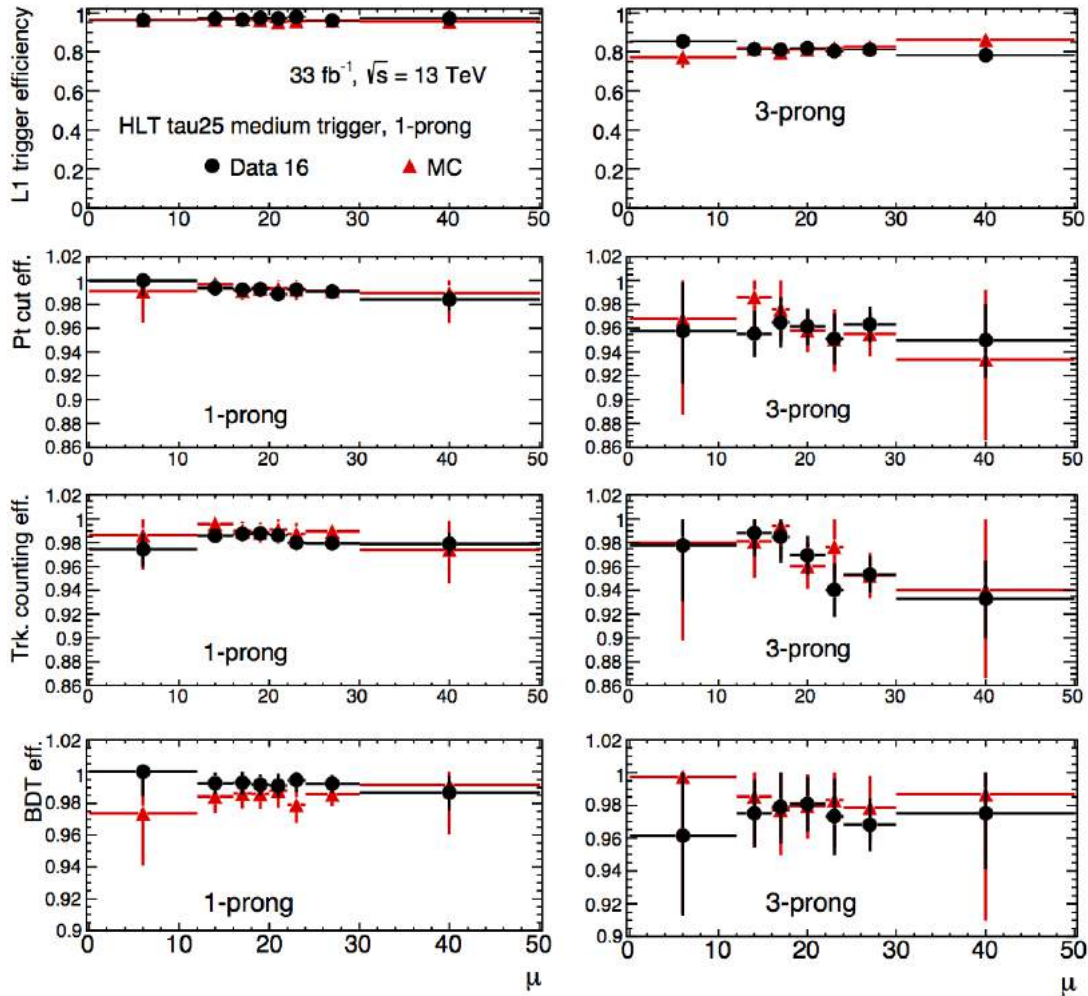


FIGURE 4.32: Selection efficiencies for each selection step of the $HLT\ tau25\ medium$ trigger for 1-prong (left) and 3-prong (right) τ_{vis} candidates in $Z \rightarrow \tau\tau$ events, parametrised in μ . The efficiencies of the L1, HLT p_T , HLT track multiplicity and HLT BDT selections are shown in descending order. Statistical and systematic uncertainties on data are combined quadratically.

Chapter 5

Conclusion

Our knowledge of the laws of physics of the sub-nuclear world is largely due to our analysis of high-energy collisions of elementary particles. As particle physicists continue to analyse higher and higher energy regimes, so the requirements on the detectors used for these analyses become more demanding, and their performance must be carefully monitored. Due to the complex nature of tau decays and the high luminosity and centre of mass energy achieved during 2016, validations of the tau trigger are crucial.

Using $Z \rightarrow \tau\tau$ events selected in the 33.3 fb^{-1} of 2016 pp collision data at $\sqrt{s} = 13 \text{ TeV}$ and a new $W(\rightarrow \mu\nu) + \text{jets}$ background estimation method, a measurement of the tau trigger efficiency and the corresponding scale factors have been performed for a selection of High Level Triggers at ATLAS. Good performance is shown by the ATLAS tau trigger over the full 2016 dataset, especially given the exceptional performance of the LHC, which resulted in a steep rise in the number of pile-up interactions. Plateau efficiencies of about 95% (85%) are achieved for 1-prong (3-prong) offline $\tau_{\text{had,vis}}$ candidates for the lowest p_T tau trigger, showing good efficiency for p_T bins above the turn on curve. The corresponding scale factors for each trigger efficiency are measured with uncertainties up to 4% (10%) for 1-prong (3-prong) $\tau_{\text{had,vis}}$ candidates. These scale factors are all close to unity, which indicates good understanding of the detector in simulation. The scale factors for the tau trigger efficiency in simulation have been provided to and approved by the Tau Trigger Group at ATLAS, to be used in future analyses.

In addition, the ATLAS Run 2 tau trigger reconstruction and identification algorithms have been presented, together with a measurement of the performance of the online $\tau_{\text{had,vis}}$ reconstruction, which has showed good performance. These algorithms have contributed significantly to fulfilling a variety of physics searches and measurements concerning hadronically decaying tau leptons, and will continue to do so in the future. The efficiency at each selection step of the HLT has been investigated, showing good stability.

The identification and reconstruction of hadronically decaying tau leptons is a difficult task, but one that the tau trigger system employed at the ATLAS detector is handling well, allowing particle physicists to continue to probe higher energy regimes in searches for new physics beyond the Standard Model.

Appendix A

Appendix

The following section presents efficiency plots of the higher p_T tau triggers, parametrised in p_T .

A.1 Higher p_T Triggers

In the following measurements the minimum p_T of the hadronic tau candidate was required to be 5 GeV greater than the p_T threshold of the trigger. The binning was not made finer for higher p_T triggers, due to insufficient amounts of data. Efficiencies are calculated independently for candidates satisfying the loose, medium and tight working points.

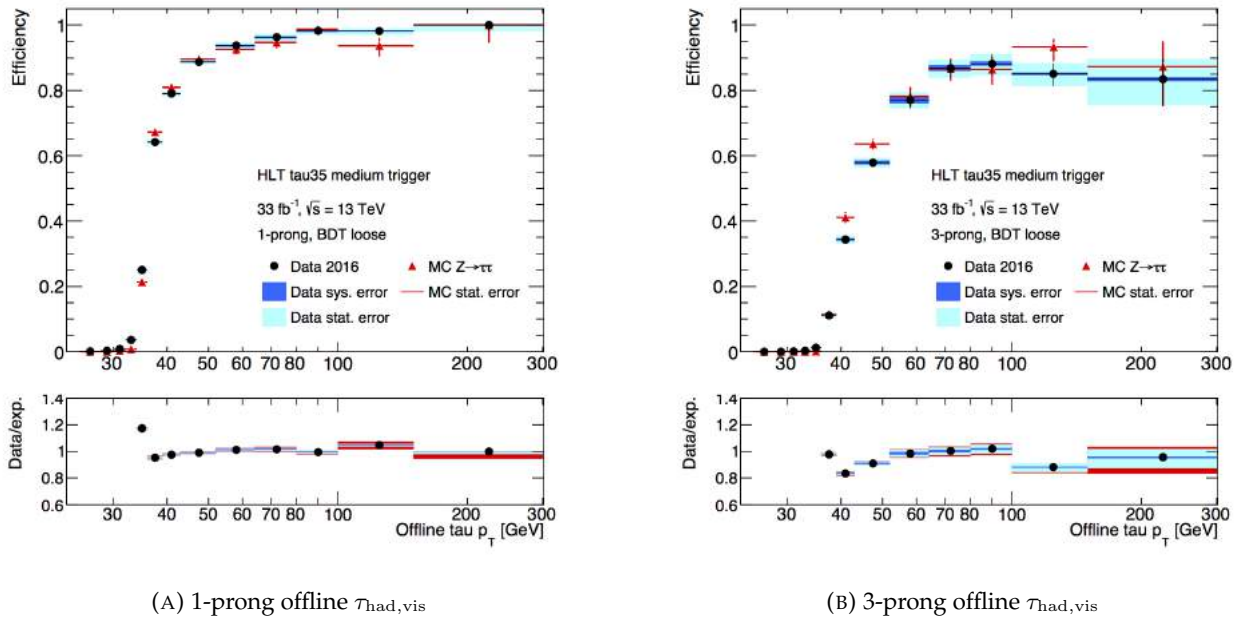


FIGURE A.1: Efficiencies of the *HLT tau35 medium* trigger as a function of the p_T of the offline $\tau_{\text{had,vis}}$ probe selected in $Z \rightarrow \tau\tau$ events for (left) 1-prong and (right) 3-prong taus fulfilling the loose identification working point. The systematic uncertainty on the background subtraction is shown in dark blue, the total uncertainty on data is shown in light blue, and the combined uncertainty for data and MC is shown in red.

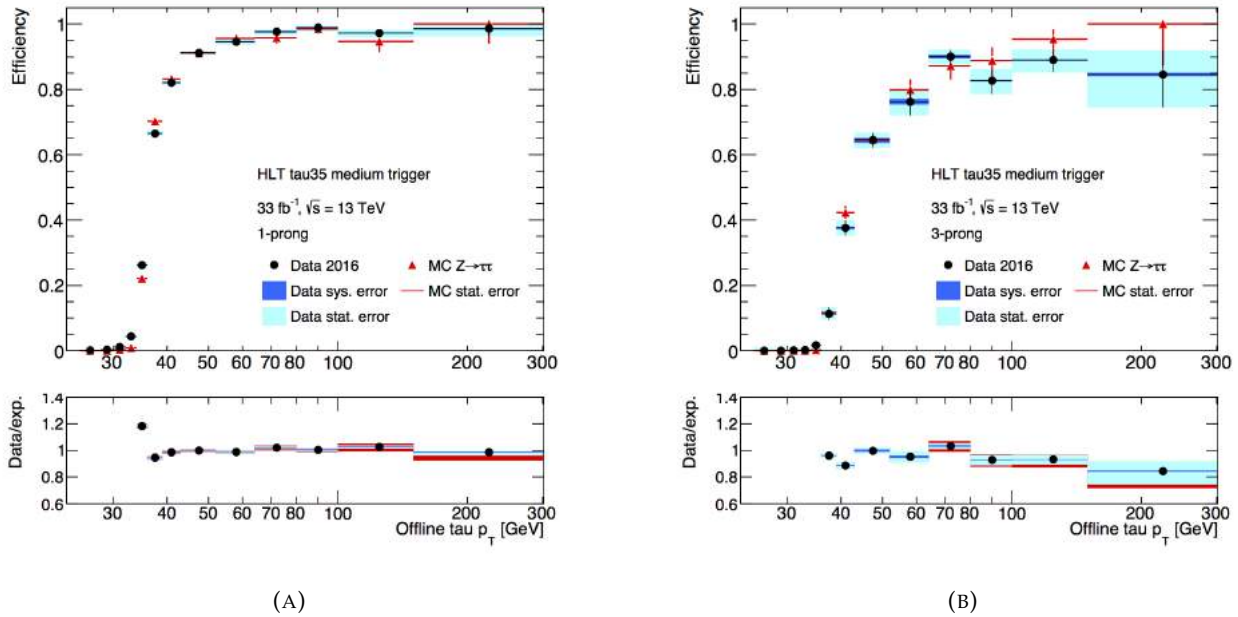


FIGURE A.2: Efficiencies of the *HLT tau35 medium* trigger as a function of the p_T of the offline $\tau_{\text{had,vis}}$ probe selected in $Z \rightarrow \tau\tau$ events for (left) 1-prong and (right) 3-prong taus fulfilling the medium identification working point. The systematic uncertainty on the background subtraction is shown in dark blue, the total uncertainty on data is shown in light blue, and the combined uncertainty for data and MC is shown in red.

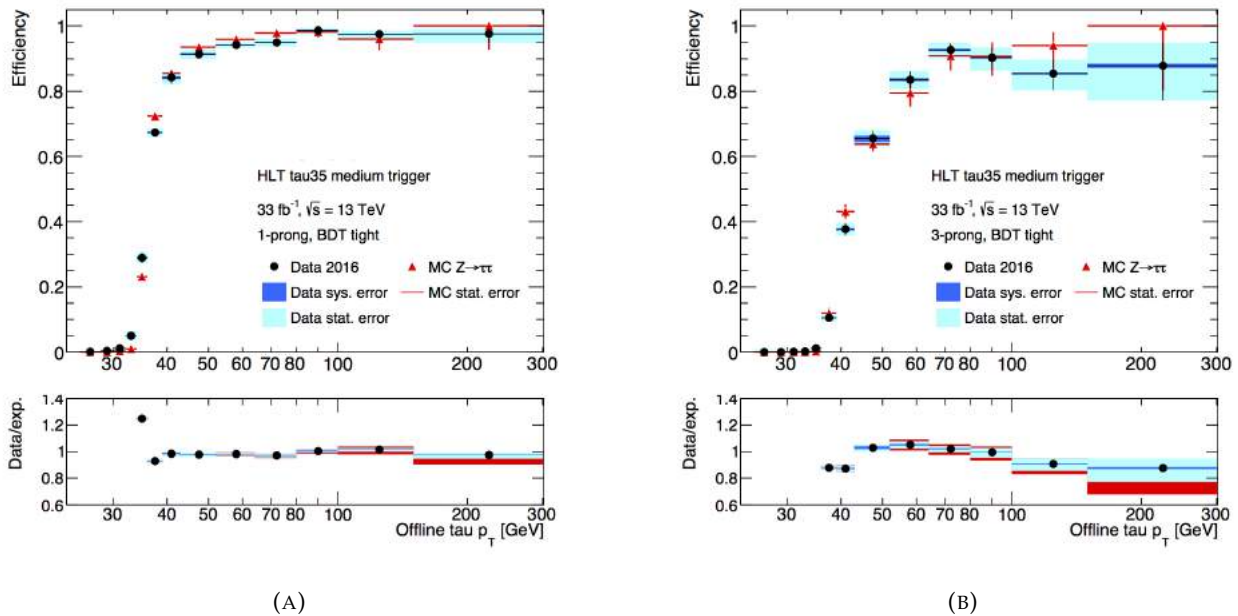


FIGURE A.3: Efficiencies of the *HLT tau35 medium* trigger as a function of the p_T of the offline $\tau_{\text{had,vis}}$ probe selected in $Z \rightarrow \tau\tau$ events for (left) 1-prong and (right) 3-prong taus fulfilling the tight identification working point. The systematic uncertainty on the background subtraction is shown in dark blue, the total uncertainty on data is shown in light blue, and the combined uncertainty for data and MC is shown in red.

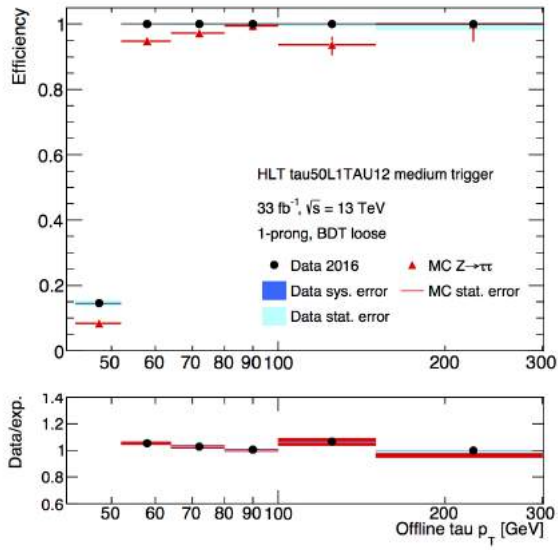
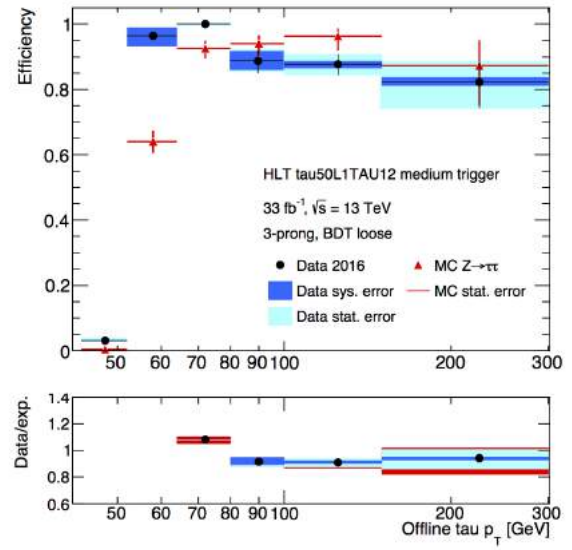
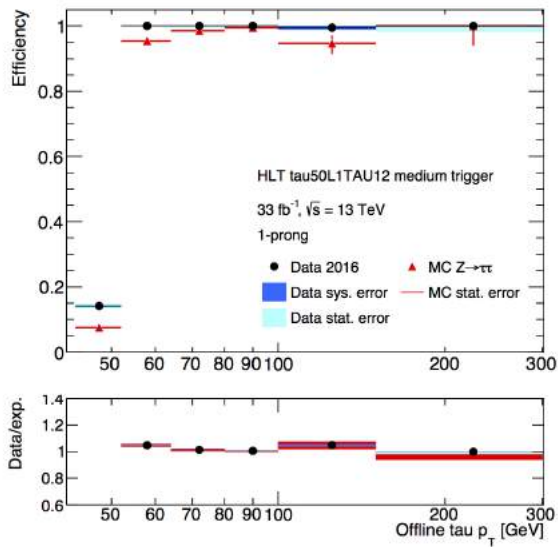
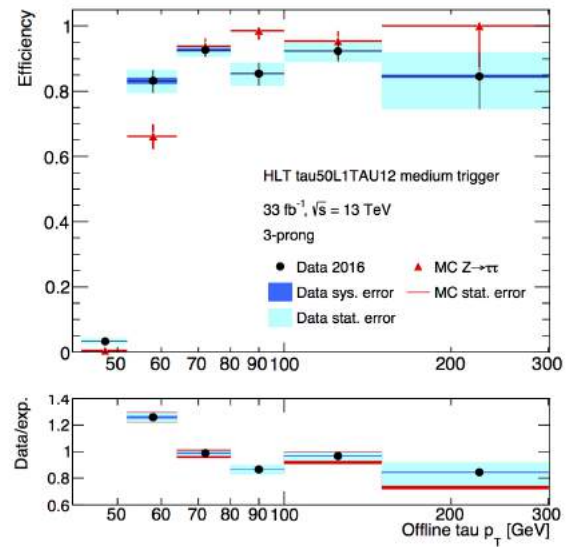
(A) 1-prong offline $\tau_{\text{had,vis}}$ (B) 3-prong offline $\tau_{\text{had,vis}}$

FIGURE A.4: Efficiencies of the *HLT tau50 L1tau12 medium* trigger as a function of the p_T of the offline $\tau_{\text{had,vis}}$ probe selected in $Z \rightarrow \tau\tau$ events for (left) 1-prong and (right) 3-prong taus fulfilling the loose identification working point. The systematic uncertainty on the background subtraction is shown in dark blue, the total uncertainty on data is shown in light blue, and the combined uncertainty for data and MC is shown in red.



(A)



(B)

FIGURE A.5: Efficiencies of the *HLT tau50 L1tau12 medium* trigger as a function of the p_T of the offline $\tau_{\text{had,vis}}$ probe selected in $Z \rightarrow \tau\tau$ events for (left) 1-prong and (right) 3-prong taus fulfilling the medium identification working point. The systematic uncertainty on the background subtraction is shown in dark blue, the total uncertainty on data is shown in light blue, and the combined uncertainty for data and MC is shown in red.

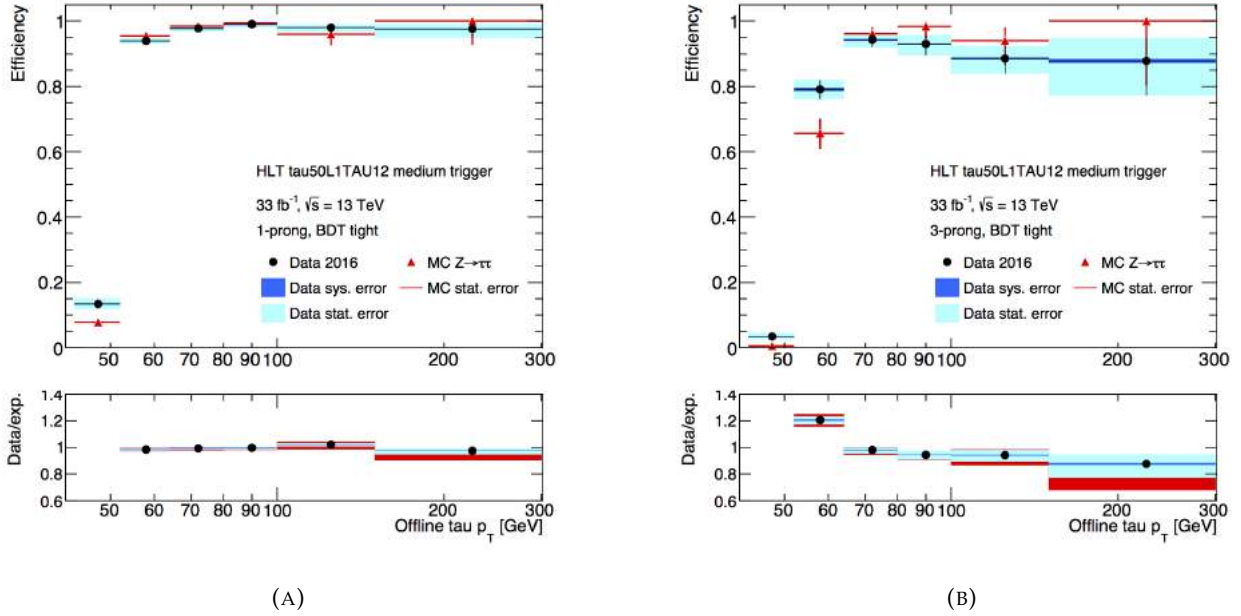


FIGURE A.6: Efficiencies of the *HLT tau50 L1tau12 medium* trigger as a function of the p_T of the offline $\tau_{\text{had,vis}}$ probe selected in $Z \rightarrow \tau\tau$ events for (left) 1-prong and (right) 3-prong taus fulfilling the tight identification working point. The systematic uncertainty on the background subtraction is shown in dark blue, the total uncertainty on data is shown in light blue, and the combined uncertainty for data and MC is shown in red.

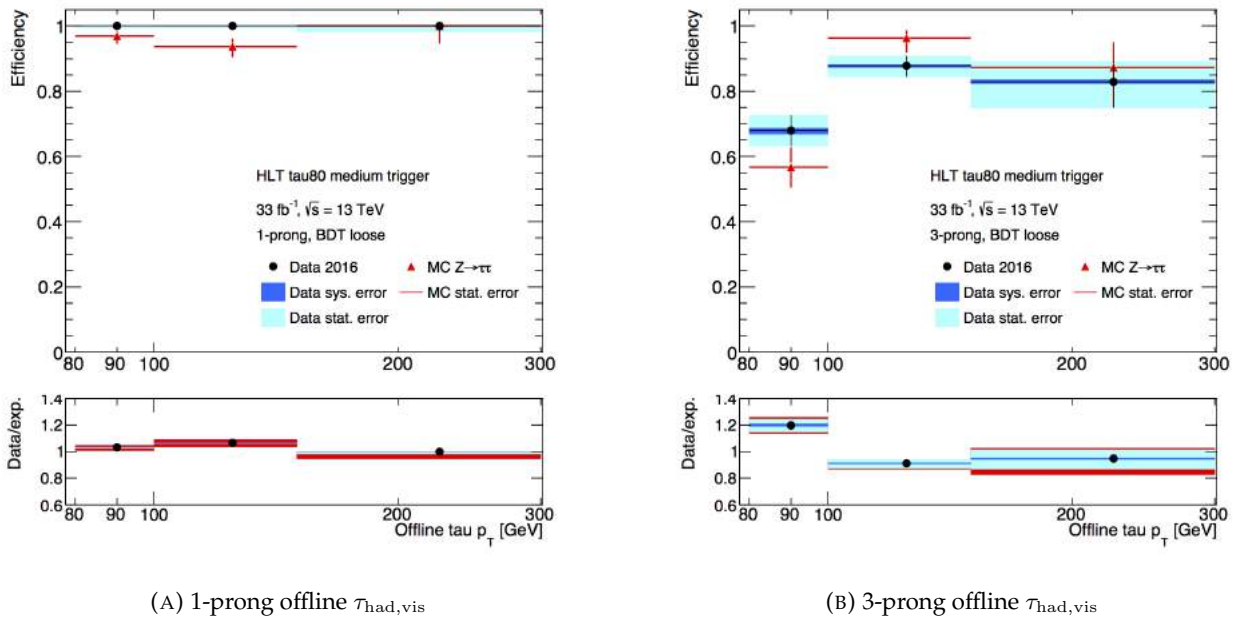


FIGURE A.7: Efficiencies of the *HLT tau80 medium* trigger as a function of the p_T of the offline $\tau_{\text{had,vis}}$ probe selected in $Z \rightarrow \tau\tau$ events for (left) 1-prong and (right) 3-prong taus fulfilling the loose identification working point. The systematic uncertainty on the background subtraction is shown in dark blue, the total uncertainty on data is shown in light blue, and the combined uncertainty for data and MC is shown in red.

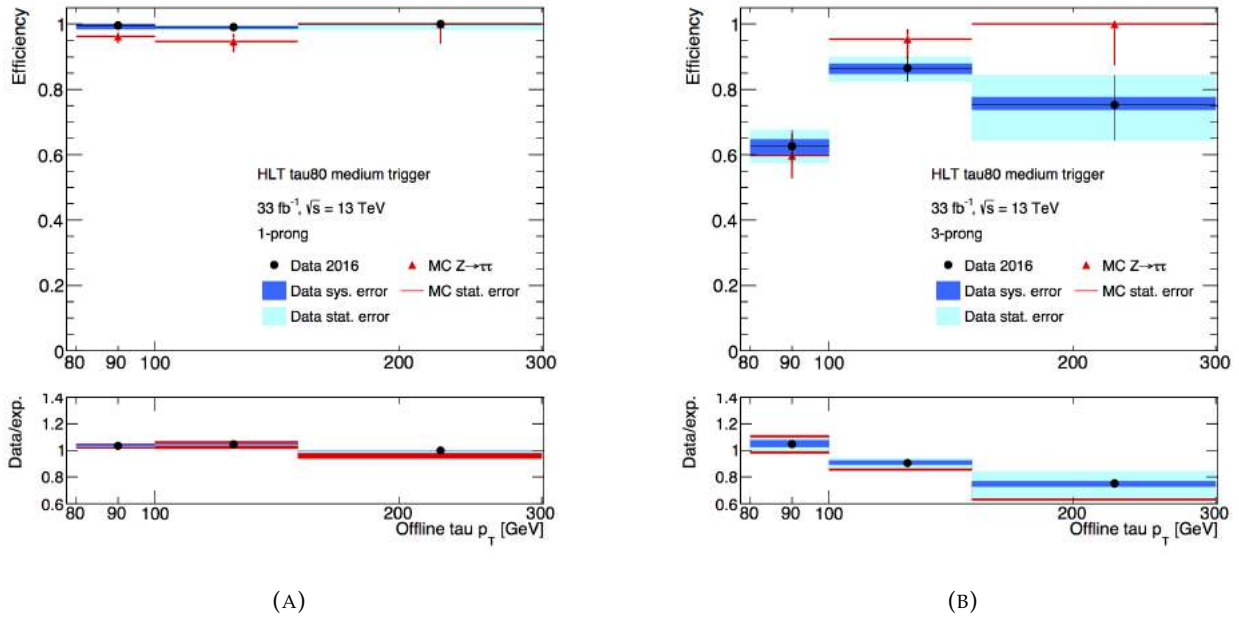


FIGURE A.8: Efficiencies of the *HLT tau80 medium* trigger as a function of the p_T of the offline $\tau_{\text{had,vis}}$ probe selected in $Z \rightarrow \tau\tau$ events for (left) 1-prong and (right) 3-prong taus fulfilling the medium identification working point. The systematic uncertainty on the background subtraction is shown in dark blue, the total uncertainty on data is shown in light blue, and the combined uncertainty for data and MC is shown in red.

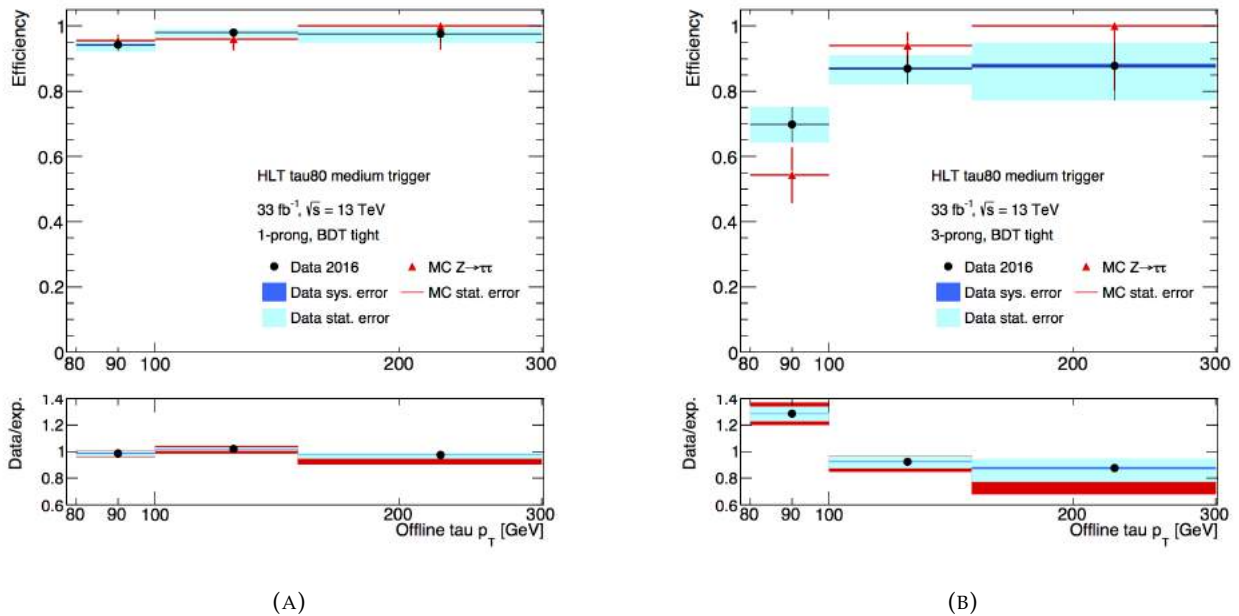


FIGURE A.9: Efficiencies of the *HLT tau80 medium* trigger as a function of the p_T of the offline $\tau_{\text{had,vis}}$ probe selected in $Z \rightarrow \tau\tau$ events for (left) 1-prong and (right) 3-prong taus fulfilling the tight identification working point. The systematic uncertainty on the background subtraction is shown in dark blue, the total uncertainty on data is shown in light blue, and the combined uncertainty for data and MC is shown in red.

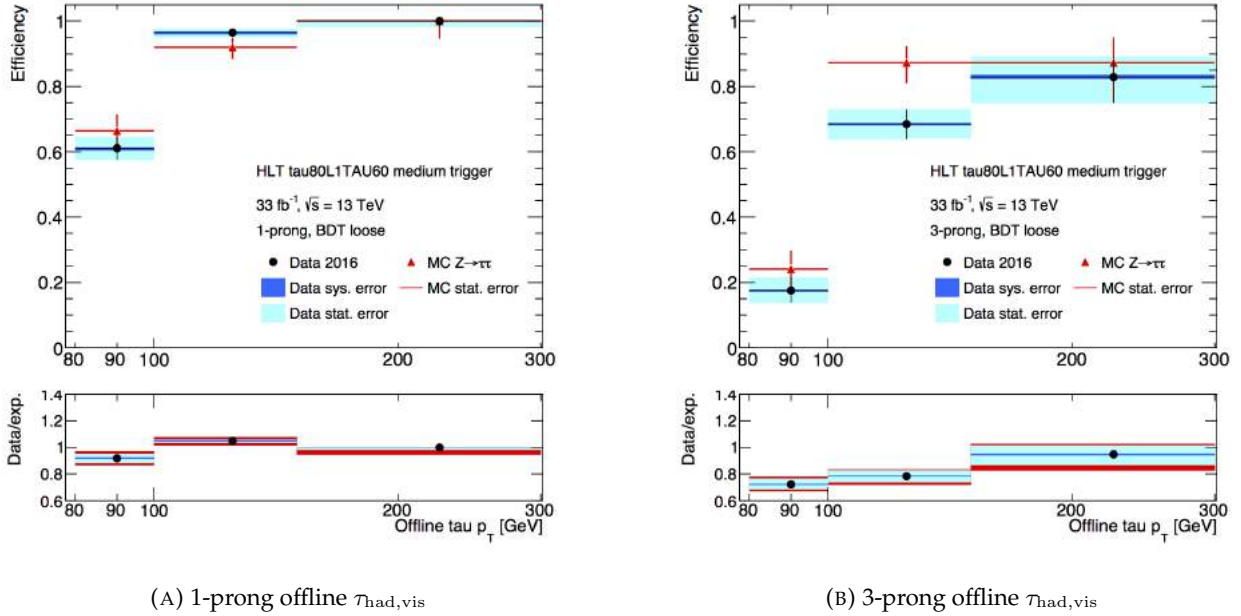


FIGURE A.10: Efficiencies of the *HLT tau80 L1tau60 medium* trigger as a function of the p_T of the offline $\tau_{\text{had,vis}}$ probe selected in $Z \rightarrow \tau\tau$ events for (left) 1-prong and (right) 3-prong taus fulfilling the loose identification working point. The systematic uncertainty on the background subtraction is shown in dark blue, the total uncertainty on data is shown in light blue, and the combined uncertainty for data and MC is shown in red.

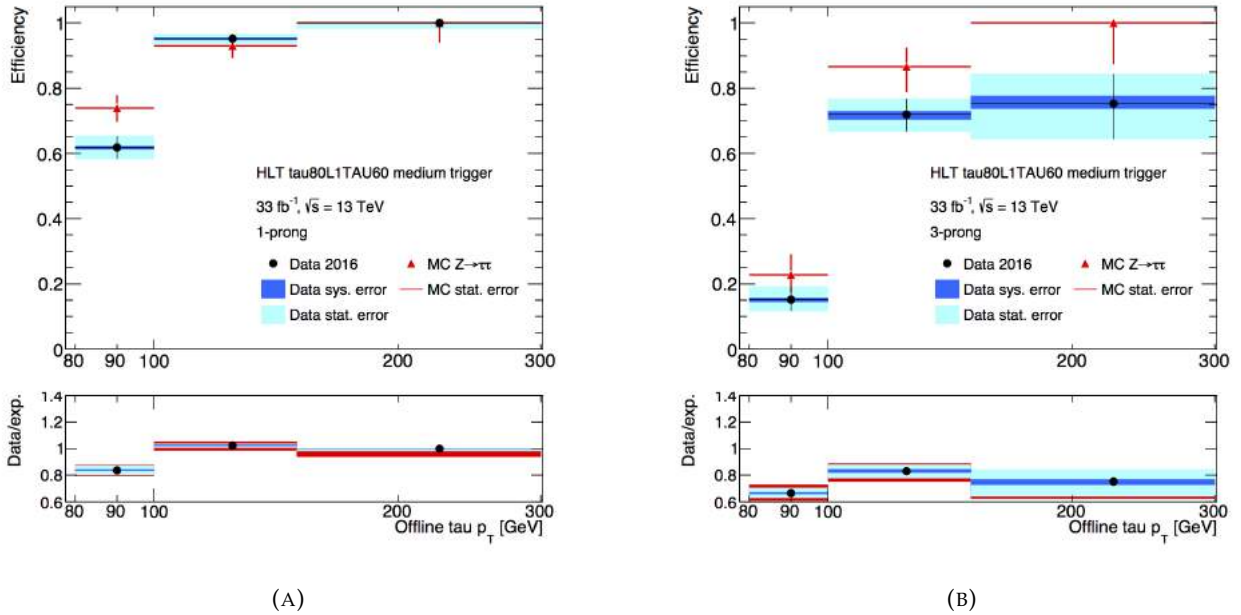


FIGURE A.11: Efficiencies of the *HLT tau80 L1tau60 medium* trigger as a function of the p_T of the offline $\tau_{\text{had,vis}}$ probe selected in $Z \rightarrow \tau\tau$ events for (left) 1-prong and (right) 3-prong taus fulfilling the medium identification working point. The systematic uncertainty on the background subtraction is shown in dark blue, the total uncertainty on data is shown in light blue, and the combined uncertainty for data and MC is shown in red.

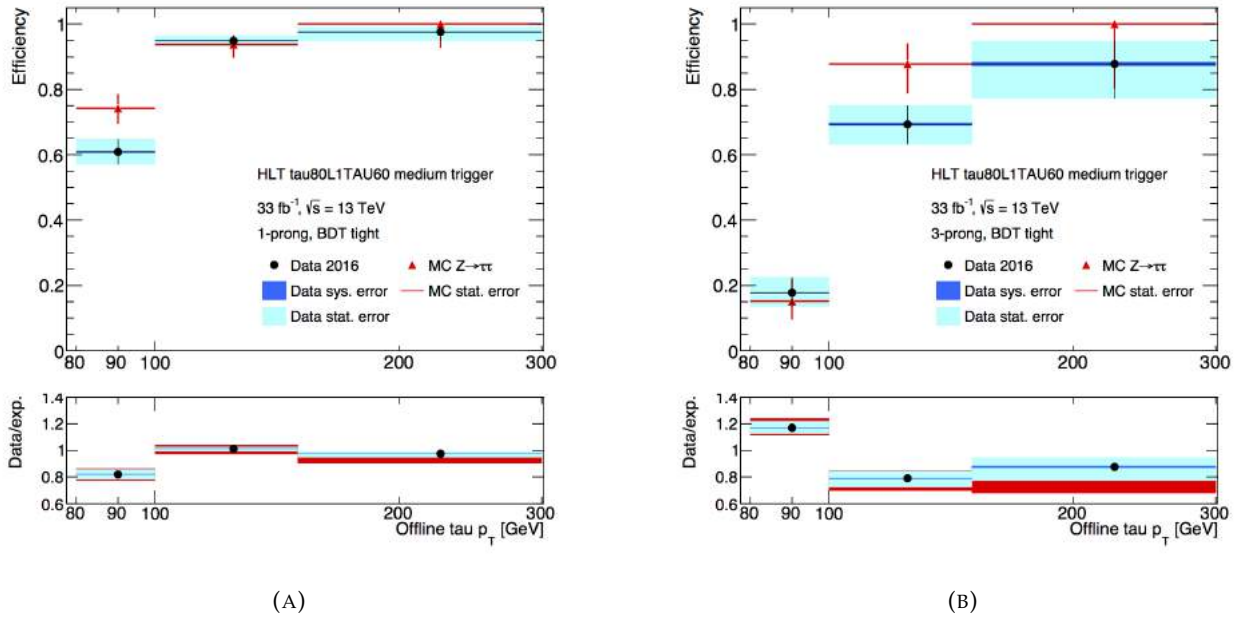


FIGURE A.12: Efficiencies of the *HLT tau80 L1tau60 medium* trigger as a function of the p_T of the offline $\tau_{\text{had,vis}}$ probe selected in $Z \rightarrow \tau\tau$ events for (left) 1-prong and (right) 3-prong taus fulfilling the tight identification working point. The systematic uncertainty on the background subtraction is shown in dark blue, the total uncertainty on data is shown in light blue, and the combined uncertainty for data and MC is shown in red.

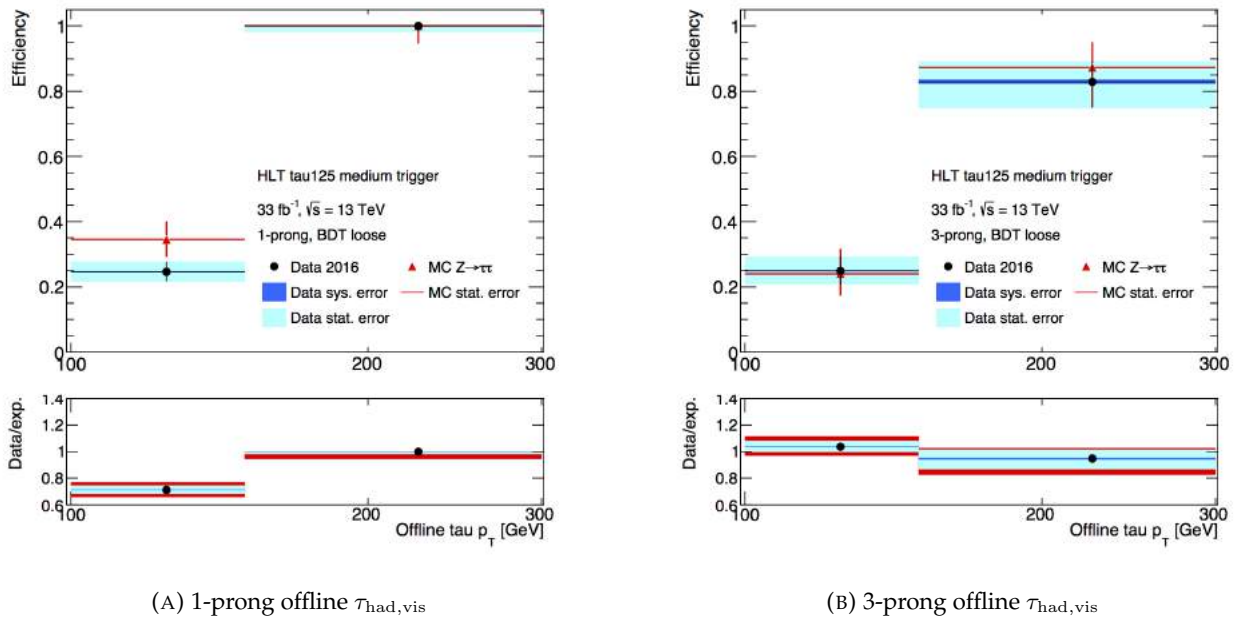


FIGURE A.13: Efficiencies of the *HLT tau125 medium* trigger as a function of the p_T of the offline $\tau_{\text{had,vis}}$ probe selected in $Z \rightarrow \tau\tau$ events for (left) 1-prong and (right) 3-prong taus fulfilling the loose identification working point. The systematic uncertainty on the background subtraction is shown in dark blue, the total uncertainty on data is shown in light blue, and the combined uncertainty for data and MC is shown in red.

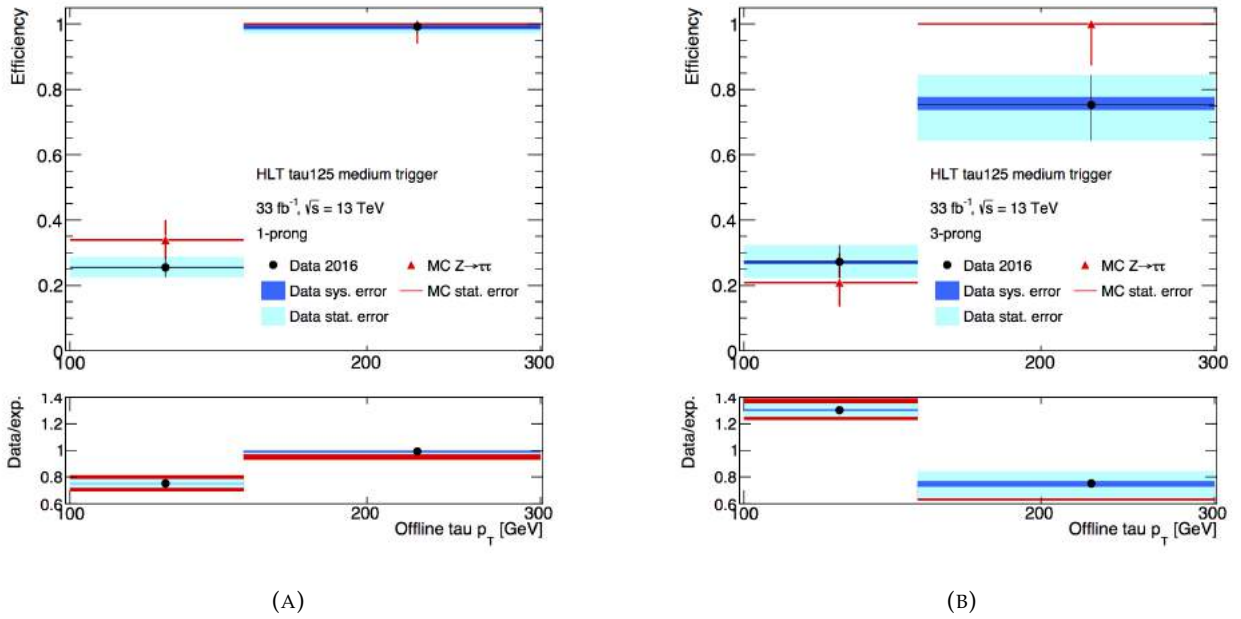


FIGURE A.14: Efficiencies of the *HLT tau125 medium* trigger as a function of the p_T of the offline $\tau_{\text{had,vis}}$ probe selected in $Z \rightarrow \tau\tau$ events for (left) 1-prong and (right) 3-prong taus fulfilling the medium identification working point. The systematic uncertainty on the background subtraction is shown in dark blue, the total uncertainty on data is shown in light blue, and the combined uncertainty for data and MC is shown in red.

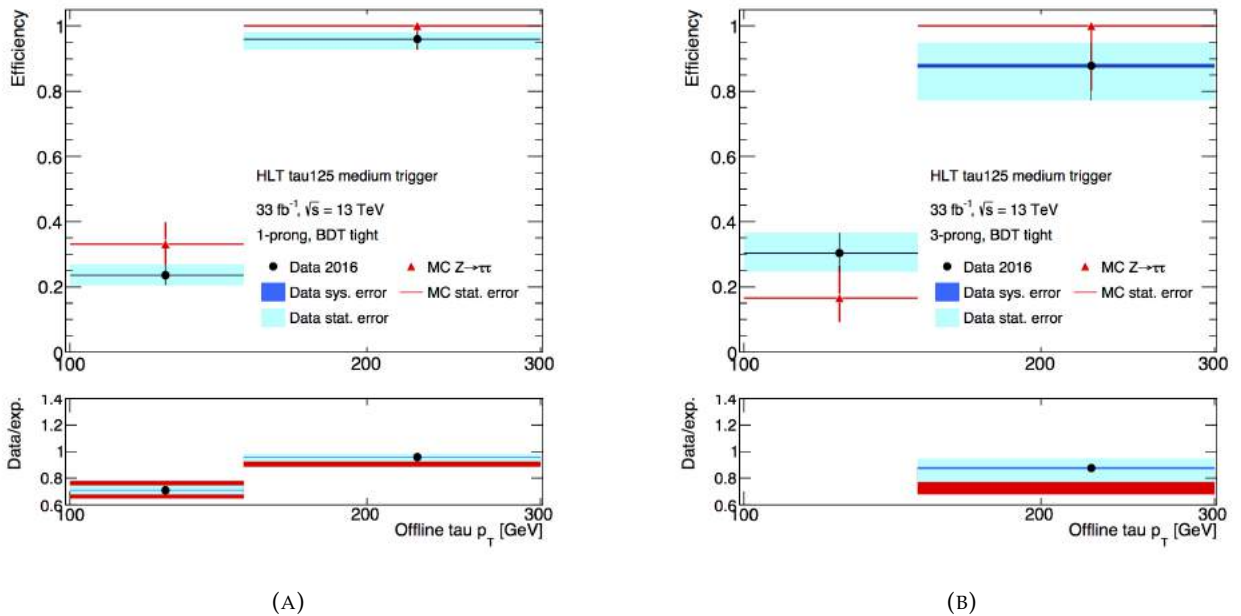


FIGURE A.15: Efficiencies of the *HLT tau125 medium* trigger as a function of the p_T of the offline $\tau_{\text{had,vis}}$ probe selected in $Z \rightarrow \tau\tau$ events for (left) 1-prong and (right) 3-prong taus fulfilling the tight identification working point. The systematic uncertainty on the background subtraction is shown in dark blue, the total uncertainty on data is shown in light blue, and the combined uncertainty for data and MC is shown in red.

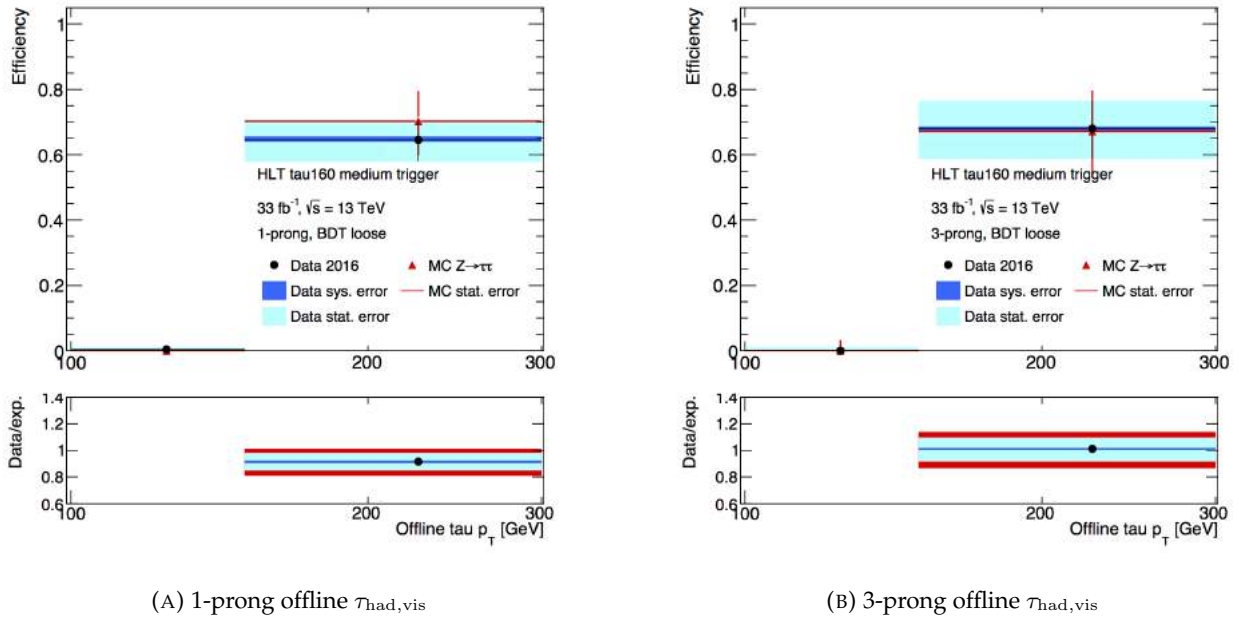


FIGURE A.16: Efficiencies of the *HLT tau160 medium* trigger as a function of the p_T of the offline $\tau_{\text{had,vis}}$ probe selected in $Z \rightarrow \tau\tau$ events for (left) 1-prong and (right) 3-prong taus fulfilling the loose identification working point. The systematic uncertainty on the background subtraction is shown in dark blue, the total uncertainty on data is shown in light blue, and the combined uncertainty for data and MC is shown in red.

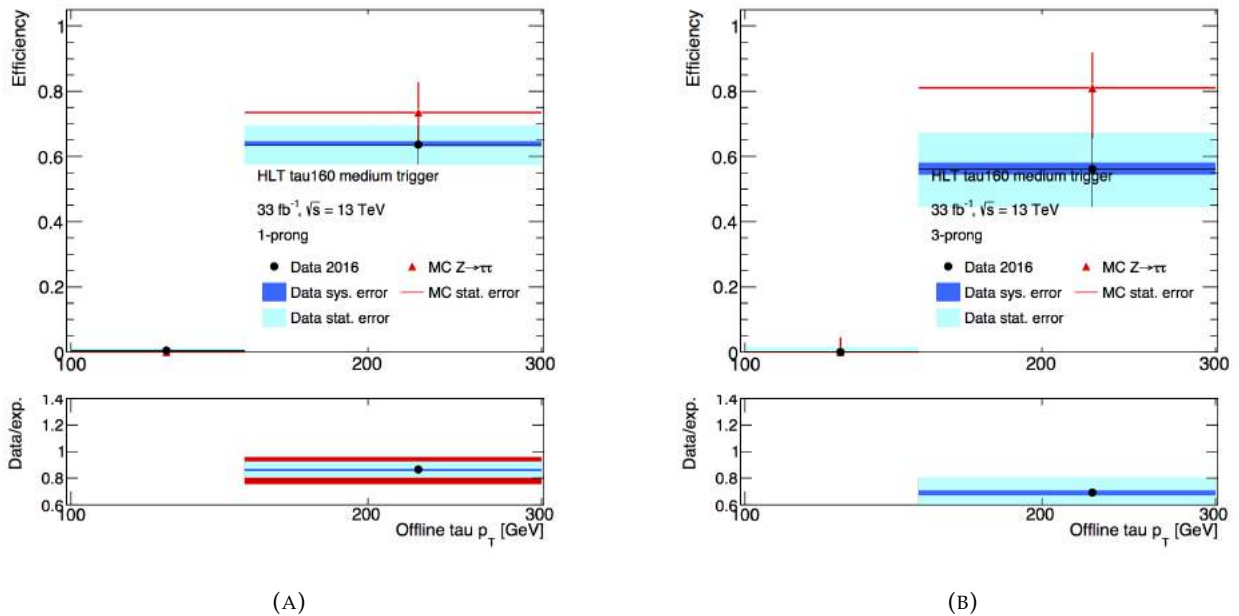


FIGURE A.17: Efficiencies of the *HLT tau160 medium* trigger as a function of the p_T of the offline $\tau_{\text{had,vis}}$ probe selected in $Z \rightarrow \tau\tau$ events for (left) 1-prong and (right) 3-prong taus fulfilling the medium identification working point. The systematic uncertainty on the background subtraction is shown in dark blue, the total uncertainty on data is shown in light blue, and the combined uncertainty for data and MC is shown in red.

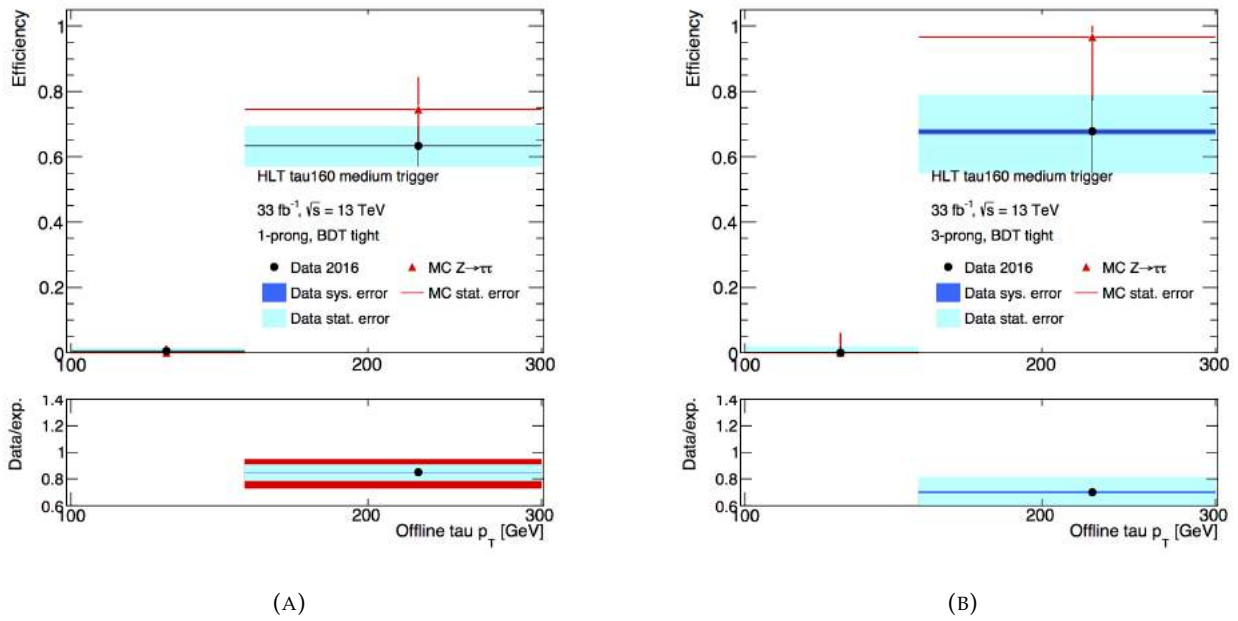


FIGURE A.18: Efficiencies of the *HLT tau160 medium* trigger as a function of the p_T of the offline $\tau_{\text{had,vis}}$ probe selected in $Z \rightarrow \tau\tau$ events for (left) 1-prong and (right) 3-prong taus fulfilling the tight identification working point. The systematic uncertainty on the background subtraction is shown in dark blue, the total uncertainty on data is shown in light blue, and the combined uncertainty for data and MC is shown in red.

Bibliography

- [1] Mark Thomson. *Modern Particle Physics*. Cambridge University Press, 2013.
- [2] M.E. Peskin and D.V. Schroeder. *An Introduction to Quantum Field Theory*. Addison-Wesley, 1995.
- [3] Lyndon Evans and Philip Bryant. “LHC Machine”. In: *Journal of Instrumentation* 3.08 (2008), S08001. URL: <http://stacks.iop.org/1748-0221/3/i=08/a=S08001>.
- [4] ATLAS Collaboration. “Observation of a new particle in the search for the Standard Model Higgs boson with the ATLAS detector at the LHC”. In: *Phys. Lett. B* 716 (2012), p. 1. DOI: [10.1016/j.physletb.2012.08.020](https://doi.org/10.1016/j.physletb.2012.08.020). arXiv: [1207.7214](https://arxiv.org/abs/1207.7214) [hep-ex].
- [5] John Ellis. “Physics Beyond the Standard Model”. In: *Nucl. Phys.* A827 (2009). [187(2009)], pp. 187C–198C. DOI: [10.1016/j.nuclphysa.2009.05.034](https://doi.org/10.1016/j.nuclphysa.2009.05.034). arXiv: [0902.0357](https://arxiv.org/abs/0902.0357) [hep-ph].
- [6] Neta A. Bahcall et al. “The Cosmic triangle: Assessing the state of the universe”. In: *Science* 284 (1999), pp. 1481–1488. DOI: [10.1126/science.284.5419.1481](https://doi.org/10.1126/science.284.5419.1481). arXiv: [astro-ph/9906463](https://arxiv.org/abs/astro-ph/9906463) [astro-ph].
- [7] Lyndon Evans and Philip Bryant. “LHC Machine”. In: *JINST* 3 (2008), S08001. DOI: [10.1088/1748-0221/3/08/S08001](https://doi.org/10.1088/1748-0221/3/08/S08001).
- [8] ATLAS Collaboration. *Reconstruction, Energy Calibration, and Identification of Hadronically Decaying Tau Leptons in the ATLAS Experiment for Run-2 of the LHC*. ATL-PHYS-PUB-2015-045. 2015. URL: <https://cds.cern.ch/record/2064383>.
- [9] Sheldon L. Glashow. “Partial-symmetries of weak interactions”. In: *Nuclear Physics* 22.4 (1961), pp. 579–588. ISSN: 0029-5582. DOI: [http://dx.doi.org/10.1016/0029-5582\(61\)90469-2](http://dx.doi.org/10.1016/0029-5582(61)90469-2). URL: <http://www.sciencedirect.com/science/article/pii/0029558261904692>.
- [10] Steven Weinberg. “A Model of Leptons”. In: *Phys. Rev. Lett.* 19 (21 1967), pp. 1264–1266. DOI: [10.1103/PhysRevLett.19.1264](https://doi.org/10.1103/PhysRevLett.19.1264). URL: <https://link.aps.org/doi/10.1103/PhysRevLett.19.1264>.
- [11] Abdus Salam. “Weak and Electromagnetic Interactions”. In: *Conf. Proc.* C680519 (1968), pp. 367–377.
- [12] C. Patrignani et al. “Review of Particle Physics”. In: *Chin. Phys.* C40.10 (2016), p. 100001. DOI: [10.1088/1674-1137/40/10/100001](https://doi.org/10.1088/1674-1137/40/10/100001).
- [13] ATLAS Collaboration. “The ATLAS Experiment at the CERN Large Hadron Collider”. In: *JINST* 3 (2008), S08003. DOI: [10.1088/1748-0221/3/08/S08003](https://doi.org/10.1088/1748-0221/3/08/S08003).
- [14] Maxim Perelstein. “Introduction to Collider Physics”. In: *Physics of the large and the small, TASI 09, proceedings of the Theoretical Advanced Study Institute in Elementary Particle Physics, Boulder, Colorado, USA, 1-26 June 2009*. 2011, pp. 421–486. DOI: [10.1142/9789814327183_0008](https://doi.org/10.1142/9789814327183_0008). arXiv: [1002.0274](https://arxiv.org/abs/1002.0274) [hep-ph]. URL: <https://inspirehep.net/record/844291/files/arXiv:1002.0274.pdf>.
- [15] *Luminosity Public Results Run-2*. <https://twiki.cern.ch/twiki/bin/view/AtlasPublic/LuminosityPublicResultsRun2>. Accessed: 26/09/2017.
- [16] G. Aad et al. “The ATLAS Experiment at the CERN Large Hadron Collider”. In: *JINST* 3 (2008), S08003. DOI: [10.1088/1748-0221/3/08/S08003](https://doi.org/10.1088/1748-0221/3/08/S08003).

- [17] Joao Pequeno. "Computer generated image of the whole ATLAS detector". 2008. URL: <https://cds.cern.ch/record/1095924>.
- [18] ATLAS Collaboration. "Performance of missing transverse momentum reconstruction in proton-proton collisions at $\sqrt{s} = 7$ TeV with ATLAS". In: *Eur. Phys. J. C* 72 (2012), p. 1844. DOI: [10.1140/epjc/s10052-011-1844-6](https://doi.org/10.1140/epjc/s10052-011-1844-6). arXiv: [1108.5602](https://arxiv.org/abs/1108.5602) [hep-ex].
- [19] Patrick Czodrowski. "Triggering on hadronic Tau Decays in ATLAS: Algorithms and Performance". In: *Journal of Physics: Conference Series* 396.1 (2012), p. 012015. URL: <http://stacks.iop.org/1742-6596/396/i=1/a=012015>.
- [20] Takashi Mitani et al. *Measurement of the tau lepton reconstruction and identification performance in the ATLAS experiment using pp collisions at $\sqrt{s} = 13$ TeV*. ATLAS Internal Note. 2016.
- [21] Georges Aad et al. "Identification and energy calibration of hadronically decaying tau leptons with the ATLAS experiment in pp collisions at $\sqrt{s}=8$ TeV". In: *Eur. Phys. J. C* 75.7 (2015), p. 303. DOI: [10.1140/epjc/s10052-015-3500-z](https://doi.org/10.1140/epjc/s10052-015-3500-z). arXiv: [1412.7086](https://arxiv.org/abs/1412.7086) [hep-ex].
- [22] ATLAS Collaboration. "Performance of the ATLAS Trigger System in 2015". In: (2016). arXiv: [1611.09661](https://arxiv.org/abs/1611.09661) [hep-ex].
- [23] Paolo Nason. "A New method for combining NLO QCD with shower Monte Carlo algorithms". In: *JHEP* 11 (2004), p. 040. DOI: [10.1088/1126-6708/2004/11/040](https://doi.org/10.1088/1126-6708/2004/11/040). arXiv: [hep-ph/0409146](https://arxiv.org/abs/hep-ph/0409146).
- [24] Stefano Frixione, Paolo Nason, and Carlo Oleari. "Matching NLO QCD computations with Parton Shower simulations: the POWHEG method". In: *JHEP* 11 (2007), p. 070. DOI: [10.1088/1126-6708/2007/11/070](https://doi.org/10.1088/1126-6708/2007/11/070). arXiv: [0709.2092](https://arxiv.org/abs/0709.2092) [hep-ph].
- [25] Torbjorn Sjostrand, Stephen Mrenna, and Peter Z. Skands. "A Brief Introduction to PYTHIA 8.1". In: *Comput. Phys. Commun.* 178 (2008), pp. 852–867. DOI: [10.1016/j.cpc.2008.01.036](https://doi.org/10.1016/j.cpc.2008.01.036). arXiv: [0710.3820](https://arxiv.org/abs/0710.3820) [hep-ph].
- [26] D. J. Lange. "The EvtGen particle decay simulation package". In: *Nucl. Instrum. Meth. A* 462 (2001), p. 152. DOI: [10.1016/S0168-9002\(01\)00089-4](https://doi.org/10.1016/S0168-9002(01)00089-4).
- [27] P. Golonka and Z. Was. "PHOTOS Monte Carlo: a precision tool for QED corrections in Z and W decays". In: *Eur. Phys. J. C* 45 (2006), pp. 97–107. DOI: [10.1140/epjc/s2005-02396-4](https://doi.org/10.1140/epjc/s2005-02396-4). arXiv: [hep-ph/0506026](https://arxiv.org/abs/hep-ph/0506026).
- [28] N. Davidson, T. Przedzinski, and Z. Was. "PHOTOS Interface in C++: Technical and Physics Documentation". In: (2010). arXiv: [1011.0937](https://arxiv.org/abs/1011.0937) [hep-ph].
- [29] ATLAS Collaboration. "Measurement of the Z/γ^* boson transverse momentum distribution in pp collisions at $\sqrt{s} = 7$ TeV with the ATLAS detector". In: *JHEP* 09 (2014), p. 145. DOI: [10.1007/JHEP09\(2014\)145](https://doi.org/10.1007/JHEP09(2014)145). arXiv: [1406.3660](https://arxiv.org/abs/1406.3660) [hep-ex].
- [30] Simone Alioli et al. "Vector boson plus one jet production in POWHEG". In: *JHEP* 01 (2011), p. 095. DOI: [10.1007/JHEP01\(2011\)095](https://doi.org/10.1007/JHEP01(2011)095). arXiv: [1009.5594](https://arxiv.org/abs/1009.5594) [hep-ph].
- [31] H.-L. Lai et al. "New parton distributions for collider physics". In: *Phys. Rev. D* 82, 074024 (2010), p. 074024. DOI: [10.1103/PhysRevD.82.074024](https://doi.org/10.1103/PhysRevD.82.074024). arXiv: [1007.2241](https://arxiv.org/abs/1007.2241) [hep-ph].
- [32] Simone Alioli et al. "A general framework for implementing NLO calculations in shower Monte Carlo programs: the POWHEG BOX". In: *JHEP* 06 (2010), p. 043. DOI: [10.1007/JHEP06\(2010\)043](https://doi.org/10.1007/JHEP06(2010)043). arXiv: [1002.2581](https://arxiv.org/abs/1002.2581) [hep-ph].
- [33] Simone Alioli et al. "NLO vector-boson production matched with shower in POWHEG". In: *JHEP* 07 (2008), p. 060. DOI: [10.1088/1126-6708/2008/07/060](https://doi.org/10.1088/1126-6708/2008/07/060). arXiv: [0805.4802](https://arxiv.org/abs/0805.4802) [hep-ph].
- [34] P. M. Nadolsky et al. "Implications of CTEQ global analysis for collider observables". In: *Phys. Rev. D* 78, 013004 (2008), p. 013004. DOI: [10.1103/PhysRevD.78.013004](https://doi.org/10.1103/PhysRevD.78.013004). arXiv: [0802.0007](https://arxiv.org/abs/0802.0007) [hep-ph].

- [35] Pierre Artoisenet et al. “Automatic spin-entangled decays of heavy resonances in Monte Carlo simulations”. In: *JHEP* 1303 (2013), p. 015. DOI: [10.1007/JHEP03\(2013\)015](https://doi.org/10.1007/JHEP03(2013)015). arXiv: [1212.3460](https://arxiv.org/abs/1212.3460) [hep-ph].
- [36] John M. Campbell et al. “Top-pair production and decay at NLO matched with parton showers”. In: *JHEP* 04 (2015), p. 114. DOI: [10.1007/JHEP04\(2015\)114](https://doi.org/10.1007/JHEP04(2015)114). arXiv: [1412.1828](https://arxiv.org/abs/1412.1828) [hep-ph].
- [37] T. Sjöstrand, S. Mrenna, and P. Skands. “PYTHIA 6.4 physics and manual”. In: *JHEP* 05, 026 (2006), p. 26. DOI: [10.1088/1126-6708/2006/05/026](https://doi.org/10.1088/1126-6708/2006/05/026). arXiv: [hep-ph/0603175](https://arxiv.org/abs/hep-ph/0603175).
- [38] Peter Zeiler Skands. “Tuning Monte Carlo Generators: The Perugia Tunes”. In: *Phys. Rev. D* 82 (2010), p. 074018. DOI: [10.1103/PhysRevD.82.074018](https://doi.org/10.1103/PhysRevD.82.074018). arXiv: [1005.3457](https://arxiv.org/abs/1005.3457) [hep-ph].
- [39] N. Davidson et al. “Universal interface of TAUOLA: Technical and physics documentation”. In: *Comput. Phys. Commun.* 183 (2012), pp. 821–843. DOI: [10.1016/j.cpc.2011.12.009](https://doi.org/10.1016/j.cpc.2011.12.009). arXiv: [1002.0543](https://arxiv.org/abs/1002.0543) [hep-ph].
- [40] ATLAS Collaboration. “Measurement of the muon reconstruction performance of the ATLAS detector using 2011 and 2012 LHC proton–proton collision data”. In: *Eur. Phys. J. C* 74 (2014), p. 3130. DOI: [10.1140/epjc/s10052-014-3130-x](https://doi.org/10.1140/epjc/s10052-014-3130-x). arXiv: [1407.3935](https://arxiv.org/abs/1407.3935) [hep-ex].
- [41] ATLAS Collaboration. “Electron and photon energy calibration with the ATLAS detector using LHC Run 1 data”. In: *Eur. Phys. J. C* 74 (2014), p. 3071. DOI: [10.1140/epjc/s10052-014-3071-4](https://doi.org/10.1140/epjc/s10052-014-3071-4). arXiv: [1407.5063](https://arxiv.org/abs/1407.5063) [hep-ex].
- [42] Federico Scutti. “Search for Neutral Higgs Bosons of the MSSM decaying to $\tau_{had}\tau_{had}$ in proton–proton collisions at $\sqrt{s} = 8$ TeV with the ATLAS detector”. PhD thesis. Universitat Bonn, 2016.